FEMTOSECOND TWO-PHOTON LASER-INDUCED FLUORESCENCE FOR TEMPERATURE AND CHEMICAL SPECIES IMAGING IN FLAMES

A Dissertation

by

PRADEEP PARAJULI

Submitted to the Office of Graduate and Professional Studies of
Texas A&M University
in partial fulfillment of the requirements for the degree of

DOCTOR OF PHILOSOPHY

Chair of Committee,	Waruna D. Kulatilaka
Committee Members,	Girish S. Agarwal
	Je-Chin Han
	Eric L. Petersen
Head of Department,	Guillermo Aguilar

May 2023

Major Subject: Mechanical Engineering

ABSTRACT

In recent years, non-intrusive, laser-based combustion diagnostic techniques utilizing ultrashort-pulse, femtosecond (fs) duration laser sources have evolved as promising tools for time-resolved imaging of fast physical processes and complex chemical reactions. The high peak power in fs-duration pulses is ideal for nonlinear spectroscopic techniques involving atoms and molecules. Additionally, the broad spectral bandwidth and high repetition rate of fs sources are advantageous over conventional nanosecond (ns) laser methods in detecting important intermediate chemical species during combustion. However, fundamental laser-matter interactions and signal generation processes during fs laser diagnostics at high-pressure practical combustion conditions are still largely unknown. Hence, this research aims to develop the fs laser-induced fluorescence (LIF) technique for practical gas turbine operating conditions, in particular high pressures and temperatures, utilizing a home-built, high-efficient frequency conversion system based on harmonic generation. This thesis consists of five research tasks highlighting the importance of intermediate species detection using optical-based combustion diagnostics and providing a basis for an environmentally sustainable and prosperous energy future.

In the first task, high-pressure combustion diagnostics is demonstrated by imaging highly reactive intermediate species, atomic hydrogen (H), in methane-air hydrocarbon flames. A comprehensive fs two-photon LIF (TPLIF) imaging study of H-atom was performed at elevated pressures (1–10 bar) for a range of flame conditions.

In the second part of this research, the same fs-TPLIF scheme was extended for flame thermometry up to 10 bar pressure using Krypton (Kr) as an inert gas tracer. Subsequently, both

H & Kr were excited simultaneously at an intermediary wavelength of 204.6 nm using the broadband, fs pulses having linewidths in excess of 400 cm^{-1}.

In the next part, the progress on kHz-rate imaging of methylidyne (CH) radical in flames using the fs planar LIF (PLIF) technique was studied for the first time. In the last task, a detailed spectroscopic and imaging study was extended to a molecular species (i.e., molecular nitrogen, N_2) to investigate the complex spectroscopy in N_2 excitation.

Overall, the above developments and the associated reacting flow diagnostics are significant steps forward in utilizing the ultrashort, broadband, high-repetition-rate, fs-duration laser pulses for practically relevant combustion diagnostics.

DEDICATION

To my family, for all their love, support, and belief in me and my capability and for continuously encouraging me to do wonders. I am indebted to their sacrifices, and I would not have been in this position today without their guidance.

ACKNOWLEDGEMENTS

This thesis research was conducted in the amazing and friendly environment at the Optical Diagnostics and Imaging Laboratory at J Mike Walker ’66 Department of Mechanical Engineering. It had been a short and sweet research adventure with interesting people from different parts of the world. Thank you to all who got engaged with me during this period. First and foremost, I would like to express my profound gratitude to my thesis advisor Dr. Waruna D. Kulatilaka, for giving me the opportunity to carry out my thesis work in this laboratory and for his constant support and assistance along this beautiful journey. Thank you Dr. Kulatilaka for giving me the freedom, and, at the same time, constantly engaging in my research work. Thank you for being patient, especially at the beginning of my journey and for all the belief in me and for providing me feedback on my work. A very special acknowledgment to Dr. Girish Agarwal, Dr. Je-Chin Han, and Dr. Eric Petersen for serving as my thesis committee members and providing guidance in graduate school and my research career. I have been fortunate to be mentored by such a group of an esteemed committee whose admiration and respect in their respective fields are remarkable.

I would also like to acknowledge my colleagues Matthew Hay, Dr. Yejun Wang, Dr. Ayush Jain, and William Swain for helping me in different stages of my experimental work. I would like to mention and thank all the wonderful people in and around the laboratory Christian Schweizer, Gavin Lukasik, Matthew Intardonato, Kristi Naude, Tyler Paschal, Nicholas Niemiec, Mattias Turner and Manuel Suarez. It was nice working with you all.

I would like to thank laser technicians and engineers from “Spectra-Physics,” Mike Herrick and Dr. McArthur, for their assistance with maintaining the fs laser system.

I am also thankful to my friends in College Station and outside for their continuous support in all the phases of this work and for the wonderful memories.

Also, warm, and utmost gratitude is due to my family members for their belief, continuous support, and encouragement and for teaching me life decisions analysis.

CONTRIBUTORS AND FUNDING SOURCES

Contributors

This research was supervised by a dissertation committee consisting of Dr. Waruna D. Kulatilaka, Dr. Je-Chin Han, and Dr. Eric L. Petersen of the J. Mike Walker ’66 Department of Mechanical Engineering, and Dr. Girish S. Agarwal of the Department of Biological and Agricultural Engineering.

All work in the dissertation was completed by the student, in collaboration with Matthew Hay, Dr. Yejun Wang, Dr. Ayush Jain, and William Swain of the Department of Mechanical Engineering.

Funding Sources

This research was funded by the National Science Foundation (NSF) Combustion, Fire and Plasma Systems Program and the Office of Naval Research (ONR). The facilities support was provided by the Texas A&M Engineering Experimental Station Turbomachinery Laboratory (TEES-TL).

Pradeep Parajuli was further supported by Pioneer Natural Resources Fellowship (2020 and 2022), Ralph E. James Fellowship (2021), Preparing Future Faculty for Mechanical Engineering (PF2ME) Program Award, Graduate Summer Research Grant Program (2020 and 2022).

The contents are solely the responsibility of the authors and do not necessarily represent the official views of NSF, ONR, and TEES-TL.

NOMENCLATURE

B	Magnetic flux density (T or V s m^{-2})
CARS	Coherent anti-Stokes Raman Scattering
CCD	Charge-Coupled Device
CH	Methylidyne radical
CMOS	Complementary Metal-Oxide Semiconductor
CO	Carbon Monoxide
D	Electric flux density (C m^{-2})
DUV	Deep Ultra-Violet
E	Electric field (V m^{-1})
fs	Femtosecond
FHG	Fourth Harmonic Generation
FNS	First Negative System
H	Magnetic field (A m^{-1})
H	Hydrogen atom
ICCD	Intensified Charge-Coupled Device
J	Current density (A m^{-2})
Kr	Krypton atom
LIF	Laser-induced fluorescence
M	Magnetization density (A m^{-1})
N	Nitrogen atom
NO	Nitric Oxide

ns	Nanosecond
O	Oxygen atom
OH	Hydroxyl radical
P	Polarization density (C m^{-2})
PLIF	Planar Laser-Induced Fluorescence
SHG	Second Harmonic Generation
SNR	Signal-to-noise ratio
SPS	Second Positive System
TDLAS	Tunable Diode Laser Absorption Spectroscopy
THG	Third Harmonic Generation
TPLIF	Two-photon laser-induced fluorescence
UV	Ultra-violet
VUV	Vacuum Ultra-violet
ρ	Charge density (C m^{-3})
ϕ	Equivalence ratio
ε_0	Permittivity of free space (C V^{-1} m^{-1})
μ_0	Permeability of free space (V s^2 m^{-1} C^{-1})
λ	Wavelength

TABLE OF CONTENTS

Page

LIST OF TABLES

Page

LIST OF FIGURES

Page

1. INTRODUCTION

1.1 Background

Why do we study the combustion process, and how can laser diagnostics help? Combustion contributes to more than 85% of the total energy consumption in the world [1]. Numerous hydrocarbon-based compounds have been widely used as reliable fuel sources for internal combustion engines, gas turbines, and industrial applications for over many decades. The combustion phenomenon of these fuels and many other alternative sources is being explored for practical applications spanning a range of operating conditions and combustor geometries. All these processes are affected by the spatial and temporal distribution of the key intermediate species and temperature gradients. A deeper understanding of the physical and chemical nature of the combustion phenomena requires quantitative information of the important flame species, which can then be used to resolve the issues related to the fuel economy, emissions, and optimize the stable operational envelope of the practical combustors.

The combustion chemistry of hydrocarbon fuels is fundamentally dictated by the presence of intermediate atomic species such as hydrogen (H), oxygen (O), and nitrogen (N), along with molecular species or radicals such as hydroxyl (OH), methylidyne (CH) and carbon monoxide (CO). These species are of significant interest as they play a pivotal role in chemical kinetics and combustion chemistry. Generation and consumption rates of these species can be extremely fast and depend on the thermophysical properties of the medium such as temperature, heat release, and turbulent mixing. Hence, it becomes tremendously challenging to measure the absolute concentration and spatio-temporal distribution of these species accurately using conventional

methods. Combustion diagnostics can be carried out using physical probes or optical and laser-based methods. The laser-based optical diagnostics offer several advantages for studying combustion processes. Depending upon the quantity of interest, which may be a combination of species concentration, temperature, pressure, velocity, and flow structures, researchers can implement various laser-based diagnostics techniques. Unlike the conventional methods that use physical probes, laser-based measurements are non-intrusive as the photons, in principle, do not interact with the flow field and combustion species. In addition, the laser photons undergo the same type of damage, such as the melting of physical probes at high temperatures, thereby increasing the applicability of laser diagnostics in extreme conditions. The laser beams are usually focused on to a small probe volume providing fine spatial resolution and can often provide high concentration measurement sensitivity in the order of parts-per-billion (ppb) levels. Several commonly used laser diagnostics approaches include Raman scattering, Rayleigh scattering, laser-induced fluorescence (LIF), tunable diode laser absorption spectroscopy (TDLAS), and coherent anti-Stokes Raman scattering (CARS).

1.2 Significance of Thesis Research

The primary thrust of this thesis proposal is to enable the spatially and temporally resolved imaging of several intermediate atomic and molecular species produced in the gas-turbine relevant flame environment using a novel method of femtosecond (fs) two-photon LIF (TPLIF). Spatially and temporally resolved imaging of these key species is of particular interest to developing highly efficient engines with reduced emissions. The imaging diagnostics enable visualization of the flow field and physical and chemical processes involved in complex mixing regions, which primarily determine the combustor efficiency and harmful emissions.

Atomic hydrogen is a highly reactive intermediate species that plays a key role in several chain-branching reactions that govern efficiency and pollutant formation in hydrocarbon combustion [2]. Further, it plays a crucial part in flame ignition, propagation, and extinction. Spatially resolved imaging of H helps in the understanding of light species transport and preferential diffusion in reacting flow environments. Further, the substantial presence of the H-atom directly impacts the chain-branching steps leading to ignition and results in an increase in the flame speed, therefore the overall combustion process. Similarly, OH radical is another important intermediate species during the combustion process. It is produced mostly in the high-temperature zone, and its spectroscopy is well studied by many researchers [3-7]. In combination with quantitative CO measurements, OH can be used to correctly predict the heat release rate in hydrocarbon-air flames as the predominant reaction for the formation of CO_2 in hydrocarbon combustion is $CO + OH \rightleftarrows CO_2 + H$ [8-10]. Additionally, atomic oxygen is another reactive species that plays a vital role in chain-branching reactions and pollution formation pathways during hydrocarbon combustion [11, 12]. Atomic oxygen in reaction with molecular nitrogen (N_2) and N controls the reactions of nitric oxide (NO) formation through the Zeldovich mechanism and also nitrous oxide (N_2O) formation during the intermediate reactions [13].

Further, flame thermometry is an important technique to characterize combustion systems. Several laser-based techniques offer the advantage of non-intrusive measurements with high spatial and temporal resolution. The most widely used thermometry techniques are Rayleigh scattering, CARS, LIF etc. Kr LIF is often introduced into the flow fields as an inert gas tracer for 2D temperature imaging [14-16], 1D velocity measurement and mixing process imaging [17-19]. The *in-situ* temperature measured from Kr LIF can further be applied for the calibration purpose of intermediate species like H and N following the approach recommended by Lamoureux et al.

[20]. Establishing such a thermometry technique and incorporating it for quenching correction to quantify the H atom is another major significance of this thesis. This simple and innovative temperature measurement technique is now verified for a simple laminar flame case which in the future can be applied for the SS temperature imaging in flames using an optimized fs harmonic generation system.

This research further reports the progress in CH planar LIF (PLIF) diagnostics with a significantly high signal-to-noise ratio (SNR) to investigate turbulent flame interaction. CH serves as a better radical to locate the position of the flame front compared to OH radical even in complex flows. An additional advantage over OH is that its distribution correlates with the region of peak heat release rate [6, 21, 22] because of its rapid production and consumption on both sides of the high-temperature reaction zone [23]. Additionally, its concentration and well-defined spatial distribution indicated by CH PLIF visualizes turbulence chemistry interactions including flame wrinkling, local extinction, and its stabilization [24]. CH has also been recognized as a key reactant for prompt NO formation and its distribution is particularly needed to model pollutant formation in turbulent non-premixed flames [25, 26].

This study further investigates the excitation/detection schemes of N_2 molecule. N_2 is the principal constituent of the earth's atmosphere that plays an important role in several theoretical and experimental studies, where its electronic states are commonly used as probe species [27]. It plays a significant role in the combustion process and atmospheric phenomena such as auroras, and airglows [28, 29]. Nitrogen molecule plays a part in pollutant formation as high-temperature combustion in its presence, such as in automobile engines, can generate NO and nitrogen dioxide (NO_2) [13]. N_2 molecule is an attractive constituent for optical and non-invasive diagnostics of such processes because it can be easily obtained in experiments. The investigation of its excited

states is important for photo-physics and atmospheric photochemistry [30], and the spectral information associated with these states can be used to obtain local temperature and density inside the atmospheric model [31, 32]. Although only the initial excitation/detection schemes are part of this study to explore the ambiguity in N_2 excitation, this thesis highlights the importance of thermometry techniques using spectrally resolved N_2 spectra.

Overall, intermediate species like H, O, OH, N_2, and CH fundamentally dictate the chemistry of hydrocarbon combustion. So, understanding the destruction pathways of the reactant mixture along with well-quantified intermediate species provides insights into the physical and chemical nature along with facilitating the development of model-based prediction abilities. Experimental datasets are needed to verify the computational models before endorsing them for various applications eliminating the need for expensive experiments. An exhaustive qualitative and quantitative measurement of key flame species is necessary due to the lack of accurate measurements because of limited optical access in realistic harsh environments. Hence, similar flame environments are often replicated on a small scale in laboratory burners, and essential measurements are performed to predict the realistic combustion chemistry. A deeper understanding of these laboratory-controlled measurements can lead to a more efficient design of furnaces and engines, and improved fuel economy while simultaneously reducing emissions injurious to health and the environment. Such investigations, in a broad sense, provide a basis for an environmentally sustainable and prosperous energy future which is the main research mission.

1.3 Dissertation Outline

The current work focuses on advancing fs LIF diagnostics technique for practical gas turbine operating conditions, in particular high pressures and temperatures, utilizing a home-built,

high-efficient frequency conversion system based on a harmonic generation system. The first objective is to extend such ultrafast fs diagnostics approach for chemical species imaging for the detailed understanding of highly dynamic and vastly changing combustion chemistry. The second objective is to develop the fs diagnostics approach for flame thermometry studies via Kr TPLIF measurement and utilize the broad bandwidth of fs laser pulses for simultaneous measurements to obtain species concentration.

This thesis proposal is outlined as follows. Chapter 2 introduces an extensive literature review on the theory of LIF, mode-locked fs pulse generation, laboratory-scaled burners for combustion research and detection systems for fluorescence emission collection. Chapter 3 demonstrates the applicability of the home-built high-energy frequency conversion unit for fs-TPLIF H-atom imaging in high-pressure flames for the first time. The development of the current TPLIF scheme for a Kr-based flame thermometry technique followed by a simultaneous investigation of two species (H & Kr) for quantitative measurements are discussed in Chapter 4 and Chapter 5 respectively. Chapter 6 reports the progress in SS CH PLIF measurements via an optimized second harmonic generation (SHG) system reducing setup complexity. A detailed spectroscopic investigation of the N_2 excitation/detection scheme for flame structure, mixing, and a potential thermometry purpose are discussed in Chapter 7. A summary of the current work, along with the limitations of the current work and future perspectives, are detailed in Chapter 8.

2. LITERATURE REVIEW*

2.1 Introduction to Laser-Induced Fluorescence

Fluorescence is simply defined as the spontaneous emission of radiation from an upper energy level excited by absorption of radiation. LIF spectroscopy is a technique that possesses the capability to detect flame and pollutant species at the ppm or even sub-ppm level and has received considerable attention since the early 1980s [33-36]. More than thirty combustion intermediates consisting of O, N, C, H atoms and their combinations have been detected by LIF [35]. During the initial days of the laser development, its tunability was limited, and the frequency typically did not coincide with the specific electronic transitions of atoms or molecules needed for the excitation process. This situation limited the scope of detecting numerous intermediates; however, with the development of dye lasers and optical parametric amplifier, the output radiation could be tuned specifically to the required transitions, and LIF became one of the most used diagnostic approaches for a large number of fields. The electronic absorptions of most of the species lie in the 200 to 600 nm range, a range which can be easily achieved using the tunable dye laser and fs laser system.

Figure 2.1 depicts two LIF approaches, fluorescence spectrum and excitation scan. In a fluorescence spectrum, the laser is tuned to a specific excitation wavelength, and the spectrometer is scanned to record the various emission transitions. In an excitation spectrum, the laser is tuned across various absorption lines, and the broadband fluorescence spectrum is recorded. Generally, the fluorescence wavelength occurs mainly at longer wavelengths.

---

*Part of this chapter is reprinted with permission from "Femtosecond two-photon LF imaging of atomic hydrogen in high-pressure methane-air flames" by P. Parajuli, Y. Wang, M. Hay, V. R. Katta, W.D. Kulatilaka, Proceedings of the Combustion Institute (2022 in press). Copyright [2022] by The Combustion Institute. Published by Elsevier Inc.

It is termed as Stokes shifted as emission occurs from a new level different than the one involved in the absorption process [37]. The spectrally shifted fluorescence is studied in combustion diagnostics to avoid the interferences from scattered laser light or Mie scattering, which is strongly wavelength independent. However, the absorption processes, being resonant, have much larger cross-sections than the Raman effects, and hence, the fluorescence is many orders of magnitude stronger than Raman scattering, which provides LIF with high detection sensitivities.

The quantitative measurement of the fluorescence signal is another intriguing topic for combustion diagnosis. Several basic criteria and requirements needed for the quantitative measurement are explained here. The atom or molecule under investigation must have a known emission spectrum. Sometimes a molecule undergoes predissociation, dissociate prior to the emission of a photon when excited to a certain energy level. In some cases, it may ionize via the photoionization process, which changes the electronic configuration and causes to have a much different spectroscopy than the neutral molecule. The molecule must have an absorption wavelength that is accessible to a tunable laser source to park the laser at a specific wavelength for excitation. Present-day laser systems have a spectral tuning range roughly from 200 nm to 1.5 μm. The multi-photon excitation technique has made possible the detection of species with absorptions even below 200 nm. Details will be explained later in this chapter. Further, the rate of radiative decay of the excited state must be known as the fluorescence signal is proportional to that. Several excited state loss mechanisms like collisional deactivation, photoionization, and predissociation need to be accounted for. In the presence of molecules other than the one of interest, the total decay rate is increased due to collisions, known as quenching. Hence, the fluorescence signal needs to be corrected for collisional quenching to obtain species number densities. The quenching correction requires the knowledge of partial pressures of all the species involved as well as the

rates for deactivation of the excited state and its temperature dependence. Further, depending on the laser sources used during LIF, the possibility of laser-induced chemistry should be considered. Such chemistry reduces or increases the radical pool locally and leads to measurement error if the chemical reaction rate in the excited state is higher than the ground state, especially when high-energy microsecond laser pulses are employed. Such behavior is avoided in modern experiments using nanosecond (ns) or less pulse lengths.

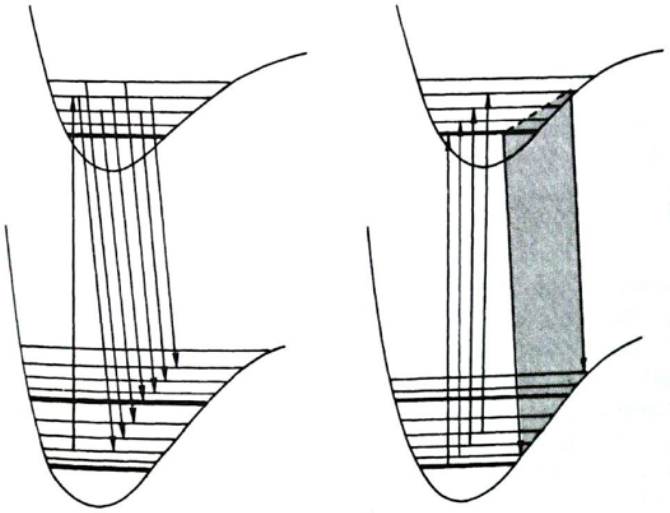

Figure 2.1 Schematic of potential energy curves for lower and upper electronic states showing fluorescence spectrum (left panel) and an excitation spectrum (right panel) reprinted from [37].

2.1.1 Advantages and Limitations of LIF

LIF is a long-established combustion diagnostics technique. It offers numerous advantages over several other laser-based diagnostics including scattering or optical emission spectroscopy. Key significance lies in its ability to detect species-selective during the excitation process. Usually, the laser is tuned such that the bandwidth of the laser overlaps with a specific excitation of a single transition that has a large absorption cross-section resulting in efficient excitation of that transition

and emission of a photon. Such fluorescence signals are spectrally or temporally filtered out from other background signals which result in high signal-to-noise ratios (SNR) for most applications. This technique allows very low detection limits from a few ppm to ppb level enabling diagnosis of minor or trace species in many applications. LIF signals are produced from the volume of illumination from the laser; hence they are spatially resolved, which is a marked strength over absorption spectroscopy. The signals can be collected from a specific zone, and further allows the advantages of imaging an area illuminated by a planar sheet, and the diagnostics method is known as planar LIF (PLIF). Additionally, the LIF technique as a thermometry measurement is already in practice. Typically, the laser is tuned to specific temperature-sensitive rotational lines and the emissions collected can be used to calculate rotational temperatures with ±25 K accuracy.

The use of LIF is complicated by the occurrence of non-radiative decay. Some of the excited species, instead of emitting fluorescence signals, may undergo different decay processes like stimulated emission, intersystem crossing, internal conversion, as shown in Figure 2.3. Additionally, not all atomic or molecular species have electronic transitions at accessible wavelengths. In some cases, processes like laser-induced chemistry, light trapping in molecules complicate a fluorescence signal, although they can be avoided through a meticulous experimental setup.

2.1.2 Comparison between Nanosecond and Femtosecond LIF

The applications for fs-duration laser pulses for LIF measurements carry significant advantages over ns-duration laser pulses although the latter has been utilized widely, including experiments in challenging diagnostic conditions. Some of the important advantages are listed below:

Short optical pulses:

In combustion diagnostics, most of the energy dissipation and the transfer processes occur on a time scale larger than 100 fs. Fs laser pulses enable the species of interest to get excited instantly, and the dynamics of the excited state can be monitored with higher temporal resolution when compared to ns-duration laser pulses. The temporal resolution is as close as $\sim 0.5\,\tau_{\mathrm{pulse}} \approx 12 - 50$ fs for most commercial lasers.

High peak power of the light:

The laser power is given by $I \sim \frac{J}{\tau_{\mathrm{pulse}}}$; I = Power, J = pulse energy.

1 mJ pulse with 10 ns duration has peak power ~ 0.1 MW.

1 mJ pulse with 100 fs duration has peak power ~ 10 GW.

The high peak power of the fs pulses enables efficient fluorescence excitation, followed by higher emission collection.

Laser bandwidth limits:

The fs-duration laser pulses are characterized by large spectral bandwidth, as shown in Figure 2.2. The laser bandwidth is given by:

$$\Delta\lambda \approx \frac{\lambda^2}{(c\Delta t)} \qquad 2.24$$

So, for 10 ns pulses with $\lambda = 800$ nm, $\Delta\lambda \approx 0.0002$ nm.

So, for 100 fs pulses with $\lambda = 800$ nm, $\Delta\lambda \approx 21$ nm.

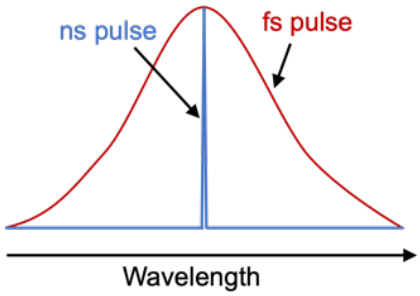

Figure 2.2 Large spectral bandwidth of a fs-laser pulse.

Although the large bandwidth limits the choice of the laser active medium, this property is quite important in the simultaneous detection of multiple species using a single broadband fs laser pulse. For example, simultaneous detection of CO and OH using 283-nm [38], H and OH using 307-nm [39], NO, O, and O_2 using 226-nm [40] laser pulse can be performed.

Reduced photo-dissociation:

One of the major limitations while using ns-duration pulses in combustion diagnostics is the use of relatively large average laser energy to produce a moderate fluorescence signal. This amount of energy can produce photo-dissociation which interferes with the quantification of the species to detect. However, fs-laser pulses with comparable average laser energies show no effects from photo-dissociation because of the lesser laser fluence for similar average energy incident. As the photo-dissociation scales linearly with the incident laser energy, the lower fluence ensures lower photo-dissociation interference and increases the accuracy of the fs-laser system.

2.1.3 Single-Photon Laser-Induced Fluorescence

Single-photon LIF is based on the absorption of a single photon and subsequent emission of a photon. This is shown schematically by the Jablonski diagram in Figure 2.3. It provides a

representation of ground and excited electronic states along with processes like absorption and emission (both radiative and nonradiative) energy. Initially, a molecule is at the ground state with each molecular orbital containing two electrons having antiparallel spin according to Pauli's principle. The total spin in the ground state is zero and this energy state is known as the singlet state, labeled as S_0. The electronic spin in the excited state occurred through the absorption of radiation. Depending upon the spin, it could be a singlet (antiparallel) and triplet (parallel) state. The absorption of a photon with an energy that matches the energy separation between the ground and excited state causes the molecule to get excited to the excited states, and the process is governed through the Franck-Condon principle. Such transition takes place so fast ($\sim 10^{-15}$ s). In Figure 2.3, molecules are excited to two excited states S_1 and S_2, they are acquired depending on the wavelength of the radiation absorbed. The molecule can't stay in the excited state for long and eventually relaxes to the ground state through several deactivation processes. Some molecules may undergo vibrational relaxation to the lowest vibrational unit through which the molecule emits a photon and return to the ground state, known as fluorescence (indicated by green arrow). This procedure takes about 10^{-9} s. Sometimes the molecule in a singlet state crossed over to the triplet state through the intersystem crossing. Several other energy transfer processes like stimulated emission, collisional quenching, ionization, internal conversion can depopulate the excited state and interfere with the fluorescence signal.

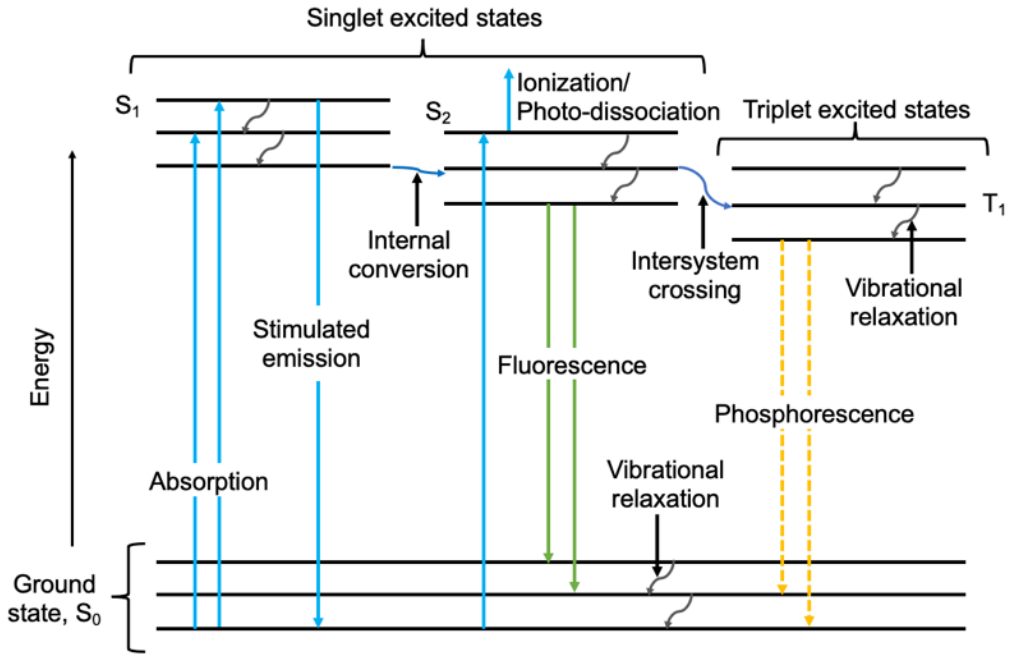

Figure 2.3 A typical Jablonski diagram showing the possible radiative and non-radiative processes.

Derivation of rate equations:

Consider a simple two-level energy diagram with ground state 1 and the excited state 2 for the quantitative analysis of a single-photon LIF signal as shown in Figure 2.4. It shows the excitation process, b_{12} leads to the stimulated emission, b_{21} and spontaneous emission or fluorescence, A_{21}. The rate constants (b_{12} and b_{21}) are related to the Einstein coefficient for absorption or stimulated emission, B by the equation

$$b = \frac{BI_v}{c} \qquad \text{Eq. 2.25}$$

Where, I_v is the incident laser irradiance per unit frequency interval ($W/cm^2 \cdot sec^{-1}$) and c is the speed of light.

b_{21} along with collisional quenching, Q_{21} is expected to affect the excited state population. The effect of ionization, $W_{2i,}$ and photo-dissociation, P, can be neglected for the sufficiently low incident laser fluence.

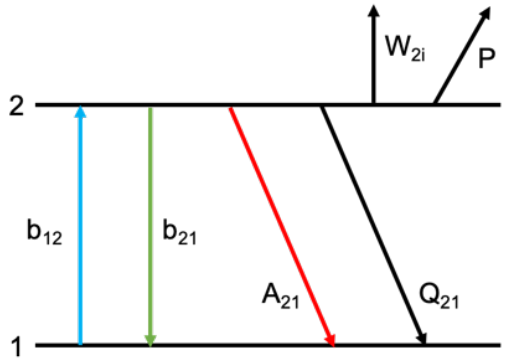

Figure 2.4 Energy level diagram showing different processes along with LIF.

The rate equations for temporal derivatives of the state population densities, N are

$$\frac{dN_1}{dt} = -N_1 b_{12} + N_2(b_{21} + A_{21} + Q_{21}) \quad 2.26$$

$$\frac{dN_2}{dt} = N_1 b_{12} - N_2(b_{21} + A_{21} + Q_{21}) \quad 2.27$$

At steady-state conditions, the relationship between populations in state 1 and state 2 becomes

$$\frac{dN_1}{dt} + \frac{dN_2}{dt} = \frac{d(N_1+N_2)}{dt} = 0; \quad 2.28$$

Hence, $N_1 + N_2 = \text{constant} = N_1^0$

$$N_2 = N_1 \frac{b_{12}}{b_{21}+A_{21}+Q_{21}} \quad 2.29$$

The fluorescence signal is proportional to $N_2 A_{21}$. Assuming the fluorescence is in linear regime, the signal strength at low laser excitation irradiances is given by

$$F = \frac{h\upsilon}{c}\frac{\Omega}{4\pi} lAN_1^0 B_{12} I_v \frac{A_{21}}{(A_{21}+Q_{21})} \quad 2.30$$

Where,

F = fluorescence signal power

h = Planck's constant

υ = frequency of emitted fluorescence

Ω = collection solid angle

l = axial extent along the beam from which fluorescence is observed

A = focal area of the laser beam

N_1^0 = total number of populations in the ground and the excited states

2.1.4 Two-photon Laser-Induced Fluorescence (TPLIF)

In modern days, laser equipment can generate tunable radiation in a continuous spectral range down to about 200 nm. However, most atoms and molecules possess absorption wavelengths well below 200 nm. Although laser radiation could be tuned in this region, it is difficult to conduct the experiments due to experimental absorption caused by molecular oxygen and other gases as we proceed deeper into the vacuum UV region. Hence, the electronic transitions in the vacuum UV are accessed and excited via the simultaneous absorption of two or more photons, and the phenomenon is called the multi-photon excitation scheme.

The two-photon excitation rate constant per molecule is written as [41, 42]

$$W_{12} = \frac{\alpha_{12} I^2}{h\omega} \qquad 2.31$$

Where, $\alpha_{12}$is the two-photon absorption cross section from state 1 to state 2. In the rate equations discussed earlier, the one-photon pumping term $N_1 b_{12}$would now be replaced by $N_1 W_{12}$.

The multi-photon excitation scheme offers several significant advantages over the singe-photon excitation scheme. The excitation wavelengths are red-shifted from the VUV region, allowing laser beam propagation with minimal absorption in air. It will have significantly lower

signal strength as compared to single-photon excitation because with the increase in the number of photons required for excitation, the absorption cross-sections also decrease. Such multi-photon transitions are difficult to saturate, and the fluorescence dependence on the laser irradiance shows non-linear behavior, given by

$$F_{\text{multi-photon}} \propto I^n$$

Where, I= laser intensity

n = number of photons involved in the transition from the ground electronic state to the excited electronic state.

Table 2.1 Two-photon excitation wavelength for different atomic and molecular species

Atomic/ Molecular species	Two-photon transition
H	205.10 nm
O	225.60 nm
Kr	204.10 nm
CO	230.00 nm
NH_3	305.00 nm
H_2O	248.00 nm
N	206.65 nm
C	284.20 nm

Most of the applications of the multi-photon excitation scheme lies in laminar flame investigations to validate various chemical kinetic flame models [43, 44]. The study focuses on the absolute concentrations as well as the spatial profiles. Many commercial laser systems can

produce laser radiation near 200 nm which is idle for species detection in many disciplines including combustion, biomedical, and materials processing. Some of the atomic and molecular species with single-photon transitions in vacuum UV that are measurable using two-photon excitation are shown in Table 2.1.

2.1.5 Prior Research on Hydrogen Atom Detection

In flames, the excitation of H-atom is performed through two- or three-photon processes [45, 46]. The first TPLIF of H in flames was reported by Lucht et al. in 1983 [43]. Conventionally, ns lasers are employed for LIF measurements of H-atom [43, 45]. However, it requires high pulse energy which is sufficient enough to photolyze precursors of H-atoms such as H_2O, OH, CH_3, and C_2H_2 [47], which then interfere with the LIF signal. In recent years, several researchers have shown that such photolytic interferences can be suppressed by using picosecond (ps) [45, 47-49] and fs [50-56] and pulsed lasers via efficient multi-photon excitation through high peak power, yet lower total pulse energy. The most used excitation scheme lies near deep ultra-violet (DUV) wavelength matching n =1 →→ n=3 transition at 205.1 nm and LIF detection from n =3 → n=2 decay at 656 nm [43, 45, 49-52, 57-59]. Also, three-photon excitation has been reported where red shifting the laser to match the n =1 →→→ n=4 transition at 292 nm followed by fluorescence detection from the n =4 → n=2 decay at 486 nm [48, 59-61]. In addition, Jain et al. [56, 62] have successfully demonstrated three-photon excitation at 307.7 nm using fs pulses and signal detection at 656 nm.

Most of these H-atom investigations were limited to sub-atmospheric conditions because of higher mole fractions of intermediates, lower quenching rate, and higher spatial distribution of the reaction zone because of slower reaction rate as compared to atmospheric and high-pressure flames [58]. One additional reason for no prior demonstration of H-atom measurements in high-

pressure flames is due to high absorption losses of excitation laser pulses while transmitting through thick optical windows of high-pressure vessels. It was shown that the losses could be minimized by red shifting the excitation wavelength to 307.7 nm instead of the commonly used scheme at 205.1 nm [56, 62]. However, the investigation was challenging because of the significantly weaker three-photon cross-section as compared to the already weak two-photon cross-section. Hence, this research is an attempt to demonstrate of H-TPLIF imaging in high-pressure flames using high-conversion efficiency direct-frequency-quadrupled fs laser pulses from a frequency tunable amplified pump laser. In real life, propulsion and power generation engines, gas turbines and several combustion devices operate at elevated pressure; hence, an in-depth understanding of the combustion process at relevant operating pressure is always an intriguing topic for researchers. In recent publications, Rahman et al. successfully demonstrated the high-pressure demonstration of CO molecule [63] and O-atom [64] using fs, TPLIF technique. Recently, we have shown the potential of broadband, fs-duration laser pulses for high-speed, single-shot OH-PLIF imaging applications in high-pressure flames, same as the one used in the current study, using a home-built, third-harmonic generation (THG) system pumped by a tunable fs laser pulse [65].

2.1.6 Prior Research on Simultaneous Krypton Thermometry and Hydrogen Atom Imaging

Krypton is an inert gas tracer commonly introduced into flow fields for a detailed understanding of the mixing process and subsequently to derive scalar dissipation rate through PLIF technique [17-19]. The Kr TPLIF is widely used for aerodynamics ground testing applications [14, 66], along with calibration proposed for H and N atoms in combustion diagnostics approaches [67]. Miller focused on several possible excitation schemes of Kr at 212.6 nm, 214.7

nm, and 216.6 nm and found that the emission signal at 212.6 nm was considerably weaker and that at 214.7 nm was higher than that at 216.6 nm [68]. The excitation scheme at 214.7 nm is popularly used for mixing studies in reacting [17, 19] and non-reacting flow fields [18] and flow tagging velocimetry [14]. Further, the excitation at 204.1 nm is particularly advantageous as it is easily accessible using a highly efficient, fs fourth harmonic generation scheme and has been used to determine the neutral density profile of helicon plasma [69], for calibrations during H and N LIF measurements [54, 67] and for mixture-fraction high-speed imaging in turbulent flows [70]. Further, Kr TPLIF has gained significant attention in 1D velocity measurement in hypersonic flow fields [14, 15] and mean temperature fields in reacting flows [71]. In recent years, Narayanaswamy et al. demonstrate a dual-wavelength excitation of Kr near 214 nm for 2D temperature imaging in a laminar non-sooting diffusion flame [16].

2.1.7 Prior Research on CH PLIF investigation

CH radical is one of the target species to investigate turbulent flame reactions which serves as a better species to locate the position of the flame front compared to OH radical even in complex flows. Initially, combustion researchers employed the same CH $A^2\Delta - X^2\Pi$ electronic bands near 431 nm for excitation and detection purposes [72, 73]. A major issue using this excitation scheme is that the fluorescence signal is spectrally close to the laser wavelength used hence the laser scattering must be suppressed effectively which could partially block the desired CH fluorescence; thereby, limiting fluorescence collection efficiency. Alternatively, blue-shifting the excitation wavelength to 390 nm as proposed by Carter et al. [74] facilitates the filtering of Mie and Rayleigh scattering interference which is also the scheme utilized in this study. The CH PLIF imaging measurements are performed by exciting $B^2\Sigma - X^2\Pi$ and detecting fluorescence from the A–X

and B–X (0,1) bands in the 420–440 nm range. The excited A state, υ'= 1 and 0 is populated via fast electronic energy transfer from state B (υ'= 0) [75]. The net fluorescence yield using B–X transition is significantly higher than that obtained by pumping A–X transition [75], thus higher signal level is observed in the B–X scheme. Most previous studies on CH B–X transition have utilized a 10 ns Nd: YAG pumped dye laser system with a narrow bandwidth (~ 0.1–0.5 cm^{-1}). Further progress has been made using this excitation-detection scheme to temporally resolve CH PLIF measurements by employing a frequency-doubled multimode alexandrite laser (~ 8 cm^{-1} bandwidth) [76] or an optical parametric oscillator (OPO) pumped by a custom Nd: YAG burst laser [24].

2.1.8 Prior Research on Molecular Nitrogen Detection

Figure 2.5 shows a schematic energy level diagram of the N_2 molecule along with some levels of N_2+ ion [77]. Nearly all the fluorescence emissions in air in the UV region originate from transitions of the second positive (2P) and first negative (1N) systems of N_2 or N_2^+ ions. The electron excitation of N_2 molecules plays a significant role in laser physics [28]. The excited states of N_2 are needed to be investigated and several kinds of literature are available that involved the N_2 molecules involving electron and photon impact followed by fluorescence or photoelectron detection [78-82]. Different laser diagnostics techniques such as Raman scattering and CARS are applied for pure spectroscopic investigation of the N_2 [83]. Heard [84] first reported oscillation in the ultraviolet wavelength at 337.1 nm, assigned to the 0–0 band of the Second Positive System (SPS). Kaslin and Petrash [85] and Massone et al. [86] observed lasing in the 0–0 and 0–1 (357.7 nm) bands. Fukuchi et al. [87] employed a nitrogen laser to excite N_2 molecules from $B^3\Pi_g$ state to the $C^3\Pi_u$ state and determined the $C^3\Pi_u$ state lifetime as well as transition probabilities of the

SPS. Zhang et al. [88] utilized the $C^3\Pi_u \rightarrow B^3\Pi_g$ transition of N_2 to measure the rotational and vibrational temperatures in nitrogen or nitrogen-containing plasma. Such utilization of SPS to study the gas temperatures is widely used [89-93].

Although the $C^3\Pi_u \rightarrow B^3\Pi_g$ transition has been studied extensively in the literature, the mechanism responsible for exciting the ground state $X^1\Sigma_g^+$ and populating the $C^3\Pi_u$ state is, however, not clear. Multiphoton excitation of molecules like N_2 molecule is a commonly used technique to overcome the limitations where the energy levels can't be probed by single-photon transitions [81]. Veen et al. [94] first reported the ground state N_2 molecules by using two-photon absorption by exciting $a^1\Pi_g(v' = 1) \leftarrow X^1\Sigma_g^+(v'' = 0)$ transition. Helvajian et al. [95] utilized the same two-photon transition to measure rotational population distributions in a pulsed supersonic expansion. Kaminski and Dreier [81] further investigated a–X (1,0) transition and observed a significant increase in the signal intensity with pressure for pure nitrogen. They attributed such behavior to the nonlinear susceptibility of the medium with photons resonantly absorbing excited state N_2 and ground state N_2^+ created due to the high laser intensity required for the multiphoton excitation scheme. Alden et al. [78] reported N_2 resonantly enhanced multiphoton ionization (REMPI) experiment using (2+3) photons with the $a^1\Pi_g$ intermediate states, followed by emission in the first negative system (FNS) of N_2^+ and possible N_2 molecules fluorescence detection. Lykke et al. [96] characterized the two-photon spectroscopy of N_2 molecule via $a''^1\Sigma_g^+ - X^1\Sigma_g^+$transition and reported the subsequent N_2 SPS LIF emission arising from the two-photon absorption at ~202 nm. Further studies are needed to better elucidate the excitation/ionization process to populate these excited states and detect the subsequent fluorescence emission which is the main idea behind this research.

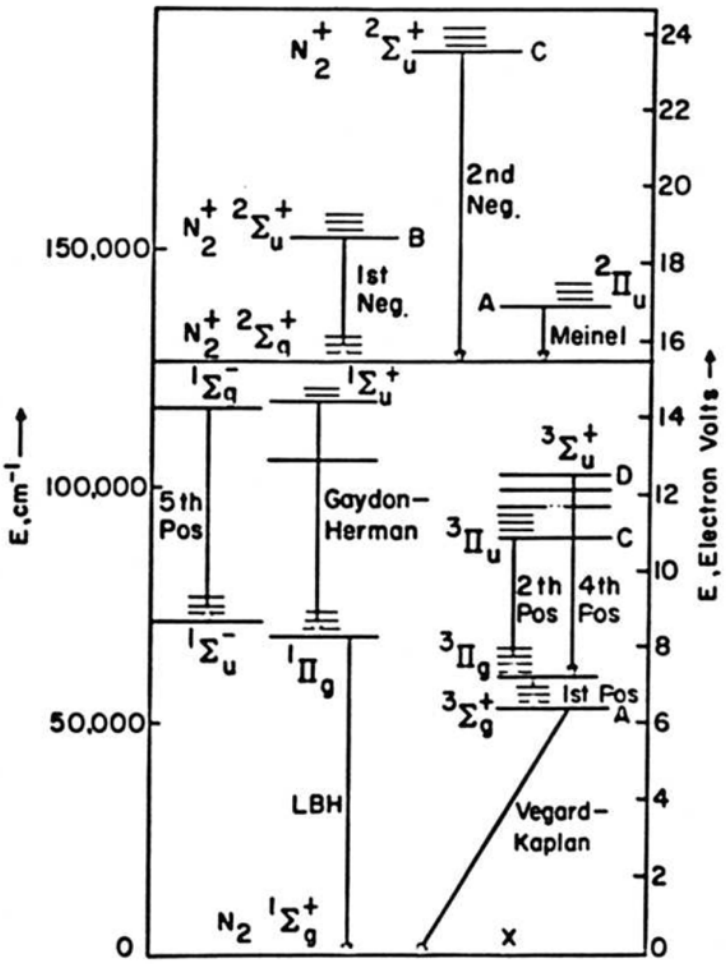

Figure 2.5 Electronic band systems of molecular nitrogen reprinted from [77].

2.2 Amplified Femtosecond Laser Systems

The first working laser was demonstrated in 1960 utilizing a powerful energy source to excite the atoms in a synthetic ruby [97]. Several genius minds prior and after to this date are often credited for today's laser and its wide range of applications. Prior to the 1960s', the shortest time duration measured was in the ns range. With the subsequent progress and constant advancement, production of light pulses in picosecond regime and eventually to lesser than 10 fs were possible after twenty odd years.

The ultrashort laser pulses are made up of light which is a form of electromagnetic radiation. All forms of electromagnetic radiation, including light is explained by a set of Maxwell's equations which is the relationship between the electric field **E** and magnetic field **H** [98]. The sets of equations are:

$$\nabla \cdot \mathbf{D} = \rho \tag{2.1}$$

$$\nabla \cdot \mathbf{B} = 0 \tag{2.2}$$

$$\nabla \times \mathbf{E} = \frac{-\partial \mathbf{B}}{\partial t} \tag{2.3}$$

$$\nabla \times \mathbf{H} = \mathbf{J} + \frac{\partial \mathbf{D}}{\partial t} \tag{2.4}$$

The relations defining D and B are

$$\mathbf{D} = \varepsilon_0 \mathbf{E} + \mathbf{P} \tag{2.5}$$

$$\mathbf{B} = \mu_0 (\mathbf{H} + \mathbf{M}) \tag{2.6}$$

Considering no free charges nor free currents are present in the space, we would have

$$\rho = \mathbf{J} = \mathbf{M} = 0 \tag{2.7}$$

Now, considering the electromagnetic wave propagation in linear, isotropic, source-free media taking curl of Eq. (2.3) and insert Eq. (2.4) leading to the famous equation [99]:

$$\frac{\partial^2 E(z,t)}{\partial z^2} - \frac{1}{c^2}\frac{\partial^2 E(z,t)}{\partial t^2} = \mu_0 \frac{\partial^2 \mathbf{P}}{\partial t^2} \tag{2.8}$$

Where, c is the velocity of light in free space. This equation is referred to as the Helmholtz equation which represents the propagation of light through a medium. The induced dielectric polarization **P** can be decomposed into linear and nonlinear part [99]:

$$\mathbf{P} = \mathbf{P}_L + \mathbf{P}_{NL} \tag{2.9}$$

$$\text{Where, } \mathbf{P}_L = \varepsilon_0 \chi^{(1)} \mathbf{E}, \tag{2.10}$$

$$\mathbf{P}_{NL} = \varepsilon_0 \chi^{(2)} \mathbf{E}^2 + \varepsilon_0 \chi^{(3)} \mathbf{E}^3 + \ldots \quad 2.11$$

$\chi^{(i)}$ are tensors

Assuming that the pulse is not intense enough to generate nonlinear behaviors, Eq. (2.8) can be approximated as [99]:

$$\frac{\partial^2 E(z,t)}{\partial z^2} - \frac{1}{c^2}\frac{\partial^2 E(z,t)}{\partial t^2} = \mu_0 \frac{\partial^2 \mathbf{P}_L}{\partial t^2} \quad 2.12$$

The decomposition of polarization in Eq. (2.9) is intended to understand how a polarization that varies linearly ($\mathbf{P}_L$) differs from the one that varies nonlinearly ($\mathbf{P}_{NL}$) with the field. $\mathbf{P}_L$is responsible for ordinary optics such as dispersion, diffraction, refraction, linear losses, and linear gain whereas $\mathbf{P}_{NL}$is responsible for nonlinear optics that includes saturable absorption and gain, Raman processes and harmonic generation [99-102]. The latter will be discussed later in detail in the section 2.2.3.

Mode-locked condition:

For multimode laser with an active gain linewidth $\Delta\omega_g$ and 2N-1 active mode separated by $\Delta\omega = 2\pi\frac{c}{L}$, we express [99] electric field as

$$E(t) = \sum_n A_n e^{i\phi_n} e^{i\omega_n\left(t-\frac{z}{c}\right)} \quad 2.13$$

Where, $A_n e^{i\phi_n}$ is the complex amplitude of the n^{th} mode. Changing the frame of reference, we get

$$E(t) = \sum_n A_n e^{i\phi_n} e^{i\omega_0 t + i\Delta\omega_n t} \quad 2.14$$

Where, $\omega_n = \omega_0 + \Delta\omega_n$ and $\omega_0$is the central wavelength. Separating the slowly varying term, $A(t) = \sum_n A_n e^{i\phi_n} e^{i\Delta\omega_n t}$ and a higher frequency term $e^{i\omega_0 t}$, the intensity can be written as [99]

$$I(t) \propto |A(t)|^2 = \left|\sum_n A_n e^{i(\phi_n + \Delta\omega_n t)}\right|^2 \quad 2.15$$

If the mode phases, ϕ_n are random, the resulting intensity profile takes an appearance of random spikes as shown in Figure 2.6 (left panel). Such behavior is called free-running mode with spikes having intensity fluctuation periodic in nature and the time duration inversely proportional to the total bandwidth of all the modes. However, if mode phases have a precise relation $\phi_{n+1} - \phi_n = \text{constant}$, then mode-locked condition is obtained, shown in Figure 2.6 (right panel). The time duration, periodic nature and average intensities are like that of free-running mode, and the main difference lies in the peak intensity of a mode-locked pulse which is enhanced by a factor N [98]. The advantages are that the possible instabilities are avoided, and the laser has the potential for lower noise.

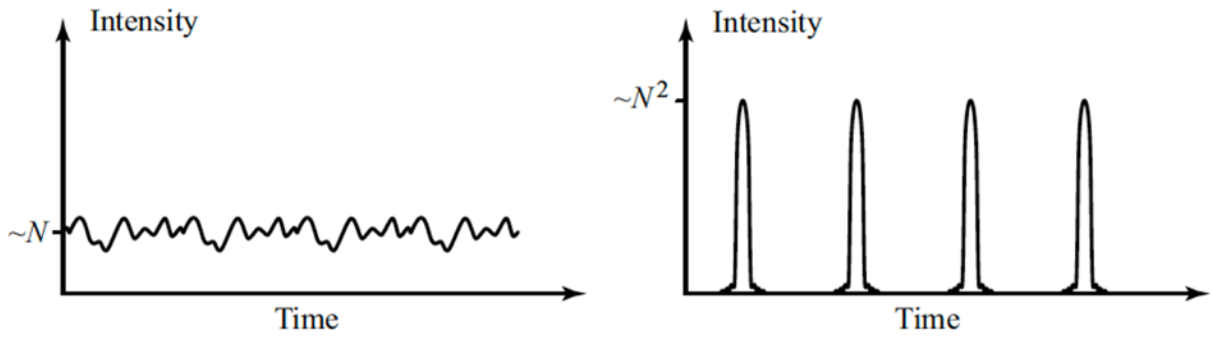

Figure 2.6 Laser output with randomly phased modes (left panel) and mode-locked phase (right panel) reprinted from [98].

Several approaches are used to obtain a train of mode-locked pulses from the laser systems. It includes active mode locking, passive mode locking, additive pulse mode locking and self-mode locking. As compared to the active mode-locking technique, the passive mode-locking technique generates much shorter pulses. It is accomplished by a saturable absorber (as indicated in Figure 2.7), driven by already short pulses, that responds to the instantaneous light intensity non-linearly.

Provided that the absorber has a sufficiently short recovery time, it can modulate the resonator losses comparatively much faster than an electronic modulator.

Figure 2.7 Schematic setup of a passively mode-locked laser reprinted from [103].

2.2.1 Construction Details

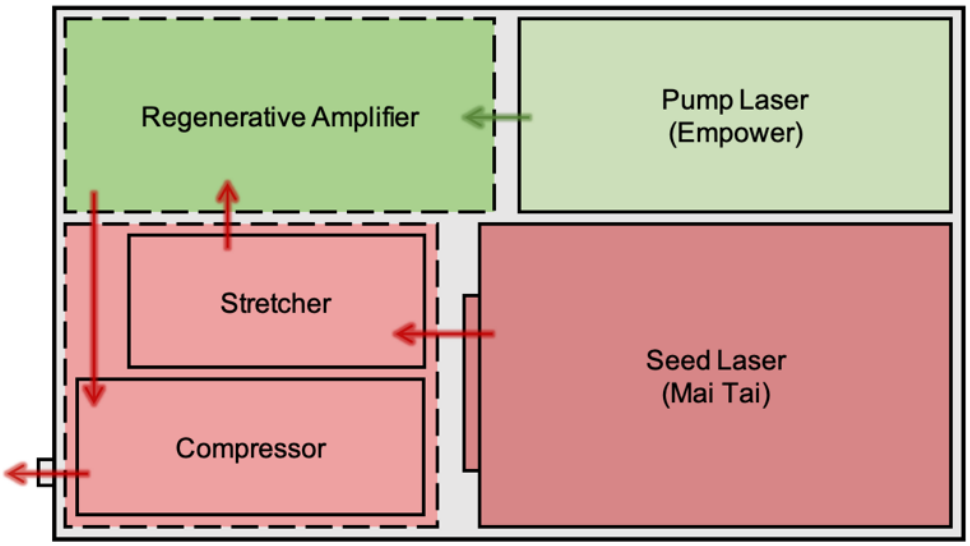

Figure 2.8 Block diagram of the fs laser system assembly.

Most of the fs laser systems are based on Ti:Sapphire and can be usually tuned in a small spectral range around 800 nm. Figure 2.8 shows the fs laser system assembly, capable of producing high-power, ultrafast pulses less than 100 fs in duration at a wavelength between 750-nm and 850-nm operating at a repetition rate of 1 kHz. The assembly consists of a Mai Tai seed laser, optical pulse stretcher/ compressor systems, a regenerative amplifier and an Empower pump laser to

energize the regenerative amplifier. The Empower pump laser is a Q-switched, frequency-doubled diode pumped, neodymium-doped yttrium lithium fluoride (Nd:YLF) laser that produces a pulsed, 527-nm green output beam used to amplify the pulses. It can produce pulse energy of 28 mJ for an average output of 28 Watts at 1 kHz. The Mai Tai comprises of two laser systems, continuous-wave (CW) diode-pumped laser and mode-locked Ti:Sapphire pulsed laser. In Mai Tai, neodymium-doped yttrium orthovanadate (Nd:YVO_4) laser crystal is the driving engine which absorbs the diode pump light and emits 1064 nm output beam, which resonates in the laser cavity and gets amplified through stimulated emission. The resulting 1064-nm beam is frequency doubled using a temperature-tuned lithium triborate (LBO) nonlinear crystal to obtain a 532-nm output beam which is an ideal pump source for the Ti:Sapphire laser because of its broad absorption band in the blue and green. The Mai Tai utilizes an acousto-optic modulator (AOM) to ensure reliable mode-locked operation as the laser starts up and delivers continuously tunable output over a range of near infrared (IR) wavelengths, from 750 to 850-nm operating at 80 MHz with pulse duration less than 100 fs.

2.2.2 Ultrashort Pulse Amplification

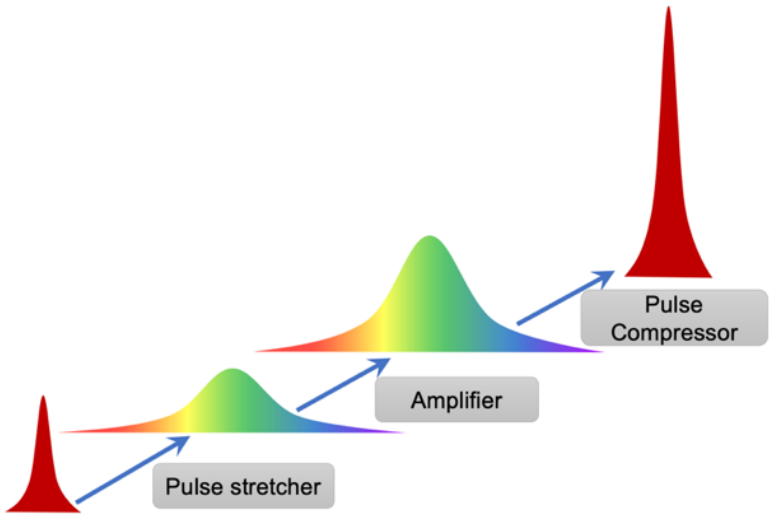

Figure 2.9 Principle of chirped pulse amplification.

The mode-locked laser generates a stable train of ultrashort fs pulses which has quite high peak power because of the inverse relation of peak power with the time duration. The high peak power of an ultrashort pulse causes nonlinearities to appear which can damage the gain material. Hence, "Chirped Pulse Amplification (CPA)" technique, illustrated in Figure 2.9, is employed to resolve this issue. This technique is completed in three steps – pulse stretching, regenerative amplification and pulse compression. The Solstice pulse stretcher (Figure 2.9) use a simple but elegant retroreflector mirror to direct the input beam onto a single diffraction grating, which causes the different frequencies to disperse. The grating and the routing mirrors are configured in such a way so that the bluer frequency components travel further than the redder components, and the pulse is said to be positively chirped. This causes the latter to exit the stretcher first, and the pulse is stretched by as much as 10^4. Once the train of mode-locked seed pulses enters the regenerative amplifier, a pulse is selected for the amplification process by a Pockels cell (Figure 2.9).

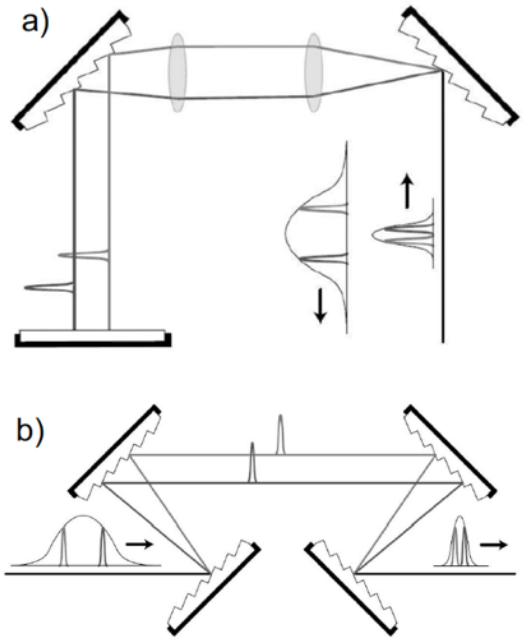

Figure 2.10 Principle of a stretcher (top panel) and a compressor (bottom panel) reprinted from [104].

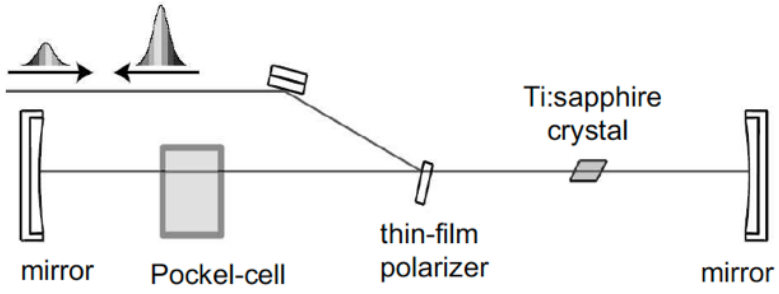

Figure 2.11 Schematic principle of a regenerative amplifier reprinted from [104].

A Ti:Sapphire crystal inside the amplifier, before the selected pulse enter into it, is excited to a condition of population inversion by a high energy pulse coming from the Empower pump laser. The selected seed pulse passes through the crystal multiple times until the pulse energy level is high enough to saturate the population inversion. A single Ti:Sapphire crystal amplifies an input

pulse having only a few nanojoules energy to several millijoules. The overall amplification through the regenerative amplifier is greater than 10^6 (solstice laser manual) at the output of the compressor. The pulse compression is the reverse of the pulse stretching where the optics are arranged such that the bluer frequencies take the shortest path and catch up with the redder components, thus compressing the pulse almost to its original pulse width with amplified peak power and it comes out of the laser box.

2.2.3 Frequency Conversion of fs Pulses

Once the chirped pulse amplification is completed, the high pulse energy supports non-linear conversion which is used to tune the frequency of the pulses to a required wavelength. In linear media, the polarization is proportional to the electrical field, whereas it is proportional to the square of the field for nonlinear media. Such nonlinear response causes an exchange of energy between several electromagnetic fields of different frequencies which can be applied for

i) Second harmonic generation: a part of the energy of an optical wave with frequency ω propagating through a crystal is converted to that of a wave at 2ω,
ii) Optical parametric oscillation: a strong pump beam at ω_1 causes a simultaneous generation of two waves ω_2 and ω_3 such that $\omega_1 = \omega_2 + \omega_3$.

Previously, we talked about the linear optics where properties of matter don't depend on the intensity of light. This usually occurs for low-intensity sources. For the peak power beyond the linear regime, the optical parameters become functions of the light intensity and the nonlinear polarization can't be ignored. Thus, Eq. 2.8 becomes [105]

$$\frac{\partial^2 E(z,t)}{\partial z^2} - \frac{1}{c^2}\frac{\partial^2 E(z,t)}{\partial t^2} = \mu_0 \frac{\partial^2 P_L}{\partial t^2} + \mu_0 \frac{\partial^2 P_{NL}}{\partial t^2} \qquad 2.16$$

Assuming a pulse electric field and P_{NL}as

$$E(z,t) = Re\{\mathcal{A}(z,t)e^{i(\omega_0 t - k_0 z)}\}l \quad 2.17$$

$$P_{NL}(z,t) = Re\{\mathcal{P}_{NL}(z,t)e^{i(\omega_0 t - k_p z)}\} \quad 2.18$$

Now, solving Eq. (2.16) with the help of the Fourier transform assuming the Slowly Varying Envelope/ Amplitude Approximation (SVEA) and neglecting the higher order terms, we reached to [105]

$$\frac{\partial \mathcal{A}}{\partial z} + \frac{1}{v_{g0}}\frac{\partial \mathcal{A}}{\partial t} - \frac{i}{2}GVD\frac{\partial^2 \mathcal{A}}{\partial t^2} = -i\frac{\mu_0\omega_0 c}{2n_0}\mathcal{P}_{NL}\mu_0 e^{-i\Delta k z} \quad 2.19$$

Where, $\frac{1}{v_{g0}} = \left.\frac{dk}{d\omega}\right|_{\omega_0} = k_0'$, $v_g = \frac{d\omega}{dk}$ being the group velocity (velocity at which the envelope of the packet travels through a medium). $GVD = \left.\frac{d^2k}{dw^2}\right|_{\omega_0} = k_0''$ Group Velocity Dispersion and $k_0$stand for k with $\omega = \omega_0$. $\Delta k = k_p - k_0$.

Harmonic generation:

When an intense laser beam passes through a suitable crystal, the electrical field of the beam interacts with the outer, loosely bound valence electrons of the crystal. This distorts the electron cloud, thereby polarizing the atoms at a frequency as that of the original beam and at its double frequency too (i.e., SHG), shown in Figure 2.12. The conservation of energy applies here and any gain in the SHG beam caused the decrease in the power of the original beam. Some crystals such as beta barium borate (BBO), LBO, potassium dihydrogen phosphate (KDP) allow almost 100% conversion of the original beam into SHG beam. The most common application of such phenomenon is observed in Nd-based laser system where IR output at 1064-nm is converted into green output at 532-nm, the most popular visible wavelength to pump Ti:Sapphire laser system.

In nonlinear optics, the first second harmonic beam was generated using a ruby laser focusing on a quartz crystal [106, 107].

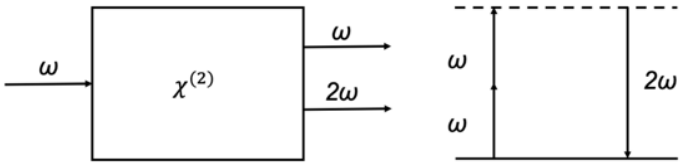

Figure 2.12 Second harmonic generation (SHG).

The efficient generation of second harmonic can be achieved only under a "phase matching" condition where Δk in Eq. (2.19) is equal to zero and constructive interference occurs between the polarization and input wave. If $\Delta k \neq 0$, the light at the new frequency gets reconverted to the original frequency and is not added in phase to create any sizable power. A suitable crystal temperature and orientation is chosen to resolve this issue and create the so-called phase matching condition where the phase velocities of the fundamental and second harmonic light are the same. The SHG process can be extended to THG and fourth harmonic generation (FHG) for further application. The THG is achieved by mixing an SHG beam with its fundamental beam to create the wavelength at one-third the incoming wavelength. Similarly, the SHG beam can be frequency-doubled to obtain FHG. Alternatively, mixing of THG beam with the residual pump beam on a fourth harmonic crystal to generate FHG is in practice as shown in Figure 2.13. Details on the construction and operation mechanism of alternate FHG scheme will be discussed in Chapter 3. All these harmonic generation processes are the frequency-mixing processes, where two coherent beams interact with each other to produce sum-frequency and difference-frequency generation (SFG and DFG, respectively). The harmonic generation can be applied to pulsed or ultrafast lasers

which have high peak power to achieve high conversion efficiency in a single pass through the harmonic crystal.

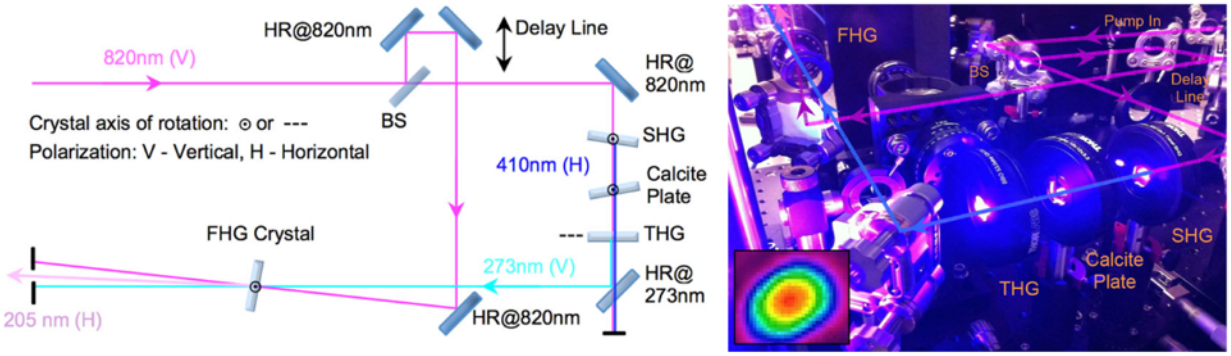

Figure 2.13 Schematic of the fs-FHG apparatus (left panel) with a typical UV beam profile at 1 m from the FHG crystal shown in bottom, left-hand corner (right panel) reprinted from [51].

Optical Parametric Generation:

In DFG, a single photon interacts with a suitable crystal and disappears, creating two photons of different frequencies. If one of the beams is stronger than the other, the energy can be utilized to amplify the less intense beam and hence, the process is called Optical Parametric Amplification (OPA). The strong beam is called pump, the weak one is called signal and the difference beam is called idler, as shown in Figure 2.14. This optical parametric generation process is beneficial as it generates two new tunable wavelengths, bound by the conservation of momentum and energy and by the refractive indices of the nonlinear crystal, n.

$$\omega_p = \omega_s + \omega_i \tag{2.20}$$

$$\frac{1}{n_p\lambda_p} = \frac{1}{n_s\lambda_s} + \frac{1}{n_i\lambda_i} \tag{2.21}$$

The phase matching for efficient OPA process occurs when the refractive indices of these three wavelengths i.e., n_p, n_s, and n_i satisfy the above momentum conservation equation in the crystal. This can be accomplished by selecting a suitable temperature or angle of the crystal, or the pump wavelength such that the phase matching takes place at the desired signal or idler wavelength.

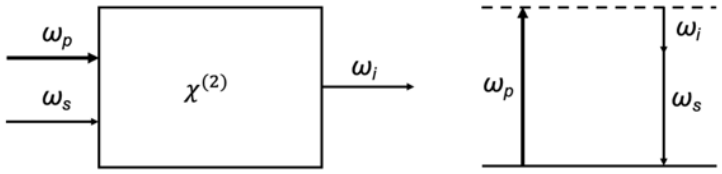

Figure 2.14 Optical parametric amplification (Subscripts p, s and i represent pump, signal, and idler respectively).

The optical parametric amplifier can emit coherent electromagnetic radiation in infrared and ultraviolet spectral regions when pumped by high peak intensity fs pulses. Several nonlinear crystals are used in the device for the generation of tunable pulses. The basic configuration of OPA process comprises of several steps: pump beam delivery, white-light continuum generator (WLG), a pre-amplifier, a signal beam expander-collimator, a power amplifier which are arranged in a single compact unit. Figure 2.15 presents the full layout of the device. Briefly explaining its operational procedure, a small fraction of the pump pulses at 800 nm is used to produce white-light continuum (WLC) in a sapphire plate which is focused into the pre-amplifier crystal along with another fraction of the pump beam. The parametric amplification taking place on these pulses are timed and overlapped non-collinearly inside the nonlinear crystal (NC1). The non-collinear geometry helps to block the residual pump beam and idler beams using a beam blocker after the crystal. The signal beam is expanded and collimated using a lens telescope and is then used for

power amplification stage which is pumped by the bulk of the input pump beam. The pump beam size is reduced and kept collimated after the telescope and is overlapped collinearly in the second nonlinear crystal (NC2) to generate well-collimated signal and idler beams.

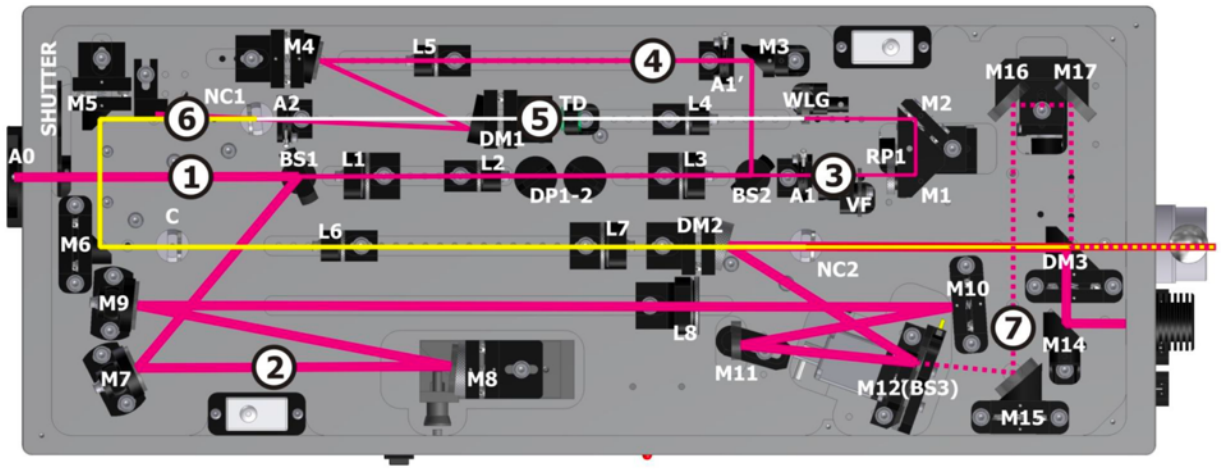

Figure 2.15 Full layout of optical parametric amplifier reprinted from [108].

The OPA process can produce tunable outputs anywhere from the mid-UV to the mid-IR but with low conversion efficiency as compared to direct SHG, THG, and FHG process. We reported approximately nine and four times higher third harmonic and fourth harmonic beam energy respectively as compared to the similar wavelength beam produced by OPA process [109].

2.2.4 Ultrashort Pulse Measurement

The unknown ultra-short laser pulse width is characterized by using Delta Autocorrelators which is based on SHG process. The delta single shot autocorrelator is constructed such that an input fundamental beam is first separated into two beams using a beam splitter. The two separated beams are reflected off two mirrors (M2 and M3) and then recombined at an equal cross angle in

a SHG crystal to generate the SHG signal, as shown in Figure 2.16. The measurement of pulse width requires two calibration processes: Calibration of the time and the Correction of the laser beam shape.

To obtain the pulse width, autocorrelation signal is observed on the oscilloscope and the time of the signal is calibrated. The time width of the signal, ΔS on the oscilloscope is measured. The peak position of the autocorrelation signal is changed by moving a translation stage and the change of time, ΔT is recorded. Then the pulse width of the laser beam, Δk is obtained using

$$\Delta\tau = (0.707 \cdot C \cdot L)\frac{\Delta S}{\Delta T} \qquad 2.22$$

where, the constant 0.707 is for the Gaussian nature of the pulse and C = 6 ps/mm is the time delay constant of the delay line for each millimeter moving distance L.

Gaussian beam has intensity distribution spatially which is why the correction of beam shape is required to obtain the real pulse width. The beam size correction is necessary if the peak intensity of the autocorrelation signal changes beyond 5% while moving the translation stage. The final pulse width after the correction is given by

$$\Delta\tau_0 = \Delta\tau \cdot \frac{\Delta S_2}{(\Delta S_2^2 - \Delta S^2)^{0.5}} \qquad 2.23$$

where, ΔS_2 is the time width between the two half peak intensity positions of the pulses on the oscilloscope.

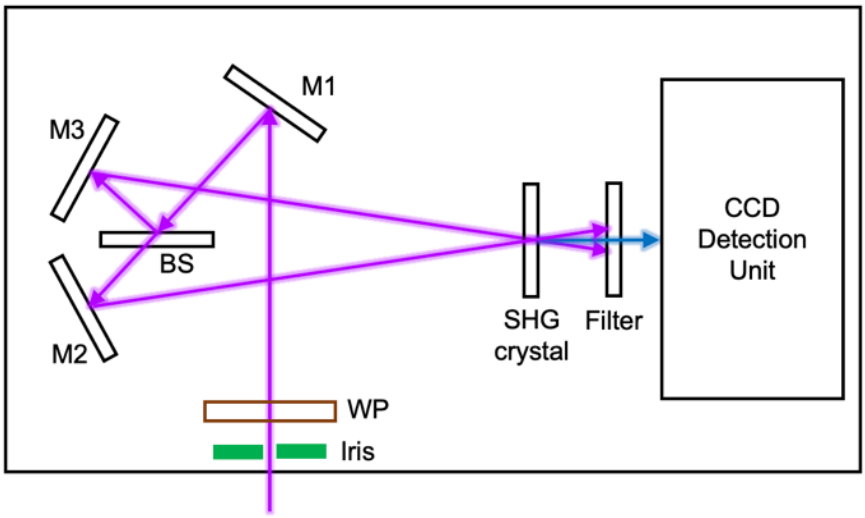

Figure 2.16 Ray diagram for pulse width measurement using optical autocorrelator. WP = waveplate, BS = beam splitter, M1, M2 and M3 are mirrors.

Spatial Mode:

Spatial intensity profile indicates the behavior of a laser beam in an application which is crucial for researchers or system designers. A beam profiler is used for the characterization of a laser beam that can measure the optical intensity distribution i.e., beam radius and the detailed shape. It helps to know precisely how the beam is behaving at the point of work and if the optics are having the desired effect. Knife edge scanners and camera-based systems are the most used beam profiler technologies depending on the wavelength, beam size and laser energy and the operating mode of laser (CW or pulsed). The knife-edge scanners are commonly used for CW lasers, smaller beams with high laser power while camera-based systems work well with large beams, and either pulsed or CW lasers.

2.3 Detection Instruments

PLIF technique is a variant of basic LIF technique which confines the laser illumination to a well-defined thin sheet within the flame region or plasma environment, thereby enabling the acquisition of spatially resolved species concentration. Typically, the fluorescence signal is recorded on an imaging sensor, as shown in Figure 2.17.

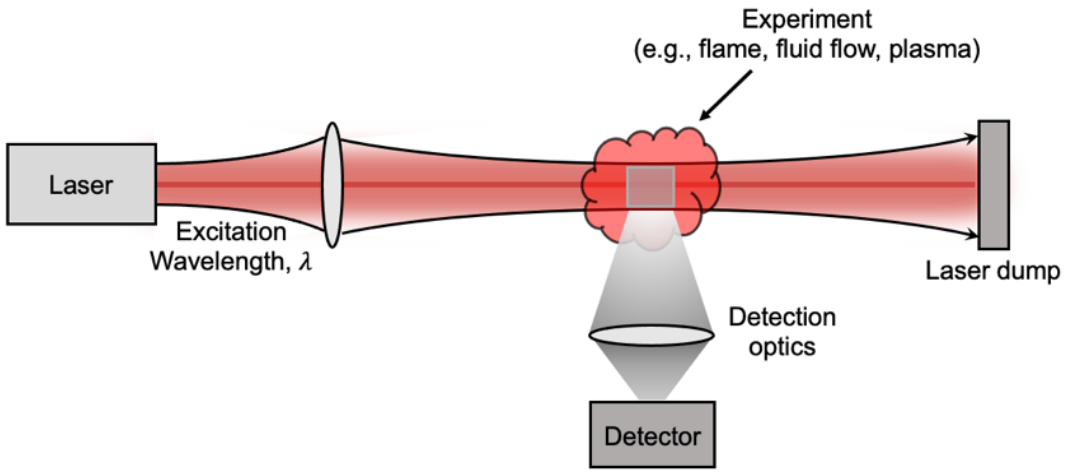

Figure 2.17 Schematic of laser-induced fluorescence technique.

2.3.1 CCD and ICCD Cameras

CCD and ICCD cameras are widely used to map out the spatial distribution of fluorescence emission from the species over time onto a 2D plane perpendicular to the laser sheet, shown schematically in Figure 2.17. They offer accurate time gating and synchronization with the pulsed excited laser source. Selected narrow bandpass filters are typically placed in the optical path of the emissions to select those wavelengths detecting the species of interest while rejecting the laser scattering and background due to fluorescence from other species.

CCDs are the imaging device that detects and counts the number of incoming photons and convert them to photoelectrons. These photoelectrons are shifted along the sensor to readout

registers where they can be amplified and digitized to display an image on the imaging software. ICCD cameras make use of a CCD sensor along with an intensifier. The intensifier consists of the electron multiplying component and the cameras can be used for low-light or single photon applications. The intensifiers are comprised of three components: a photocathode, a microchannel plate (MCP), and a phosphor screen. The photocathode detects the incoming photons generating electrons. These electrons are then accelerated to the MCP which converts them into a cloud of electrons which then travel to the phosphor screen into the fiber optic. These electrons are converted into visible light and detected by the CCD sensor.

2.3.2 High-Speed CMOS Cameras and Image Intensifiers

For the imaging applications that requires higher frame rates, Complementary Metal Oxide Semiconductor (CMOS) cameras are used instead of CCDs. Like CCDs, CMOS sensors are semiconductor image sensors that convert light into electrical signals. Use of modern sensor technology enables an ever-increasing image recording speed with maximum frame rates up to 22 kHz for full resolution or up to 600 kHz and more reduced resolution. For high-speed imaging with highest sensitivity and maximum image quality, a high-speed intensified relay optics (HS-IRO) is mounted in front of the CMOS high-speed camera. The working principle of the HS-IRO is like CCDs. The intensifiers amplify weak light signal and the whole camera-intensifier system is ideal for capturing highly turbulent flows in harsh combustion environments. The system can be utilized to capture the shot-to-shot variations while detecting the radicals in hydrocarbon flames.

2.3.3 Spectrometers

Spectrometer is another detection device which is trusted by researchers worldwide in spectroscopy applications for highly sensitive, aberration corrected spectral information. The main objective of any optical spectrometer is to measure the interaction (absorption, reflection, scattering) of electromagnetic radiation with a sample or the fluorescence emissions of the radiation from the sample. In principle, the spectrometer takes in light, break it down into its spectral components, digitize the signal with respect to wavelength, read out and display through software. At first, the fluorescence emission is directed through a fiber optic cable or optics combination into the spectrometer through a narrow aperture known as an entrance slit. Inside the spectrometer, the divergent light is then collimated by a concave mirror and directed onto a grating which disperses the spectral components of the light at slightly varying angles. These components are then focused by a second concave mirror and imaged onto the detector. In detection unit, the photons are converted into electrons which are digitized and read out through software. The emission signal is interpolated by the software based on the number of pixels and the linear dispersion of the diffraction grating to create a calibration to plot the obtained data as a function of wavelength over the given spectral range. The spectral information is used for numerous spectroscopic applications.

2.4 Laboratory Scale Burners for Combustion Research

2.4.1 Hencken Burner

Hencken burner is one of the widely used, commercially available flat diffusion flame burner. Typically, it is used as a calibration source for laser diagnostics measurements and has been used in the past for the application of optical diagnostic methods [61, 110-114]. General

construction of the burner shows that it consists of a square honeycomb-structured and uncooled burner holder which is divided into a central flow and co-flow, as shown in Figure 2.18. Fuel and oxidizer are injected into the alternating honeycomb channels within the central burner plate, as shown in Figure 2.19 with photograph shown in Figure 2.19. The fuel and oxidant rapidly mix with each other over the honeycomb and are burnt and hence the burner is considered as a semi-premixed burner. A non-flammable gas/ shield gas (e.g., N_2) is introduced through the co-flow section that surrounds the central core, shields, and stabilizes the flame.

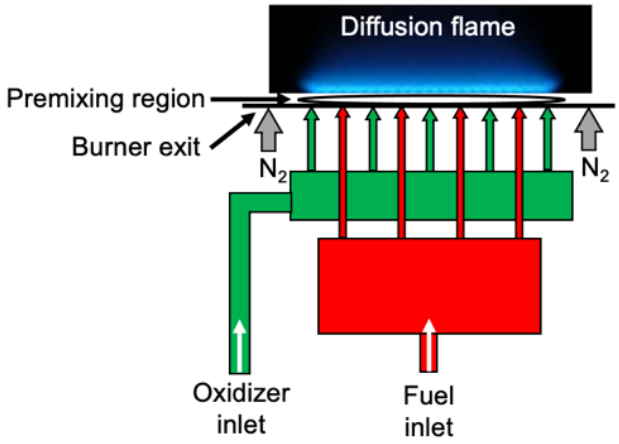

Figure 2.18 Schematic of Hencken burner.

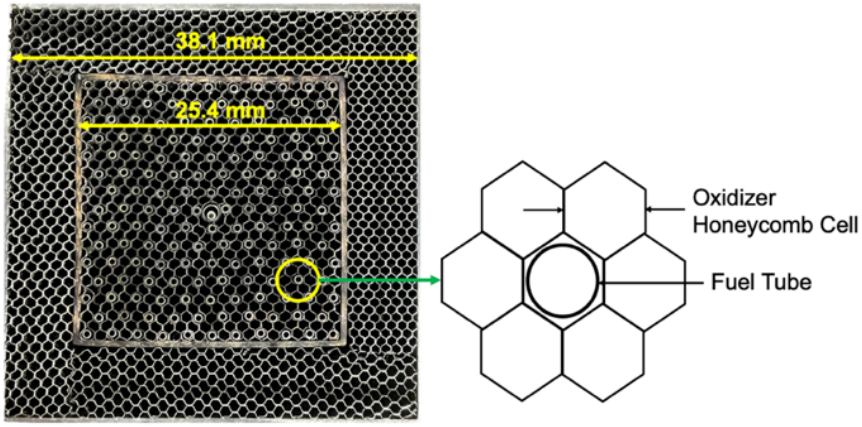

Figure 2.19 Hencken burner surface showing honeycomb-structure.

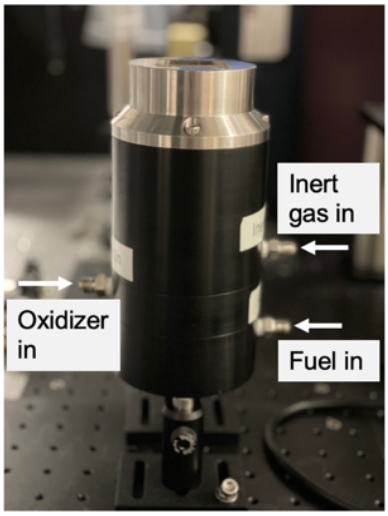

Figure 2.20 Photograph of the Hencken burner.

2.4.2 Modified McKenna Burner for Piloted Spray Flames

McKenna burners are widely used for combustion research to produce flat premixed flames [115, 116]. These premixed flames are assumed to be one-dimensional and considered as conventional and standard to perform optical diagnostics measurements. The premixed flames in rich conditions are frequently studied to understand the soot formation pathways. The optical

diagnostics measurements are performed along the flame axis assuming uniform distribution of temperature and concentration along the flame radius. The burner is in use in many laboratories around the world for the development and calibration of optical techniques [117-121]. The modified McKenna burner consists of 60-mm diameter stainless steel porous plug with a central tube allowing a passage for a central liquid fuel spray, thus supporting liquid-spray combustion too, as shown in Figure 2.21. Shown in Figure 2.22 is the side and top view of the burner. The liquid fuel is pumped into a glass nebulizer inserted into the tube and is atomized using high velocity gas (e.g., N_2). A premixed hydrocarbon/air flames is stabilized on the porous media to maintain the stable combustion of the liquid-fuel spray. Further, depending upon the stability, a guard flow is introduced through the sintered bronze annular region to reduce shear perturbations and stabilize the pilot and liquid-spray flames. Cooling water is flowed in and out of the burner to prevent the burner from overheating.

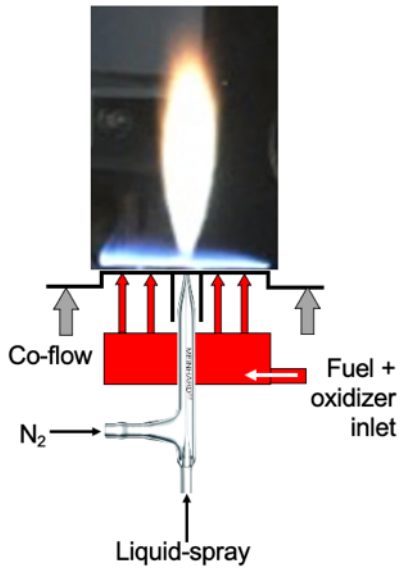

Figure 2.21 Schematic of McKenna burner.

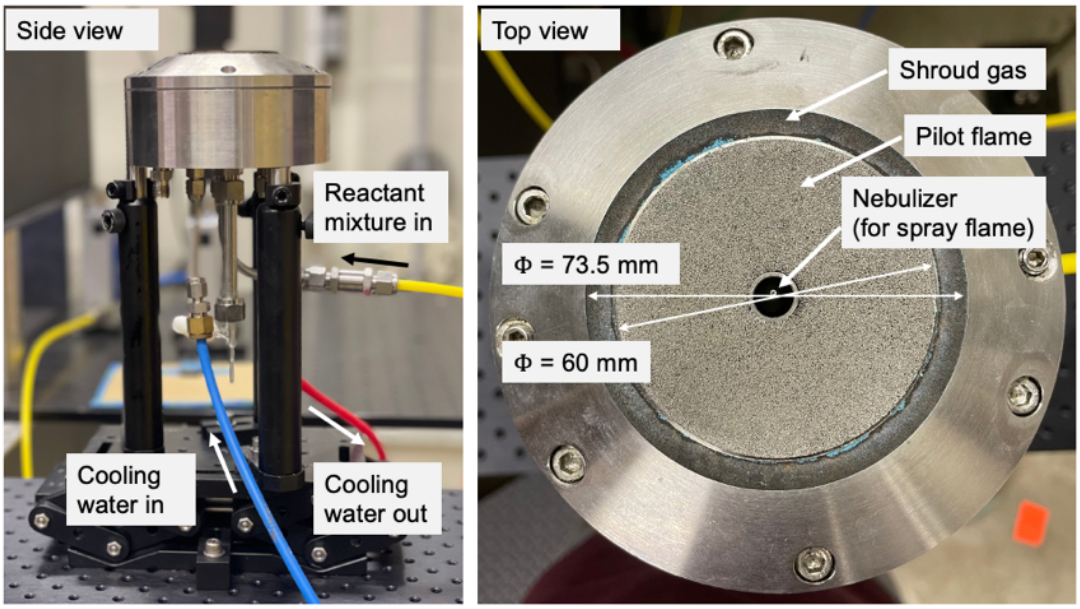

Figure 2.22 Photographs of the modified McKenna burner with a central nebulizer for spray flame experiments.

2.4.3 Bunsen Jet Burner

The Bunsen jet burner is also used in combustion research to produce laminar premixed conical flames. It consists of a single fuel tube of 4 mm inner diameter along with co-flow to shield the flame, as shown schematically in Figure 2.23. Shown in Figure 2.24 is the side view of the burner. A jet of fuel mixes with an oxidizer as it flows up through the tube. It can produce dual flame; fuel-rich premixed inner flame surrounded by a diffusion flame. The diffusion flame is resulted when carbon monoxide and hydrogen products from the inner conical region encounter the ambient air. The shape of the flame obtained is dependent on the combined effects of the velocity profile and heat losses to the tube wall. For the flame to remain stationary, the flame speed must be equal to the speed of the normal component of unburnt gases at each location, given by

$$S_L = v_u \sin\alpha \qquad 2.32$$

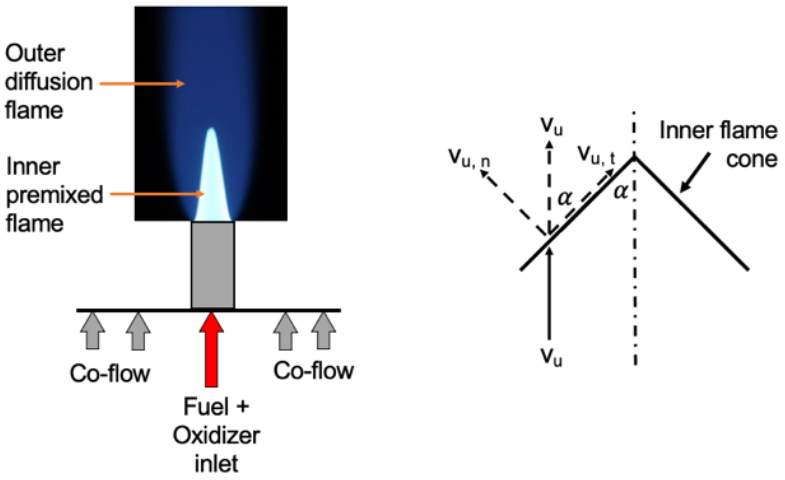

Figure 2.23 Schematic of Bunsen jet burner (left panel) and laminar flame speed equals normal component of unburned gas velocity (right panel).

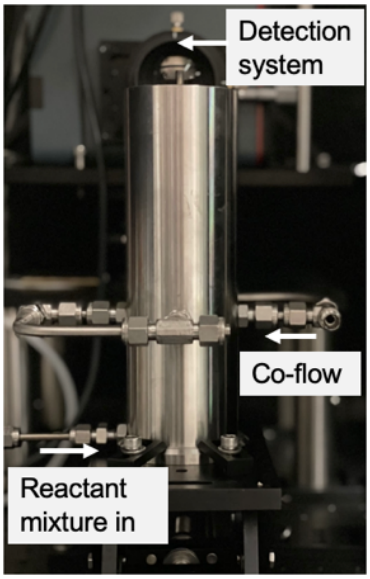

Figure 2.24 Photograph of the Bunsen jet burner for laminar flame experiments.

2.4.4 High-Pressure Burner

To conduct high-pressure measurements of intermediate species, a laboratory-scale high-pressure burner with an optical access is used, shown schematically in Figure 2.25 with photographs shown in Figure 2.25. The burner consists of two porous bronze rings, which are fed with a central premixed CH_4-air mixture and an annular air co-flow, respectively. The premixed flame is stabilized between the burner surface and a stainless-steel stagnation plate, maintaining a combustion region of approximately 11-mm tall in the middle. The annular air co-flow shields the central flame and further increases its stability. An additional N_2 co-flow was used to cool down the burner optical windows and prevent the water droplets from being formed on the window surface during the experiments.

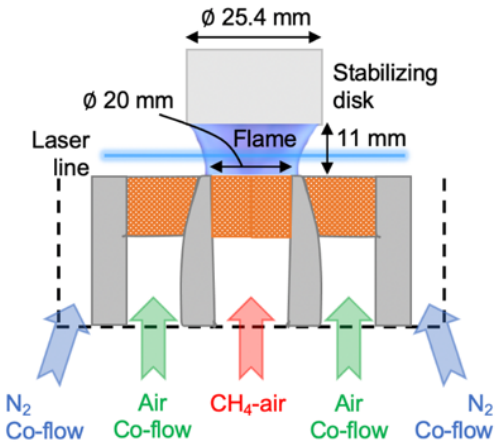

Figure 2.25 Schematic illustration of the high-pressure burner used in this study reprinted with permission from [123].

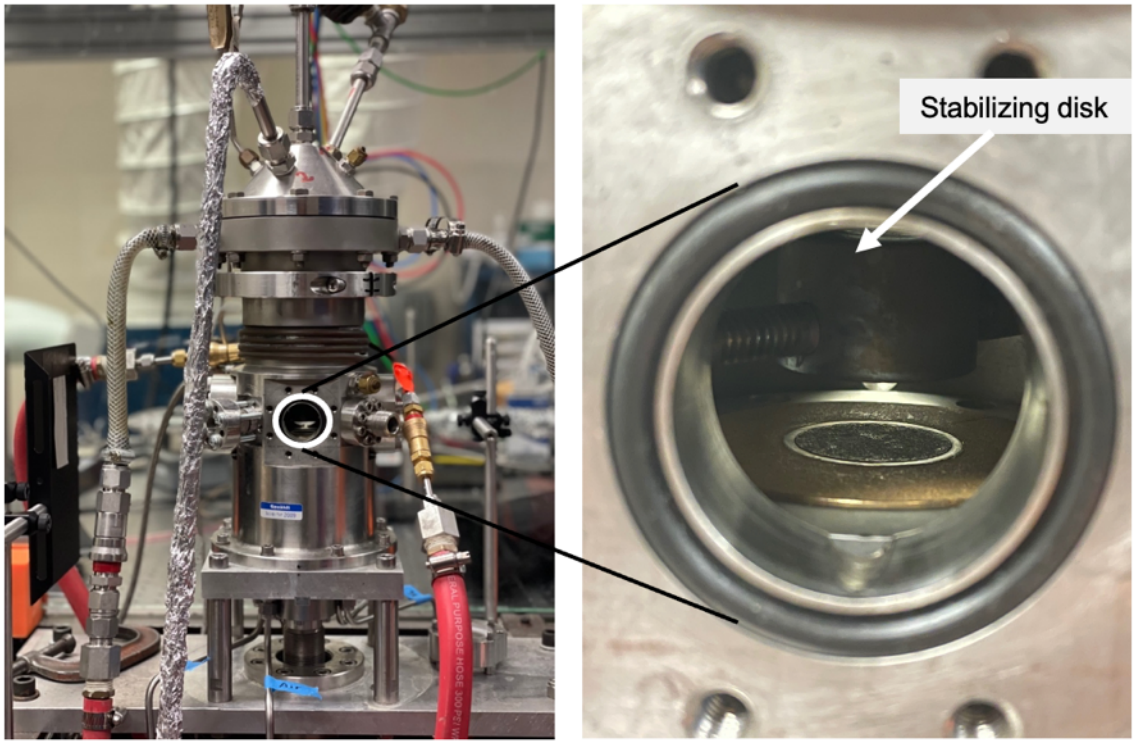

Figure 2.26 Photograph of assembled high-pressure burner along with enlarged view of burner surface and the stabilizing disk.

3. HIGH-PRESSURE HYDROGEN ATOM DETECTION*

3.1 Experimental Details and Procedure

3.1.1 High-Pressure Burner Configuration

The fs H-TPLIF measurements were performed inside an optically accessible laboratory-scale high-pressure burner, shown schematically in Figure 2.25. The detailed design configuration, operations, and flame characterization are explained elsewhere [122]. Briefly, the burner consists of two porous bronze rings, which are fed with a central premixed CH_4-air mixture and an annular air co-flow, respectively. The premixed flame is stabilized between the burner surface and a stainless-steel stagnation plate, maintaining a combustion region of approximately 11-mm tall in the middle. The annular air co-flow shields the central flame and further increases its stability. An additional N_2 co-flow was used to cool down the burner optical windows and prevent the water droplets from being formed on the window surface during the experiments.

3.1.2 Laser System and Imaging Apparatus

The schematic for H-TPLIF high-pressure measurement with a home-built FHG system is shown in Figure 3.1. The details of the FHG system, along with optics and crystals used to generate UV radiation, have been described in detail elsewhere [51]. Briefly, a regeneratively amplified Ti:Sapphire laser system (Spectra Physics, Model: Solstice Ace) generates fundamental output between 770–830-nm range with approx.. 80-fs-duration laser pulses at 1-kHz-repetition rate.

---

*Part of this chapter is reprinted with permission from "Femtosecond two-photon LF imaging of atomic hydrogen in high-pressure methane-air flames" by P. Parajuli, Y. Wang, M. Hay, V. R. Katta, W.D. Kulatilaka, Proceedings of the Combustion Institute (2022 in press). Copyright [2022] by The Combustion Institute. Published by Elsevier Inc.

As shown in Figure 3.1, the 820-nm laser beam with input energy ~2 mJ/pulse pumps the FHG system to generate UV radiation near 205-nm wavelength. The 10-mm diameter fundamental beam was down collimated to a diameter of ~4.5 mm through a telescopic combination of +200-mm/-90-mm lenses. This reduced diameter beam was guided to a 70/30 beam splitter, of which 30% is reflected off and sent through a delay line to be used later for the mixing stage. The remaining 70% transmitted beam passed through a SHG BBO crystal, a calcite plate, and a THG BBO crystal successively. The 3.3-mm thick calcite plate was angle tuned for fine-tuning of the delays to optimize the THG efficiency. The third harmonic beam was then overlapped and mixed with the other part of the fundamental beam at FHG BBO crystal in the final mixing stage to produce a 205.1-nm UV beam. The generated 205.1-nm UV beam is separated from the main, SHG, and THG beam after guiding through several dichroic laser mirrors. The output beam is approximately 3 mm in diameter and is focused into the probe region using a +200-mm lens after guiding through several 205-nm laser mirrors. The available UV beam energy was ~50 μJ/pulse (for ~2 mJ/pulse pump beam), and the energy reaching the burner was adjusted by using a thin, variable neutral density filter.

The H TPLIF signal was collected orthogonal to the direction of the propagation of the laser beam and was imaged for (1) shot-averaged H-atom fluorescence signal in high-pressure flames using an intensified charge-coupled device (ICCD) camera (Princeton instruments, PI-MAX4); and (2) single shot H-atom measurements in atmospheric flame using high-speed CMOS camera (Photron, SA-Z)/ Electron Magnifying CCD (EMCCD) camera coupled with a high-speed intensified relay optics (HS-IRO) intensifier (LaVision, HS-IRO). Each detection systems were fitted with a 50-mm focal length f/1.2 Nikon visible camera lens along with a narrow bandpass filter centered at 656-nm to block unwanted interferences and laser scattering. An additional +60-

mm focal length plano-convex lens (P/N LA1401-A) was placed towards the detection side close to the burner window to increase the collection solid angle and hence maximize the fluorescence signal collection efficiency which is extremely important for high-pressure flames. The spatial resolution was 55 µm/pixel (ICCD), 25 µm/pixel (CMOS) and 45 µm/pixel (EMCCD) and was found to be uniform in both horizontal and vertical directions.

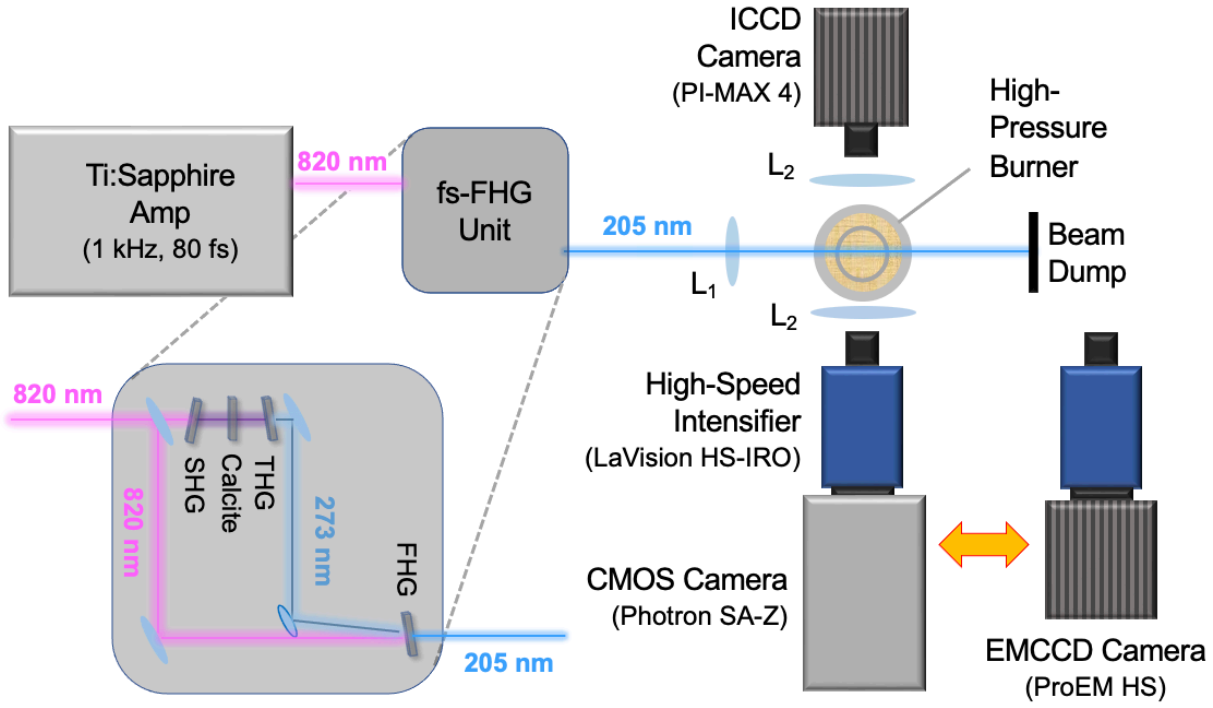

Figure 3.1 Schematic of the high-pressure H-TPLIF experimental apparatus reprinted with permission from [123]. L_1-Focusing lens, L_2-Detection lens, SHG-second harmonic generation, THG-third harmonic generation, FHG-fourth harmonic generation.

3.2 Results and Discussion

3.2.1 Laser Transmission Characterization

As briefly discussed in the introduction section, one major difficulty with high-pressure H measurements was absorption losses through thick optical windows. The maximum available pulse energy at 205-nm from a commercial OPA system is ~10 μJ/pulse when using 6-mJ of pump beam (~ 0.17% conversion efficiency at 205-nm). Most part of this energy gets absorbed while passing through the 14-mm thick quartz entrance window of the pressure vessel, making the energy available for high-pressure measurements insufficient. The home-built FHG system improved the conversion efficiency (~2.5% at 205-nm), and the available pulse energy at the burner entrance was ~50 μJ/pulse when pumped with only 2-mJ/pulse of the 820-nm fundamental. A detailed energy absorption study was performed and is plotted in Figure 3.2 along with the calculated transmission efficiency. The transmission efficiency decreased from ~80% to 20% when the pulse energy was increased from 1–50 μJ/pulse due to energy-dependent nonlinear effects of the quartz window material and MgF_2 focusing lens with centerline thickness of approx. 3 mm. A detailed investigation on the laser energy attenuation was conducted and the results are presented in Figure 3.3. As seen from this study, the focusing lens and window have ~50% and ~40% transmission, respectively, at the peak laser energy of 50 μJ/pulse, hence the resulting overall transmission is ~20%. It should be noted that the beam diameter was maintained close to 4.5 mm on the entrance window by placing the focusing lens right against the window holder. As seen from Figure 3.2, roughly ~12 μJ/pulse is available inside the burner, which is sufficient for shot-averaged H measurements at elevated pressures.

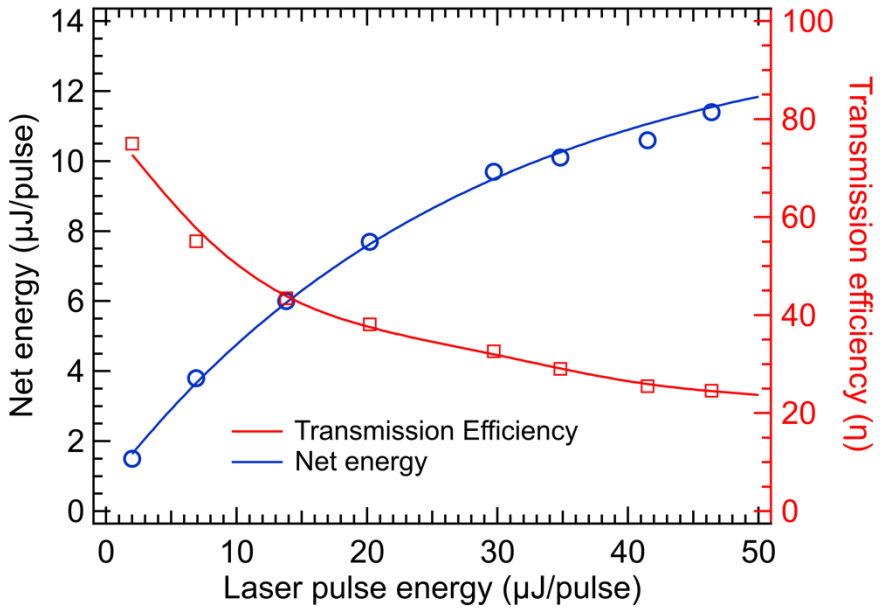

Figure 3.2 Laser energy absorption effect due to the thick burner window in terms of absolute power and transmission efficiency reprinted with permission from [123].

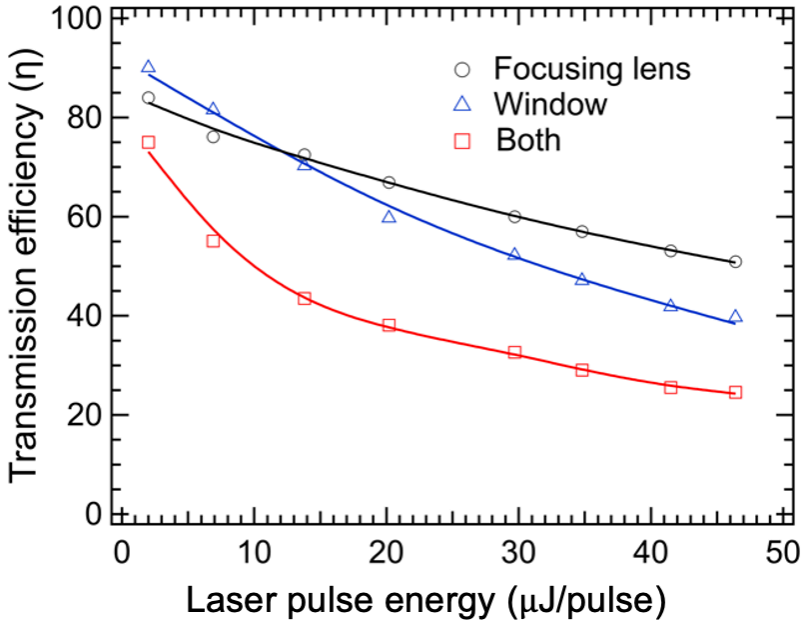

Figure 3.3 Laser energy attenuation due to focusing lens, window, and combination of both reprinted with permission from [123].

3.2.2 Excitation-detection Signal Analysis

Shown in Figure 3.4 is the dependence of the H signal on the excitation wavelength, recorded in an atmospheric-pressure CH_4/air flames of ϕ =1.2. An intensifier gate width of 10 ns and 100% gain were used. On-CCD accumulation of 1000 was used, and a set of 100 such images were recorded at each wavelength. The excitation wavelength was measured using a fiber-coupled spectrometer (Ocean Optics, Model: Flame S). The wavelength plotted is blue-shifted by +0.5-nm based on the theoretical excitation wavelength of 205.1 nm to account for a device calibration error. The laser convoluted excitation bandwidth is ~0.6 nm, full-width-at-half-maximum (FWHM). Sample on-resonance (at 205.1 nm) and off-resonance (at 207.6 nm) images are shown in the insets. A residual signal of less than 5.0% is present on both sides of the main peak, which is expected to come from nonuniform wings of the laser spectrum (i.e., sidebands). Also shown by the red curve is the on-resonance laser spectrum with a broad spectral bandwidth of ~1.5-nm (FWHM).

H TPLIF emission signals were recorded for four different pressures for a range of laser pulse energies at a height above the burner (HAB) of 3 mm, as shown in Figure 3.5. The pulse energy values plotted are those reaching the probe volume. Ideally, a two-photon excitation scheme should result in quadratic dependence of fluorescence yield on the laser pulse energy. The high-energy UV laser, however, could photolytically generate additional H, leading to a higher than quadratic energy dependence [45]. Figure 3.5 shows no apparent deviation from quadratic dependence in all four pressures below ~11 μJ/pulse, suggesting no evidence of photolytically created H.

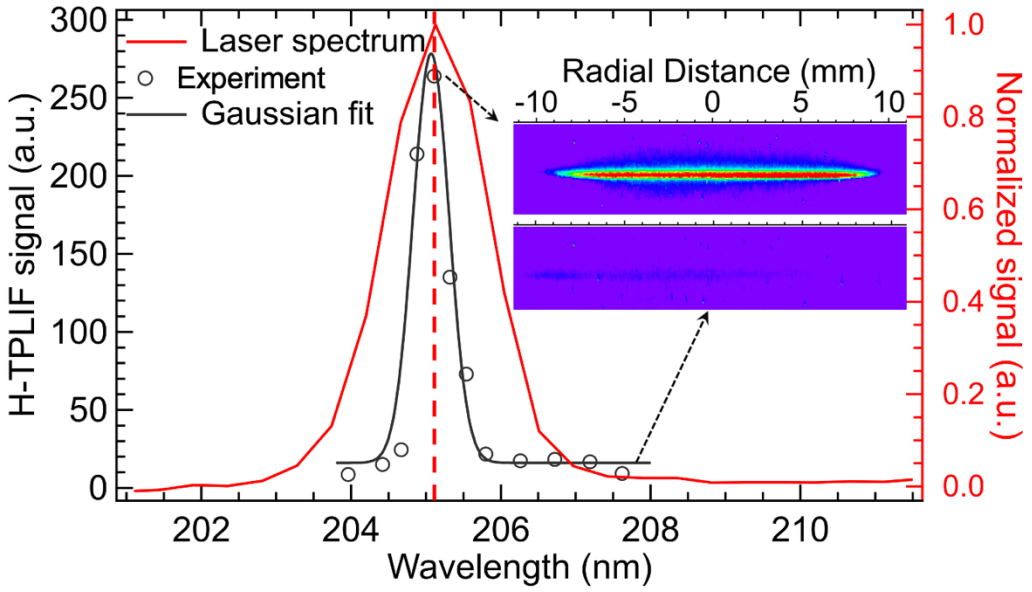

Figure 3.4 Fs H TPLIF signal dependent on the excitation wavelength, recorded in the ϕ =1.2 CH_4/air flames at 1 bar reprinted with permission from [123]. Sample on- and off-resonance images are shown in the inset along with on-resonance laser spectrum. The color distribution is based on a rainbow color palette with red and purple being maximum and minimum signals, respectively.

Therefore, the laser energy was held constant at 10 μJ/pulse for the remaining experiments, except for the amplified spontaneous emission (ASE) detection studies. Partial saturation may be evident beyond 11 μJ/pulse for 1, 2 & 5 bar cases but is absent in the 10-bar case, likely due to increased laser beam attenuation at higher pressures. This data also showcases the H TPLIF signal drop with increasing pressure. The symbols are experimental measurements, and the solid lines are quadratic power-law fits. The error bars are 2-sigma standard deviations of 100-line images. The observed quadratic dependence also suggests that the photoionization and ASE can be negligible in the flames investigated. ASE would have resulted in sub-quadratic laser energy dependence.

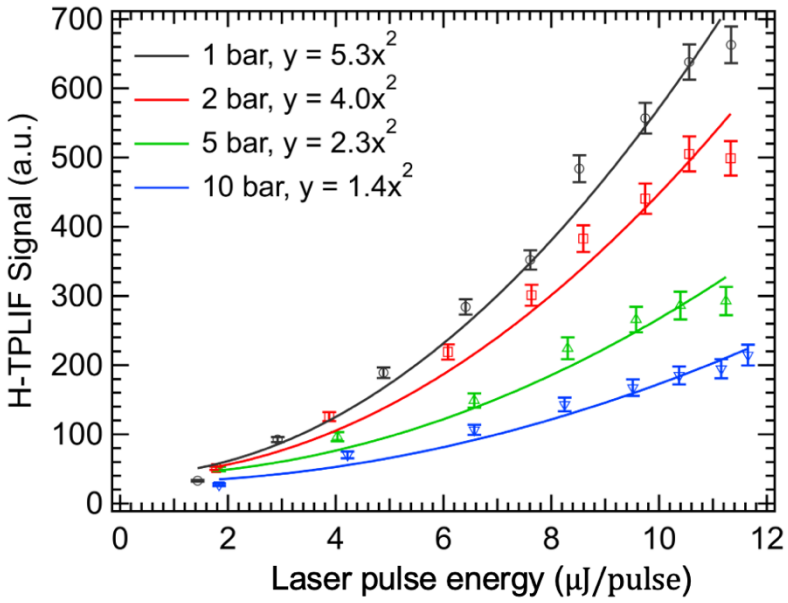

Figure 3.5 Laser energy dependence of the fs-TPLIF signal of H, recorded in a ϕ =1.2 CH_4/air flame at HAB = 3 mm at pressures of 1, 2, 5, and 10 bar reprinted with permission from [123].

Generation of ASE was further investigated using a photodiode with a UV attenuation filter placed along the laser beam path outside the burner exit window, and the results are shown in Figure 3.6. As indicated by the flat red curve in the inset of Figure 3.6, we did not observe any ASE in the fully assembled high-pressure burner for all pressures investigated; hence it can be concluded that all high-pressure measurements reported here are ASE interference-free. However, an ASE peak could be detected near 656-nm when the burner entrance window was removed, and the flame was operated at 1 bar. No ASE was observed for lower pulse energies up to 4 μJ/pulse, and a sharp onset of ASE generation was observed thereafter. Recall that Jain et al. [62] also observed a similar ASE trend in atmospheric-pressure jet flames. This observation indicates the excited state population loss through ASE at higher energies resulting in less intense fluorescence

signals. However, with the addition of the window material, the laser pulse gets stretched in time for the same pulse energy and is expected to eliminate ASE generation.

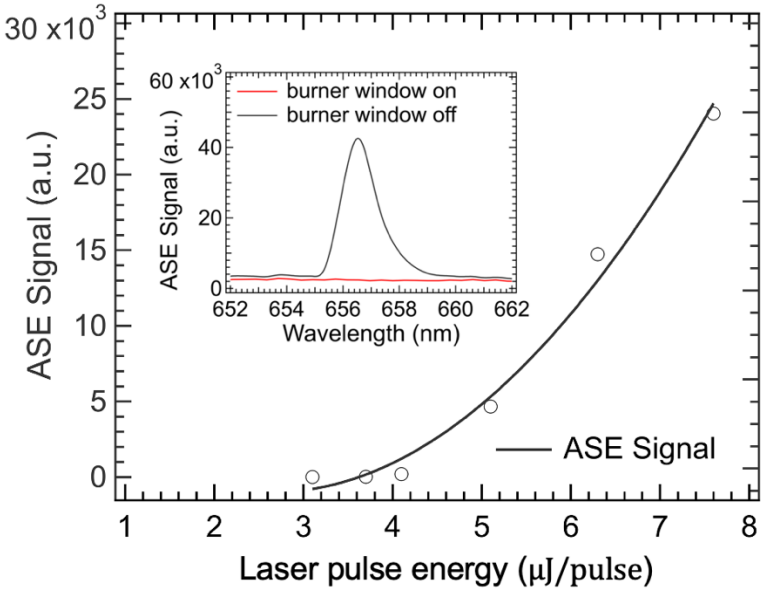

Figure 3.6 Two-photon ASE recorded as a function of laser energy in ϕ =1.2 CH_4/air flames at P = 1 bar reprinted with permission from [123]. The ASE can be avoided with the burner window on, as shown by the signals in the inset.

3.2.3 H-atom TPLIF Pressure Scaling: 1–10 bar

To investigate the applicability of the fs TPLIF scheme in flames at elevated pressures, the H signal was recorded as a function of pressures up to 10 bar in premixed CH_4/air flames at ϕ = 1.2. Ideally, the H TPLIF signal should scale linearly with the increasing H number density with pressure in flames at equilibrium conditions. However, the H TPLIF signal decays rapidly with the increasing pressure, as depicted by closed circles in Figure 3.7. The solid line is a curve simply connecting the data points to guide the eye. It is observed that the signal reduced by approximately

a factor of four when the pressure is increased from 1–4 bar and remained nearly constant thereafter up to the pressure of 10 bar.

It was already confirmed that the signal losses due to photoionization and ASE are insignificant for the current experimental conditions. Hence, the collisional quenching and fluorescence signal trapping are the dominant loss mechanisms with increasing pressure. Generally, the fluorescence signal scales approximately as the inverse of the quenching rate. We estimate quenching rates in the current flames using the room-temperature rate coefficients for N_2, O_2, H_2, H_2O, CO_2, CO, CH_4, and C_2H_2 and assuming that the coefficients are temperature-independent [124]. The mole fractions of these species and temperatures in the flames were calculated using a well-documented, axisymmetric CFD code with detailed chemical kinetics known as UNICORN (Unsteady, Ignition, and Combustion using Reactions) [125]. UNICORN is a time-dependent, axisymmetric mathematical model that has been developed in conjunction with the experiments for predicting ignition, extinction, stability limits, and the dynamic characteristics of non-premixed and premixed flames. It solves for *u*- and *v*-momentum equations, and continuity, and enthalpy- and species-conservation equations on a staggered-grid system. CFD calculations for the flames in our high-pressure burner were performed using a 401×101 grid system. The code predicts super equilibrium concentrations for radical species such as H and OH. Heat transfer through the stabilizing disc is included but not the catalytic effects. Plots of streamlines suggest that the flame is stabilized in the diverging flow field as expected for a stagnation flame. The calculated quenching rates are then applied to the H TPLIF signals, and the resulting trend is plotted in open circles in Figure 3.7. The dashed line is a curve simply connecting the data points to guide the eye. As seen, collisional quenching accounts for a certain degree of the nonlinear decay of the fluorescence signal with pressure. Hence, other processes such as laser beam

attenuation and fluorescence signal trapping are assumed to account for the remaining signal losses, which need to be accounted based on the particular burner geometry for accurate quantitative TPLIF measurements.

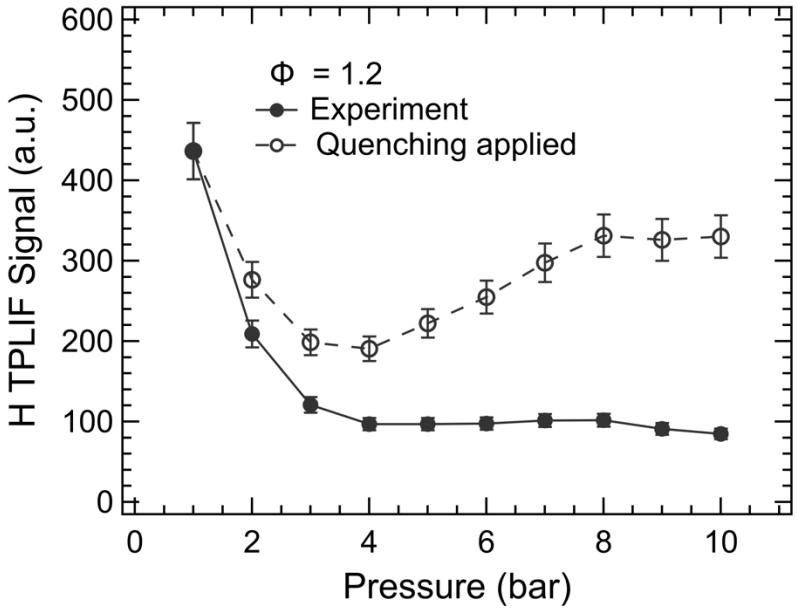

Figure 3.7 Pressure dependence of fs TPLIF signal of H, recorded in ϕ =1.2 CH_4/air flames reprinted with permission from [123]. Each data point corresponds to the spatially averaged fluorescence signal over the entire line image across the flame at HAB= 3 mm.

Further, the fs H TPLIF scheme was applied to measure the experimental H-atom signals as a function of ϕ in premixed flames at pressures of 2, 5, and 10 bars. The results are compared with the equilibrium H number densities and local H concentrations calculated using the Cantera [126] and UNICORN [125] codes respectively. The Cantera (0D calculation) and UNICORN calculations use GRI-Mech 3.0 and USC Mech II kinetic mechanisms, respectively. The corresponding results are shown in Figure 3.8. The model curves are adjusted appropriately to

intersect the experimental H-atom signal with the Cantera profile at ϕ =1.2. At lower pressure of 1 and 2 bar, the signal count increases with increasing ϕ. This trend is in good agreement with the calculated profiles up to ϕ =1.2. However, a continuous increase in the experimental H signal levels is observed on the rich end as opposed to decreasing predicted trend. A part of the increasing experimental signal may be due to interference from soot incandescence [53], although super-equilibrium H concentrations might also be possible in these flames. With the further increase in ϕ, the flame tends to liftoff and flame structure changes, so the upper end of ϕ was limited to 1.3. In future studies, better characterization of such soot interferences is recommended by subtracting off a background signal recorded at the detuned laser wavelength but at the same flame condition.

The experimental H signal shows an opposite trend at higher pressures (5 bar and 10 bar) as compared to the Cantera and UNICORN calculations. The experimental signals decrease as ϕ increases up to near stoichiometric conditions and remain nearly flat thereafter. It is worthwhile noting that the experimental SNR is very low, near ~1.2 for higher-pressure fuel-lean cases, although the observed 2-sigma uncertainty remains nearly the same throughout. An additional challenge for such high-pressure cases arises from the increasingly luminous background at 5 and 10 bars arising from the stabilizing disk. Such increasing luminous background along with super-equilibrium H concentrations could have contributed to the observed trends. These behaviors of high-pressure H TPLIF signal with ϕ needs to be investigated further. It should also be noted that laser beam absorption and fluorescence trapping could change as the ϕ is changes, even at a given pressure. Such variations need to be accounted for during quantitative signal comparisons in future studies.

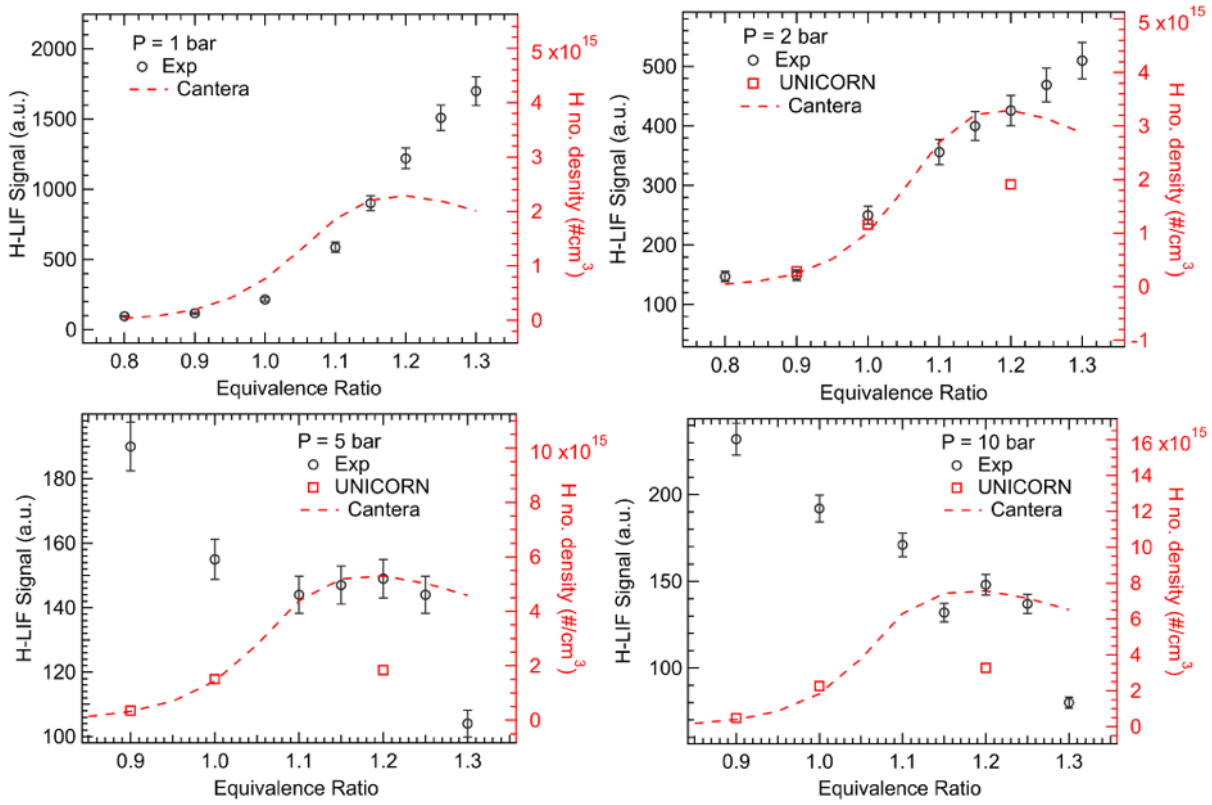

Figure 3.8 Fs H TPLIF signal as a function of ϕ in CH_4/air flames at pressures of 1, 2, 5, and 10 bar reprinted with permission from [123]. Dash lines and red markers represent the calculated equilibrium H number density using Cantera and UNICORN code respectively. Both measurements and UNICORN model prediction are the integrated signal obtained at HAB of 3 mm.

3.2.4 Line and 2D Imaging Results

H TPLIF line images are radial profiles derived by vertically integrating across the line images in ϕ =1.2 CH_4/air flames at pressures of 2, 5, and 10 bar are shown in Figure 3.9. These

images are corrected by subtracting the background recorded with the laser beam blocked. The UV laser beam was propagated through the probe region from right to left of the image. The beam waist is estimated to be ~0.300 mm from the recorded line images; hence, the fluence is ~0.014 J/cm^2 for the 10 μJ pulse. All three plots indicate that the primary chemical reactions take place in the middle region of the flames, where fuel-rich combustion occurs. Small peaks of H TPLIF signals are observed near the periphery of the flame because of the extra supply of air through the annular co-flow, which increases the flame temperature by generating near-stoichiometric flow conditions.

The TPLIF signals are found to be in good agreement with the local H concentrations obtained from the UNICORN model. The radial H TPLIF signals are nearly flat in the premixed middle region at the P=2 bar case. The experimental signal in the middle region, however, shows a minor decrease on the left side at 5 and 10-bar cases, suggesting increased UV laser attenuation across the flame. It should also be noted that the flame structure tends to become non-uniform as the pressure is increased, as evident by previous chemiluminescence and OH PLIF studies in the same burner [122]. As compared to the model predictions, the experimental H-atom profiles get marginally broader with increasing pressure, which can be due to increase in the buoyancy-driven flame flickering. Such effect increases with the increase in fuel flow rates and operating pressure condition [127].

Several line images were also recorded at P=2 bar ϕ =0.9 and 1.2 flames at different heights by translating the burner vertically. The 2D H profiles shown in the right halves of Figure 3.10 are assembled from 20 vertical line images, each separated ~0.35-mm while vertically translating the burner. They are then compared with the UNICORN code predictions as shown by the left half of the images. A satisfactory qualitative agreement is observed for both flames. The signal counts are

multiplied by a factor of 6 for ϕ =0.9 flame for better visualization. The model overestimates the flame edges due to nitrogen co-flow, whereas the experimental H signals are concentrated more towards the center of the flame. The H TPLIF signals are stronger at the bottom of the flame and become weaker with HAB, which is also predicted by the model. The reduced H signal close to the SS disk could be due to strong flame-wall interactions and wall quenching effects. It should be noted that the H measurements presented here are only semi-quantitative. In follow-on applications, a detailed calibration scheme such as by seeding Krypton [20] can be used to convert the experimental signals into the quantitative H number densities. Such process would require a thorough understanding of the quenching rates, concentrations of major colliders, temperature distributions, as well as knowledge of non-radiative decay processes, laser beam attenuation, and fluorescence trapping.

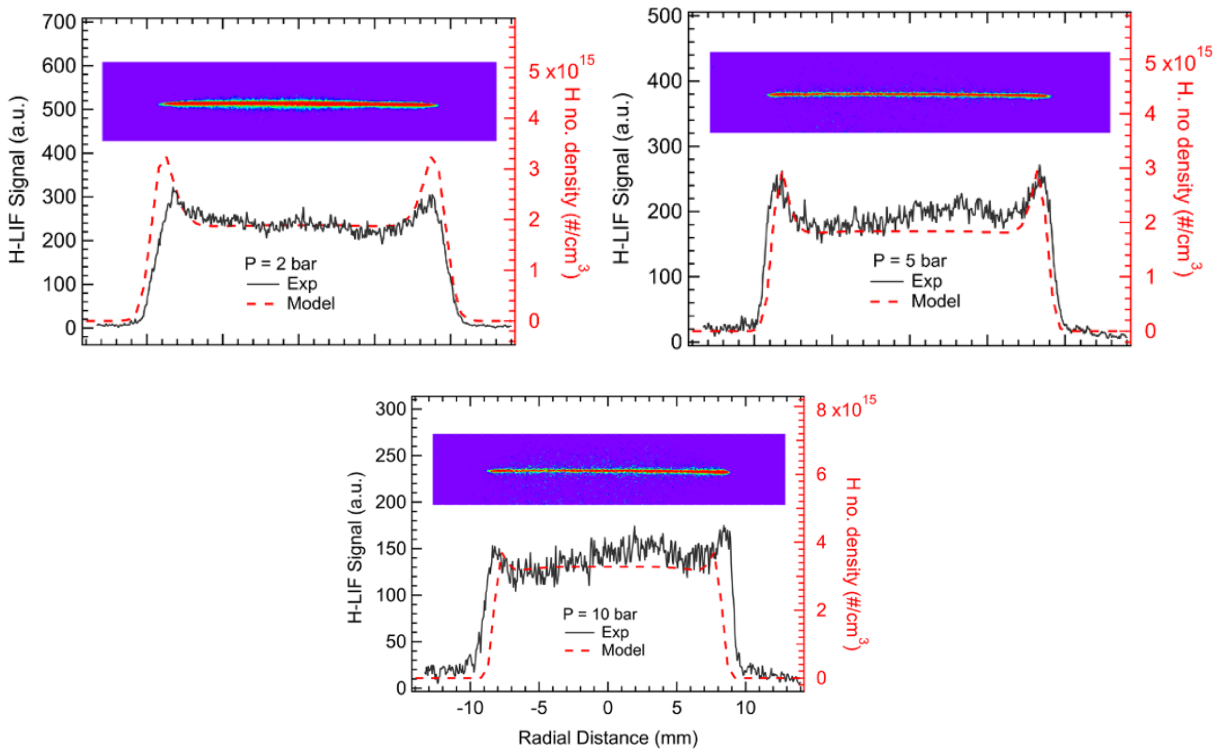

Figure 3.9 Fs H TPLIF radial profiles in ϕ =1.2 CH_4/air flames at pressures of 2, 5, and 10 bar reprinted with permission from [123]. Corresponding line images are shown on the top of each frame.

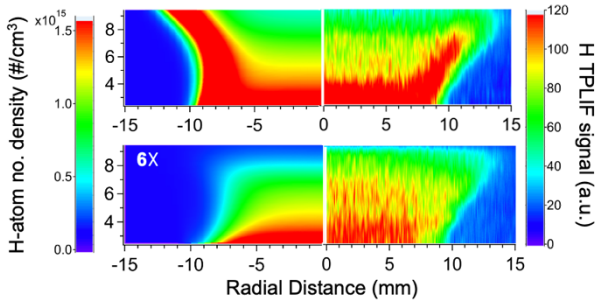

Figure 3.10 Stacked H TPLIF line images recorded in ϕ =1.2 (top) and ϕ =0.9 (bottom) in CH_4/air flames towards the right half compared with that corresponding H no. density contour obtained from UNICORN towards left half reprinted with permission from [123].

3.2.5 Progress Towards Single-shot H Imaging

Two detection systems: high-speed CMOS/IRO and EMCCD/IRO systems were used for single-shot, kHz-rate H TPLIF imaging measurements in an atmospheric flame. Unfortunately, it was not possible to demonstrate single-shot imaging at high-pressure with current laser and imaging setup. In both systems, the IRO intensifier gain was set at 70%. The IRO gate width of 200 ns and 40 ns were used for CMOS and EMCCD setup respectively. For CMOS system, reduction in intensifier gate didn't improve the SNR significantly, hence it was set to 200 ns just to ensure we are not losing laser pulses for excitation. For EMCCD camera, the Electron-Multiplying (EM) gain, and gate were set to 1% and 150-ns respectively. The UV camera lens and the spectral filter were the same as those used for the ICCD detection system.

Figure 3.11 & Figure 3.12 present 1-kHz H TPLIF sample images recorded for ϕ =1.2 and 0.9 CH_4/air flames at an atmospheric pressure for CMOS and EMCCD setup respectively. It is clearly indicated that the signal level is significantly weaker for the CMOS/IRO system as compared to that for the EMCCD/IRO system. Towards the right, in both Figure 3.11 & Figure 3.12, are the fluctuations in signal level with respect to shot# and the percentage of signal variation with the mean count is shown at the top panel. The signal level varies within ±25% of the mean value for rich flame as compared to -50% to +100% for lean case in case of CMOS/IRO system. However, the signal level is much more consistent and varies within ±12% of the mean value for both flames while using EMCCD/IRO setup. This is due to extreme low sensitivity of the CMOS camera which can capture the H-signal above certain threshold values only. Additionally, the SNR of the single-shot LIF images was determined as the ratio of the signal and the background over a 10 mm × 0.3 mm region. On comparison, the peak and mean SNR were calculated to be ~17 and ~15 for ϕ =1.2 flame for EMCCD/ IRO system as compared to ~ 1.8 and ~ 1.6 only for CMOS/IRO

system, possibly causing the signal level to have wide variations in latter case. It is evident that the high-speed EMCCD/IRO detection system is comparatively effective for H TPLIF imaging applications. As the EM gain was increased to 5%, the peak and mean SNR were calculated to be ~53 and ~49. Thus, we can claim that the SNR can be further improved by increasing the EM gain of the EMCCD camera.

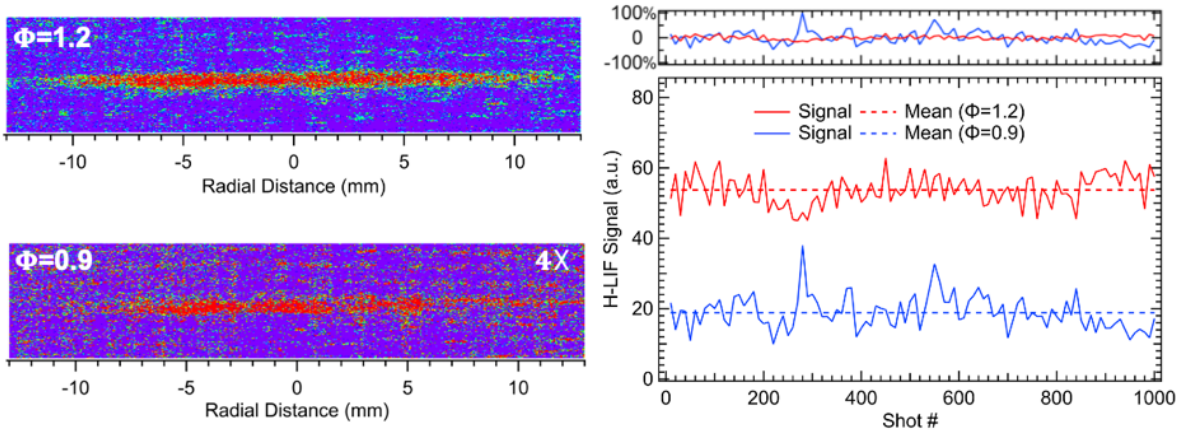

Figure 3.11 Sample single-laser shot fs-TPLIF H images recorded using CMOS/IRO system in ϕ =1.2 (top) and ϕ =0.9 (bottom) in CH_4/air flames towards the left with integrated line signal variation versus shot# towards the right reprinted with permission from [123].

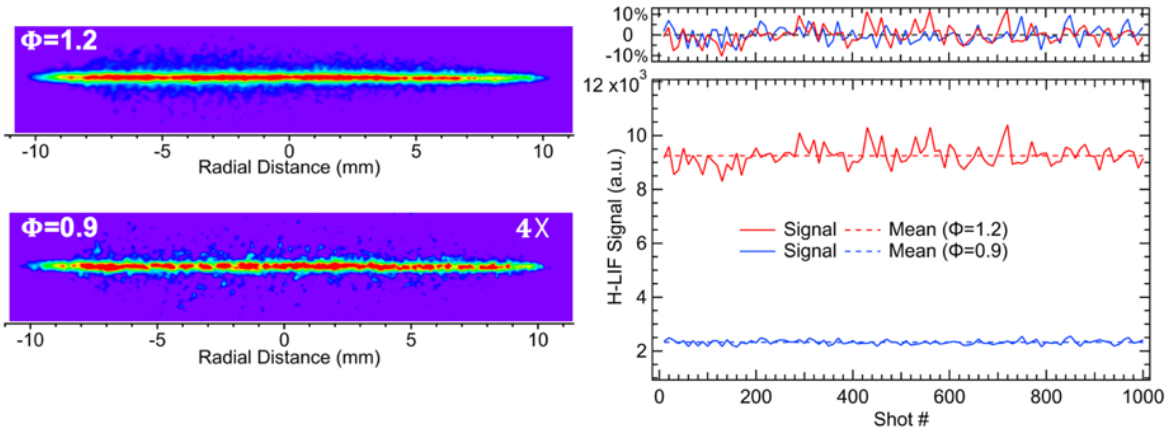

Figure 3.12 Sample single-laser shot fs-TPLIF H images recorded using EMCCD/IRO system in ϕ =1.2 (top) and ϕ =0.9 (bottom) in CH_4/air flames towards the left with integrated line signal variation versus shot# towards the right reprinted with permission from [123].

It is worthwhile to mention that these single-shot measurements were recorded with laser input window off; hence, the power at the probe region was maintained at ~30 μJ/pulse resulting in better SNR. Recall from Figure 3.2 that the power drops by 5× at the peak energy with the introduction of the input window, resulting in a ~25× drop in signal (i.e., quadratic energy dependence), and hence single-shot measurements were not feasible at high pressure under present conditions. In the future, the UV laser energy available at the probe region can be increased by using high-transmission ultrafast optical window materials such as MgF_2. Additionally, the current FHG setup was operated with only 2 mJ/pulse of pump energy, adding a buffer on the BBO crystal damage threshold. The pump beam diameter can be increased on FHG optics to utilize the maximum available pump energy of 6 mJ/pulse (or higher). It is estimated the fourth-harmonic laser energy can be increased by 3× (or higher), and hence, 9× or more increase in the TPLIF signal can be expected. The significant increase in the laser energy, however, can result in additional

complications such as ionization and dielectric breakdown in the beam focus. These complications can be minimized by allowing for laser pulse-stretching while transmitting through the window and lens to increase the pulse duration and hence reduce the peak intensity. Such improvements along with highly efficient transmissive optics (MgF_2), and high-quantum efficiency EMCCD cameras, although yet to be realized experimentally, could enable the kHz-rate single shot H TPLIF imaging in high-pressure flames.

3.3 Summary and Recommendations

In this work, we have demonstrated TPLIF for H imaging in high-pressure flames up to 10 bar using a high-conversion-efficiency fs FHG laser system. Detailed investigations are performed on the laser transmission losses through pressure vessel windows, followed by characterizations of different measurement challenges such photoionization, photolytic interferences, and background chemiluminescence. A quadratic dependence of the H TPLIF signal on the laser pulse energy was confirmed up to pressures of 10 bar. Negligible SE interferences are reported, potentially resulting from fs pulses being stretched by the burner window. The pressure-dependence study showed a rapid decrease of the fs H TPLIF signal with increasing pressure as opposed to the expected linear increase in the H number density. Quenching corrections and other potential signal loss mechanisms are discussed. The measured H fluorescence signal variations as a function of ϕ are well predicted by Cantera and UNICORN flame models at lower pressures (1 & 2 bar); however, significant discrepancies are observed at higher pressures. Potential mechanisms for such deviations are outlined. TPLIF line images recorded at different flame heights and generated 2D H maps are reasonably well predicted by the UNICORN flame model. The present laser energy was insufficient for single-shot imaging at kHz rates; however, strategies

for increased signal levels and detection sensitivity in future experiments are discussed. Overall, the TPLIF technique, combined with efficient fs FHG laser system, is a promising diagnostic approach to H atom imaging in high-pressure combustion environments.

4. THERMOMETRY TECHNIQUE BASED ON KRYPTON TWO-PHOTON LASER-INDUCED FLUORESCENCE*

4.1 Experimental Procedure

The experimental apparatus shown in Figure 4.1 includes a fs laser system, camera configuration and the burner configuration. All the experimental runs were conducted in two types of flame (i) an atmospheric-pressure Bunsen flame of $CH_4/O_2/N_2$ mixture established on a 13-mm inner diameter stainless-steel tube (ii) a high-pressure flat flame of premixed CH_4-air mixture and air co-flow at pressures up to 10 bar. Around 5% Kr tracer gas was introduced to the mixture gas line. The fs laser system consists of a frequency-tunable, regeneratively amplified 1-kHz Ti:Sapphire laser (Spectra Physics, Solstice Ace). The ~80-fs-duration (FWHM) fundamental output near 820 nm was used to pump a custom-built FHG unit to obtain deep ultraviolet (DUV) radiation centered at 204.1 nm [16]. The DUV output beam was guided through several dielectric laser mirrors and focused onto the probe region using a +500-nm focal length lens. Kr-TPLIF line images were recorded orthogonal to the laser beam direction using an intensified charge-coupled device (ICCD) camera (Princeton Instruments, PIMax IV). The ICCD camera was fitted with a 50-mm focal length f/1.2 Nikon visible camera lens and a bandpass filter (Semrock, FF01-832/37-50). Kr emission spectrum was also monitored in the 750–840 nm range by using a spectrometer/camera combination (Princeton Instruments Isoplane160/PIMax IV) to ensure the signal collected through the filter bandwidth consisted of only Kr emission peaks [11].

---

*Part of this chapter is reprinted with permission from "Evaluation of LIF Thermometry technique using Krypton as a tracer: Impact of laser lineshape and collisional bandwidth" by N. Lamoureux, P. Parajuli, W.D. Kulatilaka, P. Desgroux, Proceedings of the Combustion Institute (2022 in press). Copyright [2022] by The Combustion Institute. Published by Elsevier Inc.

Interference due to the fundamental laser wavelength at 820 nm was removed during data processing by subtracting a background image. The absence of ASE was checked, and measurements were performed in the quadratic regime of LIF.

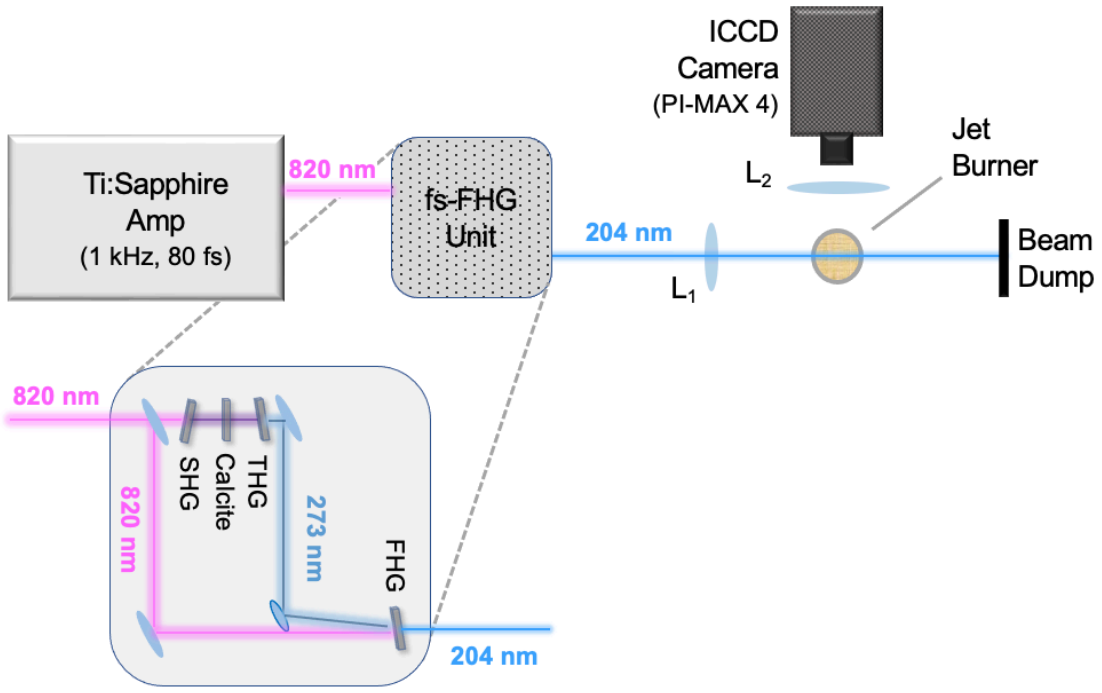

Figure 4.1 Schematic of the Kr TPLIF experimental apparatus. L_1-Focusing lens, L_2-Detection lens, SHG-second harmonic generation, THG-third harmonic generation, FHG-fourth harmonic generation.

4.2 Theory Behind Kr Thermometry

Krypton is excited from the ground state $4p^6\ {}^1S_0$ to the excited level $5p'\ {}^1D_2$ at 97945.16 cm^{-1} via a two-photon absorption at 204.13 nm. The TPLIF signals collected during the experiment include 5p to 5s emission transitions at 811 and 826 nm [11]. According to Refs [18, 23][128], the

time-integrated TPLIF signal of Kr, S_{Kr}, that is temperature-dependent, can be expressed as a function of the Kr density [Kr] as follows:

$$S_{Kr} \propto g(\Delta\bar{\nu}) \frac{A_{32}}{A_3+Q_{Kr}} [\mathrm{Kr}](I_\nu)^2 \quad 4.1$$

Here $g(\Delta\bar{\nu})$ is the normalized line profile of the two-photon excitation, which is composed of the convolution of the effective laser line profile and the atomic absorption line A_{32} is the spontaneous emission rate along $3\rightarrow 2$, A_3 is the total spontaneous emission rate of the $n = 3$ excited level, and Q_{Kr} is the total quenching rate. A_3+Q_{Kr} is the total depopulation rate of the upper level or the fluorescence decay rate. I_ν is the laser intensity at the wavenumber ν. To extract the temperature, we need to consider the temperature dependence of Q_{Kr}, $g(\Delta\bar{\nu})$ and [Kr]. In isobaric flows, [Kr] scales as X_{Kr}/T, where X_{Kr} is the Kr mole fraction. Hence, Eq (4.1) becomes [128]:

$$S_{Kr} \propto g(\Delta\bar{\nu}) \frac{A_{32}}{A_3+Q_{Kr}} \frac{X_{Kr}}{T} (I_\nu)^2 \quad 4.2$$

The conversion of the fs TPLIF signal into temperature profile requires only the knowledge of the quenching rate along the radial axis. Since the bandwidth of the fs laser is so large, the variation in $g(\Delta\bar{\nu})$ across the flame can easily be neglected. Hence, assuming a $T^{-0.5}$ dependence of Q_{Kr} and neglecting the variation of X_{Kr}, Eq. (4.2) simplifies to [128]:

$$S_{Kr} \propto (T)^{-0.5}(I_\nu)^2 \quad 4.3$$

Hence, fs TPLIF returns an easy way to extract the temperature simply from the inverse square of the fluorescence signal (provided the excitation laser intensity is held fixed). This method has been applied to the Kr TPLIF line images recorded with the fs-laser for Bunsen flame. The conversion to the absolute temperature was performed using a calibration point where the hot area of the flame is assumed to be at the adiabatic temperature of 2200 K.

From a double iterative procedure including the corrections for $T^{-0.5}$ and $g(\Delta\bar{\nu})$, the temperature profile was determined from the Kr TPLIF, calibrated using the hot temperature of

2200K. Figure 4.2 (left side) shows the comparison between the experimental and the simulated temperature profiles obtained in Bunsen burner using fs Kr-TPLIF and the corresponding profiles from ns experiments are shown in the right side.

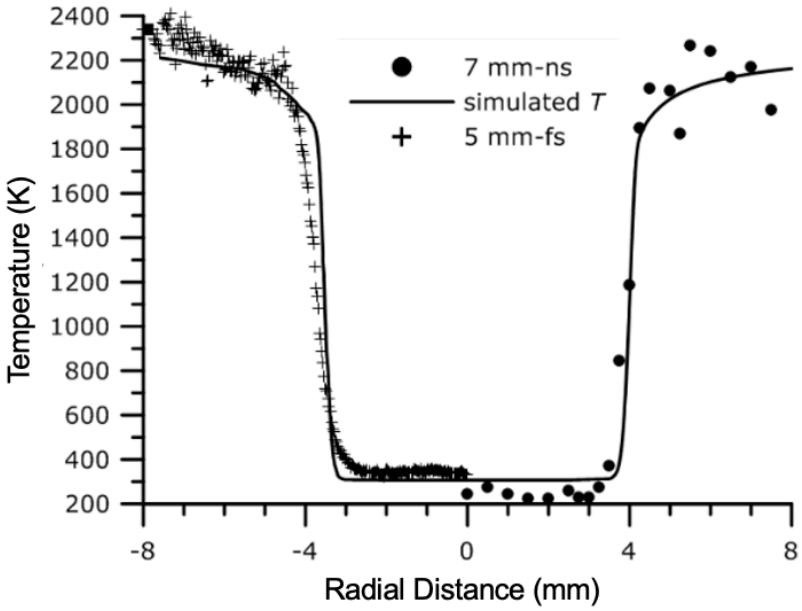

Figure 4.2 Comparison between the simulated and experimental T profiles determined from the Kr-LIF signal measured with a fs-laser at 5 mm (left) or with a ns-laser at 7 mm (right) for one atmospheric flame reprinted with permission from [128].

4.3 Bunsen Flame Measurements

4.3.1 Excitation and Detection Signal Analysis

Shown in Figure 4.3 is the dependence of Kr-atom fluorescence emission on the excitation wavelength at an atmospheric pressure recorded in a Bunsen flame. An intensifier gate width of 100 ns with 100% gain was used. Fifty shots are accumulated on the imaging system, and a set of 50 such images were recorded at each wavelength. The excitation wavelength reading was made

using a fiber-coupled spectrometer (Ocean Optics, Model: Flame S). It shows on-resonance wavelength near 204-nm, as expected, and has spectral bandwidth of ~0.5-nm. The corresponding spectra recorded for the excitation wavelength used are shown in Figure 4.4 along with the filter transmission curve indicated in blue. The significant Kr peaks are observed at 760.15, 785.48, 811.29, and 826.32-nm.

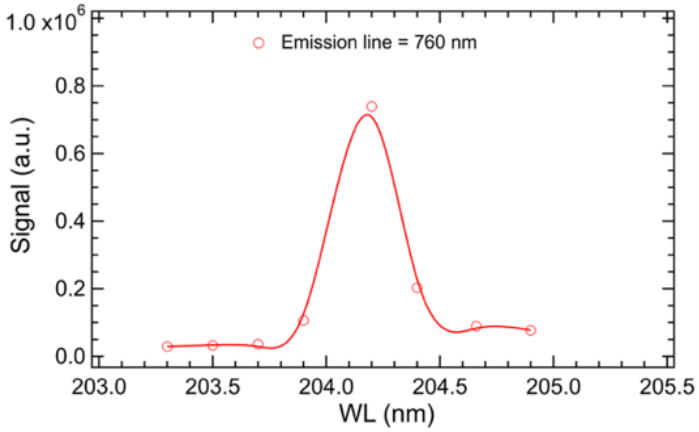

Figure 4.3 Fs Kr TPLIF signal dependent on the excitation wavelength recorded in gas cell at 1 bar.

Figure 4.5 shows no apparent deviation from quadratic dependence of the Kr fluorescence signal with respect to the laser energy, which is expected for the two-photon process. The symbols are experimental measurements, and the solid lines are quadratic power law fits. Each data point is accumulation of 50 laser shots and an average of 50 camera frames. The observed quadratic dependence also suggests that the photoionization and ASE are negligible in the investigated flames, which would have resulted in sub-quadratic laser energy dependence. Therefore, the laser energy was held constant at 3.5 μJ/pulse for the remainder of the experiment.

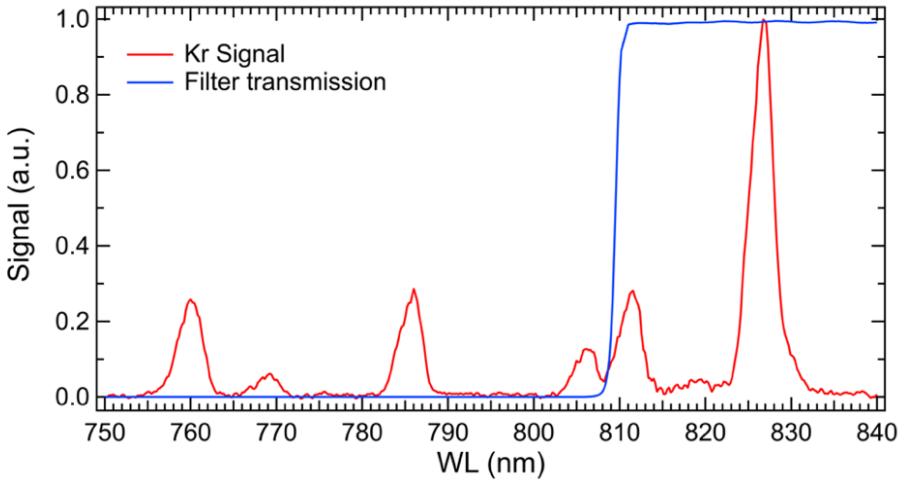

Figure 4.4 Experimentally recorded fs-TPLIF emission spectra of Kr at 1 bar along with filter transmission curve indicated in blue.

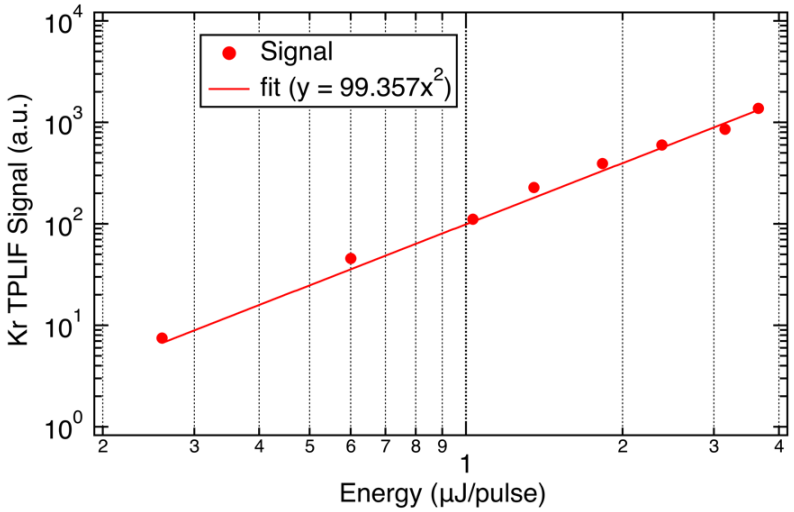

Figure 4.5 Fs Kr TPLIF signal dependence as a function of laser pulse energy at 1 bar.

4.3.2 Kr TPLIF Measurements

Similarly, Kr TPLIF measurements were performed along the radial axis at three HAB locations using the fs-laser at TAMU. The raw fluorescence images recorded by seeding 5% Kr into the Bunsen flame are shown in Figure 4.6. The typical width of the line filled about 8 pixels in the camera plane, corresponding to a spatially calibrated beam waist of 0.220 mm. The typical signal-to-background ratio in the inner premixed reactants zone is approx. 36, and that in the hot flame zone is 18. Those values changed to 8 and 5, respectively, when the Kr seeding level was changed to 1%. However, the general profile shapes remained unchanged. The signal-to-noise ratio (SNR) values defined as the mean signal of background subtracted image divided by one standard deviation of background noise are approximately 380 and 70 for 5% and 1% seeding levels, respectively.

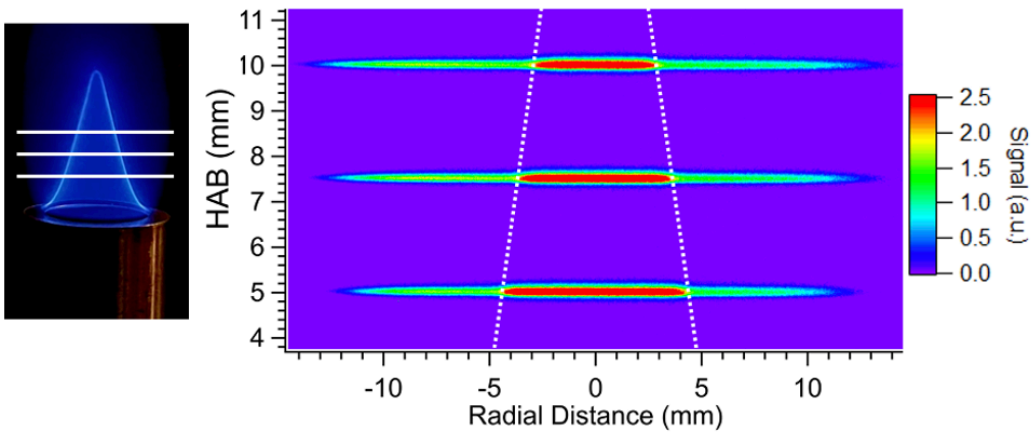

Figure 4.6 Fs Kr TPLIF line images recorded at three different HAB locations as indicated in $CH_4/O_2/N_2$/Kr Bunsen flame at 1 bar reprinted with permission from [128].

4.3.3 Temperature Extraction using Kr TPLIF

Figure 4.7 shows the corresponding LIF signals obtained by vertically integrating the line images shown in Figure 4.6. Only the right half of the nearly-perfectly symmetric line profiles are shown. The relative signals are normalized to the values of 5 mm < r < 8 mm region. The fs TPLIF returns an easy way to extract the temperature simply from the inverse square of the fluorescence signal (provided the excitation laser intensity is held fixed). The conversion to the absolute temperature was performed using a calibration point where the hot area of the flame is assumed to be at the adiabatic temperature of 2200 K. Accordingly, the radial TPLIF signals profiles shown in Figure 4.7 are converted to the corresponding *T* profiles using Eq. (4.3) and are shown in Figure 4.8. Again, for better clarity, only the right half of the nearly perfectly symmetric radial *T* profiles are shown. Beyond r =8 mm, S_{Kr} drops rapidly due to drop in flame *T* as well as X_{Kr} (due to mixing with outside air). Hence, *T* is difficult to quantify in that region.

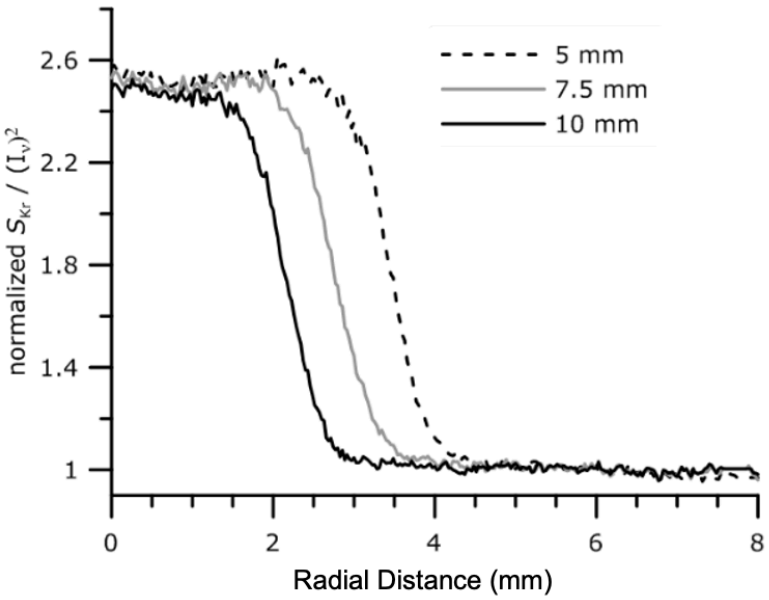

Figure 4.7 Normalized LIF signals along the radial axis measured at HAB = 5, 7.5, and 10 mm with a fs-laser at 1 bar reprinted with permission from [128].

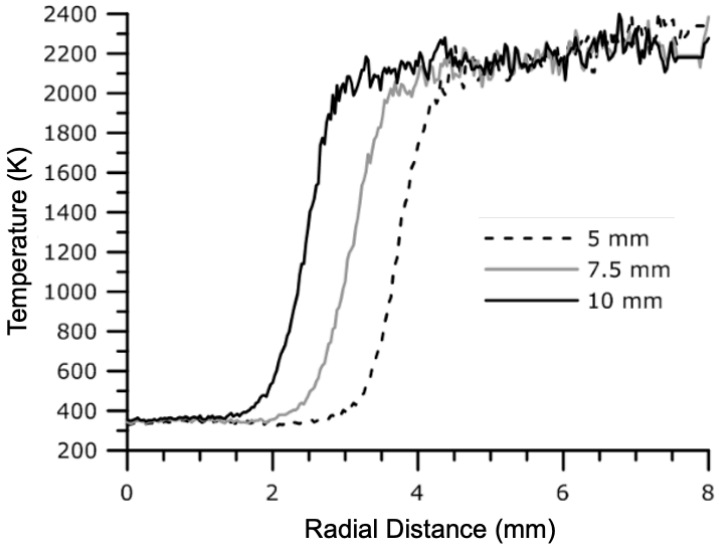

Figure 4.8 Radial T profiles obtained using fs-TPLIF at HAB = 5, 7.5, and 10 mm for 1 bar using the calibration procedure outlined in Eq. (4.3) reprinted with permission from [128].

4.4 High-Pressure Flame Measurements

The temperature measurement technique was extended in premixed CH_4/air flames surrounded by air co-flow particularly in high-pressure conditions up to 10 bar. Approximately 5% Kr is introduced into both premixed and co-flow regions as a tracer species. Figure 4.9 shows the high-pressure burner's schematic and the field of view for the detection system used. The details of burner construction and operation are explained in the previous Chapter. The flame has two distinct temperature zones – hotter and cooler zone due to burnt gases and unburnt air co-flow respectively. A home-built high-efficient FHG system was used to generate high-energy laser pulses near 204 nm that can overcome the laser transmission losses via thick optical windows. The absence of ASE was checked, and measurements were performed in the quadratic regime of LIF at 40 μJ/pulse laser energy (measured before the focusing lens and vessel window).

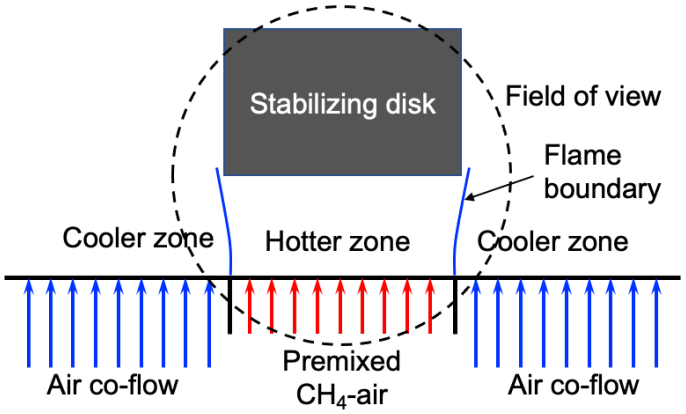

Figure 4.9 Schematic of the high-pressure burner for high-pressure Kr thermometry.

4.4.1 Kr TPLIF Measurements: Pressure and Equivalence Ratio Scan

The applicability of the fs TPLIF scheme in flames at elevated pressure was investigated via Kr TPLIF measurements as a function of pressure up to 10 bar in premixed CH_4/air flames at

ϕ = 0.9. The Kr TPLIF signal depicts a faster decay from P = 1 to P = 2 bar and slower decay after 2 bar till 10 bar as depicted by the closed circles in Figure 4.10. The solid line simply connects the data points at each pressure to guide the eye. The error bars are 2-sigma standard deviations of 50-line images recorded. It is observed that the signal is reduced by approximately 60% when the pressure is increased from 1 to 2 bar and then by only 30% when the pressure is increased from 2 bar to 10 bar. Such a slower decay of the Kr signal especially at a higher pressure and strong signal at 10 bar pressure gives us a firm belief that this fs diagnostics scheme can be extended to even higher pressure.

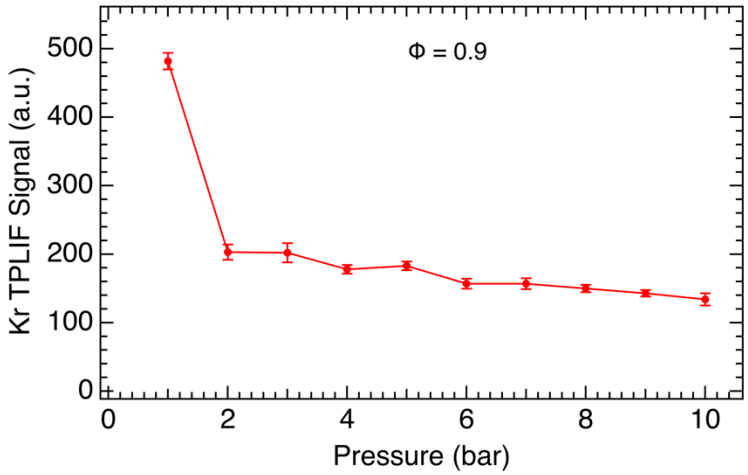

Figure 4.10 Pressure dependence of fs TPLIF signal of Kr, recorded in ϕ = 0.9 CH_4/air flames. Each data points corresponds to the spatially averaged Kr TPLIF signal integrated over the entire line image across the flame at HAB = 6 mm.

The Kr TPLIF measurements were performed for a range of equivalence ratios up to 10 bar pressure. Figure 4.11 shows the raw fluorescence images recorded for the pressure of 2 bar

and 8 bar by seeding ~6% Kr into the flow region. The Kr fluorescence signal was measured along the radial axis at the 6-mm height location of the high-pressure flame. Only the left half of the nearly-perfectly symmetric line profiles are shown. It depicts a nearly flat low Kr signal within the premixed region where high temperature burnt gases are present. In contrast, the Kr signal increases towards the periphery of the flame and peaks when the room temperature is attained because of the air co-flow. Similar strong temperature dependence was also observed in atmospheric Bunsen flame. The typical FWHM of the Kr line is about 5 pixels in the camera plane, corresponding to a spatially calibrated beam waist of 0.230 mm.

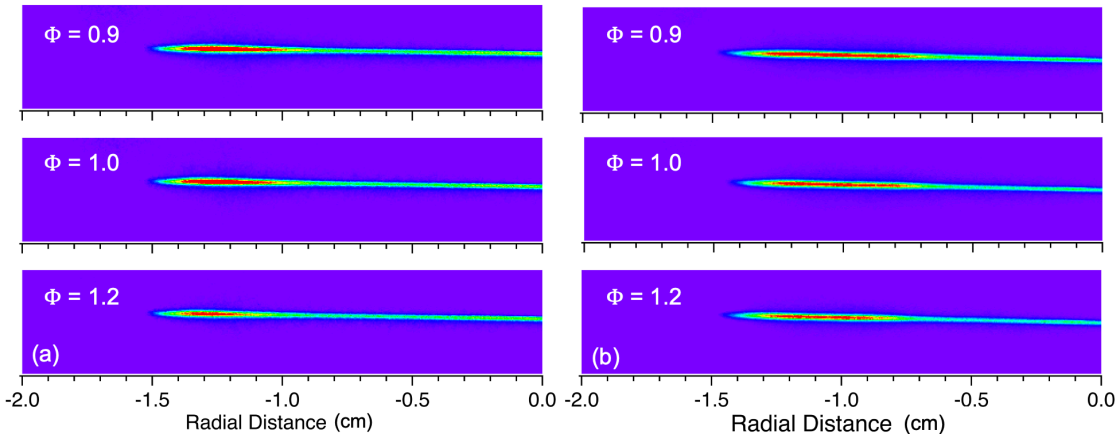

Figure 4.11 Fs Kr TPLIF line images recorded in CH_4/air flame at (a) 2 bar and (b) 8 bar.

Figure 4.12 shows the corresponding LIF signals obtained by vertically integrating the line images shown in Figure 4.11. The radial profiles are normalized by the peak Kr fluorescence signal obtained within the cool region outside the flame zone. In the case of ϕ =1.2 for both pressures, the secondary combustion region occurs near the periphery due to the reaction of extra fuel with the air co-flow. It is likely to cause a sharp rise in the Kr signal a little away from the flame axis due to the larger combustion zone. In the case of 8 bar pressure, the flow velocities of air and nitrogen co-flow are increased to stabilize the flame. Because of this increase in cold flow, the

flame zone is concentrated more towards the center and a wider cold region is achieved as depicted by the region of nearly flat high Kr signal from -0.9 cm to -1.2 cm. Importantly, Figure 4.12 depicts that the constant ratio of the Kr signal between cold and hot regions (~2.5) is preserved for all the cases irrespective of the flame and pressure condition. This ratio is converted to the T ratio using Eq (4.3).

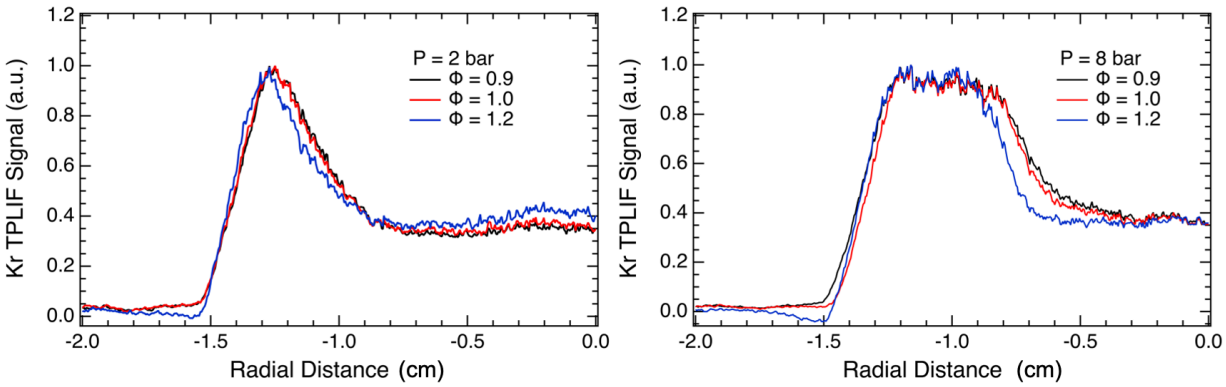

Figure 4.12 Normalized Kr TPLIF signals along the radial axis measured at HAB = 6 mm for pressure of 2 bar and 8 bar.

4.4.2 Temperature Extraction using Kr TPLIF

The fs TPLIF returns a simpler way to extract the temperature simply from the inverse square of the fluorescence signal. The conversion to the absolute temperature was performed using a calibration point where the cold region is assumed to be at the room temperature of 300 K. Accordingly, the radial Kr TPLIF profiles in Figure 4.12 are converted to corresponding T profiles and shown in Figure 4.13 and Figure 4.14 for pressure 2 bar and 8 bar respectively. It depicts that the high-temperature zone is present in the premixed section and the temperature gradually decreases to room temperature when the flow mixes with the air co-flow. The temperature in the 2 bar flames was also calculated using a well-documented, axisymmetric CFD code with detailed chemical kinetics, UNICORN, and is shown by a solid green curve in Figure 4.13. The

experimental T profile behavior is well predicted by the UNICORN model. The uncertainty of the temperature estimation is approx. 7.5 % (for the hot region) and 4.5 % (for the cold region), given by one standard deviation of the temperature values in the respective zone.

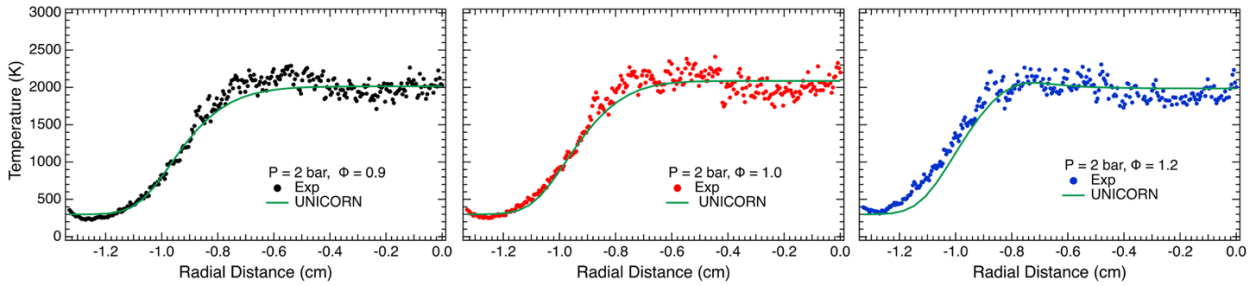

Figure 4.13 Radial T profiles obtained using fs-TPLIF for ϕ =0.9, 1.0 and 1.2 at 2 bar. The experimental T profiles are compared with the T obtained from the UNICORN model.

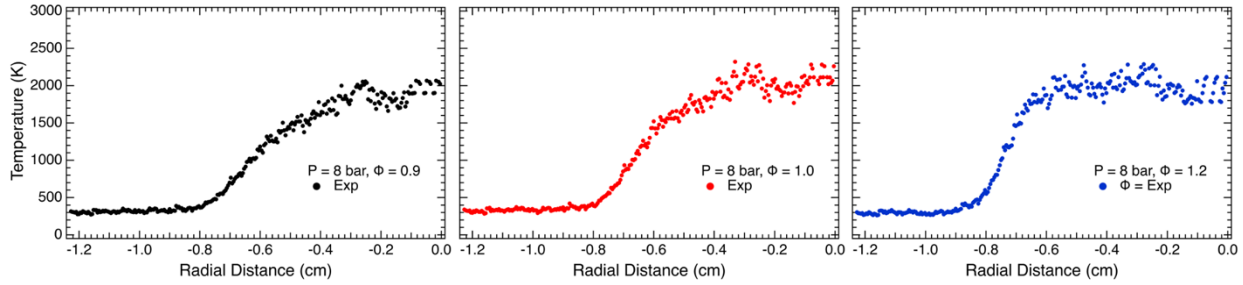

Figure 4.14 Radial T profiles obtained using fs-TPLIF for ϕ =0.9, 1.0 and 1.2 at 8 bar.

4.5 Summary and Recommendations

In contrast, converting the fs TPLIF signal into a T profile requires only the knowledge of the quenching rate, which can be approximated by$T^{-0.5}$ dependence in our flames. Hence, fs TPLIF provides a simpler way to extract the flame temperature, simply by taking the inverse square of the fluorescence signal. Accordingly, fs-TPLIF line images were recorded at for atmospheric

Bunsen flame and high-pressure flat flame and converted to radial T profiles. It was confirmed these T profiles agree well with 1D flame model predictions and the 2D UNICORN model predictions. Therefore, fs-TPLIF is a promising approach for thermometry in atmospheric and higher-pressure flames.

5. SIMULTANEOUS HYDROGEN ATOM IMAGING AND KRYPTON THERMOMETRY

5.1 Experimental Procedure for Simultaneous Measurements

5.1.1 Experimental Apparatuses

All the experimental runs were conducted in $CH_4/O_2/N_2$ Bunsen flame established on a 13-mm inner diameter stainless-steel tube. Around 5% Kr tracer gas was introduced to the mixture gas line. The gas mixtures were supplied with a volumetric flow rate of 0.775, 1.55, 5.3 & 0.358 slpm to maintain a cone height of nearly 17 mm. Bunsen flame was preferred because the conical shape of the premixed Bunsen flame provides steep species and temperature gradients and the temperature at the flame front and the reaction zone can be assumed adiabatic which is essential for thermometry purposes.

Figure 5.1 depicts the schematic of the experimental apparatus consisting of a frequency-tunable, regeneratively amplified Ti: Sapphire laser system generating fundamental output between 770–830-nm range with approx. 80-fs-duration laser pulses at 1-kHz-repetition rate. The 800-nm laser beam with input energy ~6 mJ/pulse pumps the OPA system to generate UV radiation at a 204.5-nm wavelength and is focused into the probe region using a +500-mm focal length lens (L_1). The H & Kr TPLIF signals were collected orthogonal to the direction of the propagation of the laser beam for spectroscopic studies and imaging measurements using two different detection systems.

The emission spectra were collected using a spectrometer (Princeton Instruments, Model: Isoplane 160) fitted with an ICCD camera (Princeton Instruments, Model: PIMax4). The combined spectrometer-camera system can provide a spectral resolution of approximately 0.20 nm/pixel for 300 lines/mm grating. The spectrometer-camera system was calibrated for wavelength using a dual

Hg/Ne-Ar calibration lamp (Princeton Instruments, Model: IntelliCal). The spectrometer was positioned such that the entrance slit, and the laser line were in the same horizontal plane. The horizontal entrance slit was wide open ~400 µm to maximize the H & Kr fluorescence signal collection efficiency. An additional +60-mm focal length plano-convex lens (L_2) was added in between the probe region and the detection system to optimize the signal collection solid angle and focus the flame emission into the entrance slit.

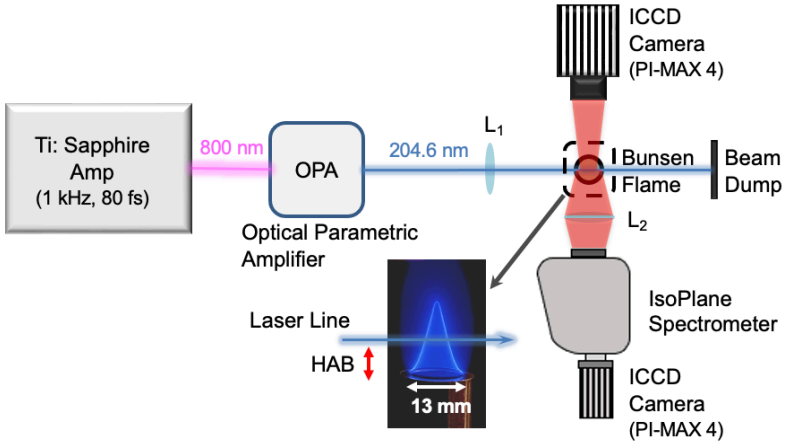

Figure 5.1 Schematic of the simultaneous H & Kr TPLIF experimental apparatus. L_1-Focusing lens, L_2-Detection lens, OPA-optical parametric amplifier.

5.1.2 Data Acquisition Settings

The fs H & Kr TPLIF imaging measurements were performed using the same ICCD camera setup alone. The ICCD camera was fitted with a 50-mm focal length Nikon visible camera lens (f/1.2) with an appropriate filter to isolate the desired fluorescence signals from unwanted interference and laser scattering. A summary of the parameters for the optical setup to conduct H & Kr imaging is listed in Table 5.1. The intensifier gate width was opened for 20 ns to suppress the collection of background light. In a typical experiment, 400 laser shots were accumulated on

the camera, and 50 such images were averaged and recorded at three different height locations. The laser beam energy was kept constant at 3.5±0.05 μJ/pulse to avoid ionization and ASE.

Table 5.1 Parameters for the optical setup.

Parameters	**Species**	
	Kr	**H**
Excitation λ (nm)	204.5	
Emission λ (nm)	826.5	656
Laser energy (μJ/ pulse)	3.5±0.05	
Camera	PI-Max4	
Camera lens	Nikon visible camera lens, f/1.2 (focal length = 50 mm)	
Pixel resolution	1024 × 1024	
Spatial resolution	35 pixels/mm	
Filter	Semrock, Part no. #FF01-832/37-50	Semrock, Part no. #FF01-650/60-50
Gate width (ns)	20	
On-CCD accumulation	400	
Exposure per frame	50	
Gain	100%	

In all measurements, a background image was captured separately with the laser beam blocked and then subtracted from each signal image during data analysis. Each background-subtracted image was corrected for variation in laser intensity along the laser line direction. The FWHM of the line images recorded was about 8 pixels in the camera plane which corresponds to a spatially calibrated beam waist of nearly 0.220 mm.

5.2 Methodology

5.2.1 Process Flow Diagram for Simultaneous Measurements

In this section, we present the methodologies involved for fs-TPLIF H and Kr signal acquisition and data processing. Figure 5.2 shows the flow chart of the procedure involved. In direct imaging measurements, the laser beam profile was characterized first and profile correcting map was obtained. The H and Kr signal images and background images were recorded simultaneously at three different heights (HAB = 5.0, 7.5 & 10 mm) using appropriate filters. Each experimental data points accumulated the fluorescence signal of 400 laser shots and 50 such frames were averaged. The gain was set at 100% and the gate width was opened to 20 ns. The signal images were corrected for chemiluminescence interference by subtracting off the background images recorded with the laser beam blocked. After background subtraction, the raw image was divided by the laser beam profile to obtain the required final image.

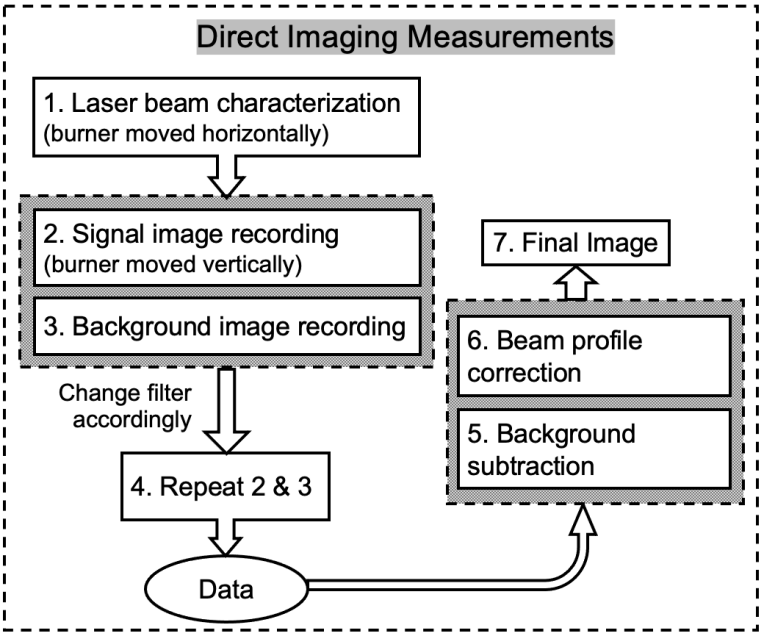

Figure 5.2 Flow chart showing the methodologies used for data acquisition and processing.

5.2.1 Laser Beam Profile Characterization

The laser beam profile needs to be characterized, especially since the Kr TPLIF response depends on the laser energy squared and as a result, spatial non-uniformity significantly influences the fluorescence distribution. For the laser beam profile correction map, the Kr TPLIF signal was recorded for the cold flow (a mixture of O_2, N_2 and Kr) flowing through the burner tube. The burner was moved along the laser path, around 1 mm in each step and around 60 TPLIF signal and background images were captured. All these images were averaged together after background subtraction to obtain the laser intensity correcting map, as shown in Figure 5.3. It shows that the laser intensity is non-uniform and is focused slightly on the left side of the region of interest. This correction map is important to obtain the symmetric H and Kr line profiles. A detailed description of obtaining laser sheet profile is provided in Appendix 10.2.

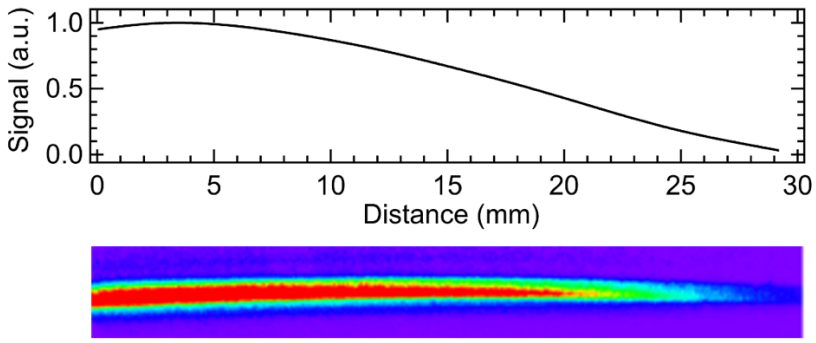

Figure 5.3 Laser beam profile correcting map.

5.3 Results and Discussion

5.3.1 Simultaneous Excitation Spectrum

Previous studies have shown Kr is excited from the 4p ground state to the 5p' excited state via two-photon absorption near 204-nm. Fluorescence signals are collected at 826.5-nm from the 5p' to 5s' decay [67]. Similarly, the two-photon excitation of $n = 1 \rightarrow\rightarrow n = 3$ transition of H-atom occurs near 205 nm with subsequent fluorescence yield from $n = 3 \rightarrow n = 2$ decay at 656 nm [43, 45]. Hence, both these species can be excited simultaneously at an intermediary wavelength near 204.5 nm taking advantage of broadband fs pulses having linewidths in excess of 400 cm^{-1}. The on-resonance laser spectra for the two species used for this experiment show significant overlap (as indicated in Figure 5.4) because of the broad full-width at half-maximum (FWHM $\sim$ 1.5 nm) indicating possible simultaneous excitation of both species.

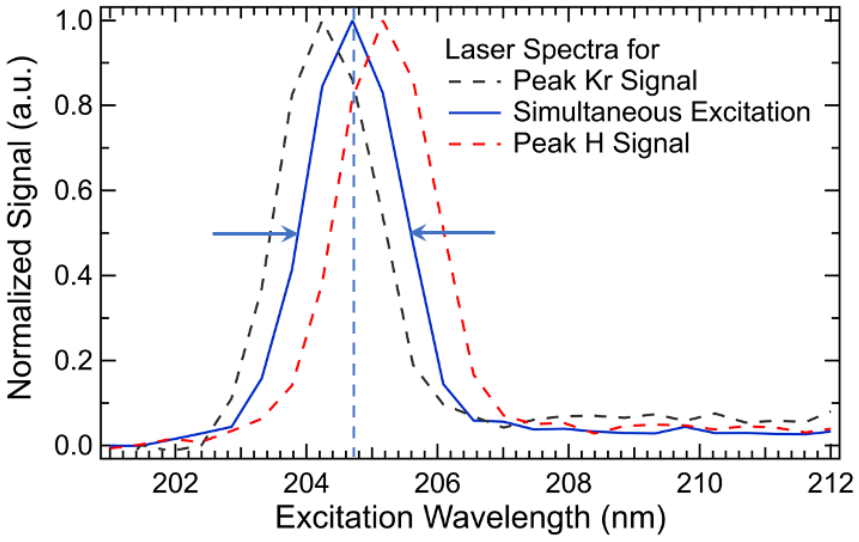

Figure 5.4 Spectral overlap of the laser spectra for the simultaneous excitation of two species.

5.3.2 Simultaneous Spectroscopic Studies of Kr and H

Simultaneous H and Kr emission spectra were recorded at an intermediate wavelength of 204.5-nm. We verified the H and Kr emission line positions in the 640–840 nm range through a spectrally resolved fluorescence signal in the flame using the combination of the spectrometer-camera system. The spectra were recorded using a 300-lines/mm grating with a 300-nm-blaze wavelength. The low-resolution grating yielded a wavelength bandwidth of approximately 200 nm at one time; hence the central wavelength was set at 740-nm to capture both species at once. Figure 5.5 presents the simultaneous H & Kr fs-TPLIF spectra recorded for 13-mm $CH_4/O_2/N_2$/Kr jet flame in $\Phi = 1.0$ flame. The H-atom peak occurs at 656-nm, as indicated in Figure 5.5. The main Kr emission lines are at 760, 785, 810, 811, and 826 nm, which were also confirmed using a cold flow of Kr at 1 atm. Although the spectrometer can provide a spectral resolution of approximately

0.20 nm/pixel, all H & Kr emission peaks obtained here are artificially broadened as the slit was widely opened to increase the signal collection efficiency.

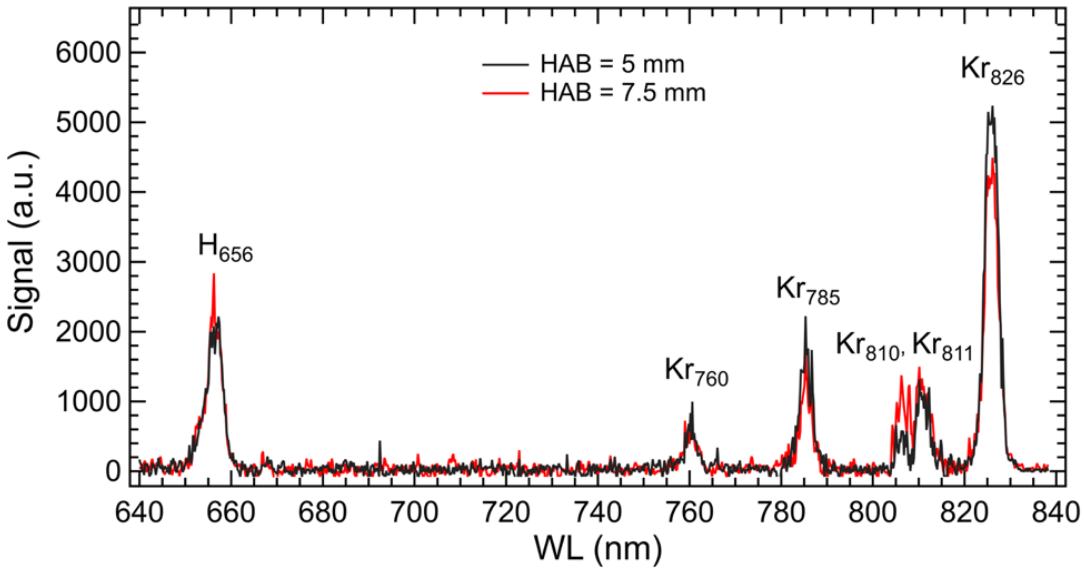

Figure 5.5 Simultaneous Kr fs-TPLIF and H fs-TPLIF spectra recorded for $CH_4/O_2/N_2/Kr$ jet flame at Φ=1.0.

5.3.3 Combined H & Kr Imaging Measurements

The H & Kr fs-TPLIF imaging measurements were performed along the radial axis at three HAB locations as shown by stacked TPLIF images in Figure 5.6, along with the flame image in the center. Figure 5.6a depicts H TPLIF images where H-atom peaked sharply close to the flame front and in the reaction zone where most of the combustion activities take place. The flat zero signal indicating a non-reacting zone is followed by a sharp H peak at the cone edge which decays gradually further away. The general profile trend remains similar for all three HAB locations. The average SNR value is approximately 105 for the H TPLIF image. The white dotted white lines are drawn to indicate the conical shape of the flame front, as evident by the very faint

chemiluminescence signal in flame image. In contrast, Figure 5.6b depicts that Kr distribution profiles appear comparatively different, which show strong temperature dependence. As Kr species is excited to the upper excited level (5p'), additional transitions occur due to redistribution from the excited level to the other levels depending on the temperature, colliders, and pressure which causes the Kr emission to become maximum at the low-temperature zone. The signal decays quickly near the flame front where a rapid increase in temperature takes place and remains constant in the reaction zone due to the constant temperature zone. The average SNR values are approximately 95 and 52 for the cold and hot regions of the Kr image, respectively. The interference due to the fundamental laser wavelength at 820 nm was removed through the background subtraction during data processing. Hence, we can claim that no other interferences were present in the filtered range used. Thus, the Kr emission signal collected for the current setup was primarily from the 826-nm emission line as there is a sharp cut-off of the filter transmission efficiency curve beyond this wavelength range.

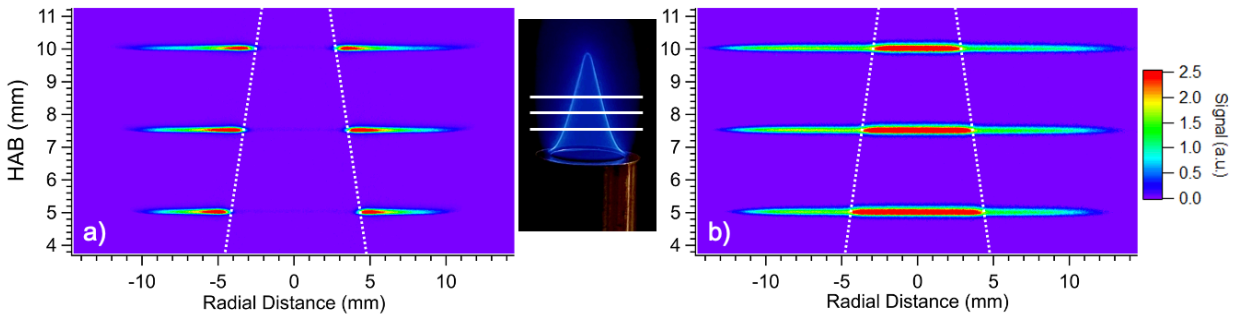

Figure 5.6 a) H and b) Kr fs-TPLIF line images recorded for $CH_4/O_2/N_2$/Kr jet flame at Φ=1.0 at HAB=5 mm, 7.5 mm & 10 mm as indicated by white lines in the central flame image.

5.3.4 *In-situ* Temperature Measurements

The Kr line images in Figure 5.6b are vertically integrated and the corresponding LIF signals are depicted by black dots in Figure 5.7. Due to the symmetric nature of the line profiles, only the right half is shown here. In a recent publication, we demonstrated that the in-situ 1D temperature profile could be extracted easily using the inverse square of the Kr fluorescence signal provided the excitation laser intensity is held constant [128]. The adiabatic temperature of the hot region was assumed to be 2135 K and the corresponding radial temperature profiles were generated by using Eq. 4.3 in Chapter 4 and are shown by the red dots in Figure 5.7. Only $0.0 < r\ (mm) < 8.0$ portion is shown here, beyond which temperature is expected to drop rapidly because of the diminishing reaction zone and rapid mixing with outside cold air in the outer shear layer. The uncertainty of the temperature estimation is approx. 5.0 % (for the hot region) and 3.5 % (for the cold region), given by one standard deviation of the temperature values in the respective zone. The region considered was $5.0 < r\ (mm) < 8.0$ for the hot region and $-1.5 < r\ (mm) < 1.5$ for the cold region. Similar calculations were performed for three different heights and were averaged to obtain the overall uncertainty.

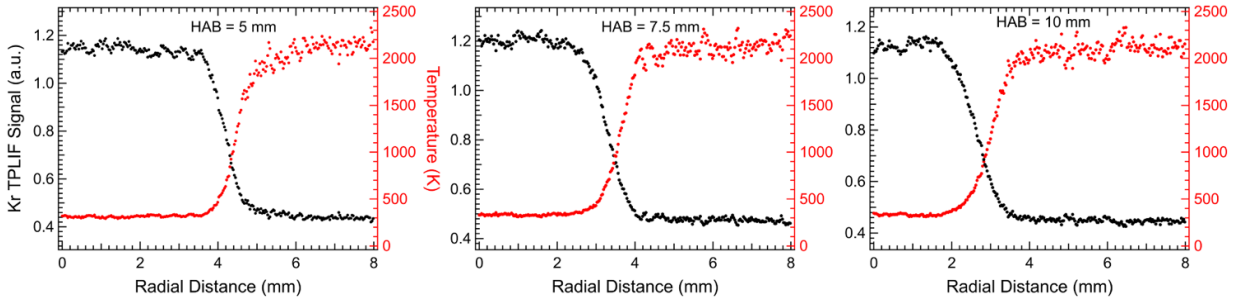

Figure 5.7 Fs Kr TPLIF signals and corresponding temperature profiles along the radial axis obtained at HAB=5, 7.5, and 10 mm.

5.3.5 Spatially Resolved H-atom Distribution using Kr Calibration

5.3.5.1 Detailed Calibration Procedure

In addition to the *in-situ* temperature profiles measurement, the same Kr profile is used as a calibration source for the spatially resolved H-atom concentration measurement which is the main advantage of this study. The calibration procedure involves the comparison of the H TPLIF, and Kr TPLIF signals recorded with a known mole fraction of Krypton (χ_{Kr}). Provided that the quadratic regime of fluorescence holds, the H-atom number density can be calculated using the following equation [20, 67, 129, 130].

$$\chi_H = \chi_{Kr} \frac{C_{Kr}}{C_H} \frac{\sigma_{Kr}^{\langle 2 \rangle}}{\sigma_H^{\langle 2 \rangle}} \frac{g(\Delta\bar{\nu}_{Kr})}{g(\Delta\bar{\nu}_H)} \frac{A_{32,Kr}}{A_{32,H}} \frac{A_{3,H}+Q_H}{A_{3,Kr}+Q_{Kr}} \frac{f_B(Kr,T)}{f_B(H,T)} \frac{S_H}{S_{Kr}} \frac{I_{\nu_{Kr}}^2}{I_{\nu_H}^2} \left(\frac{\nu_H}{\nu_{Kr}}\right)^2 \quad 5.1$$

Considering i refers to a species, C_i is the global efficiency of the LIF collection at a specific wavelength (Camera efficiency, filter efficiency, lenses, solid angle, etc.). The determination of the normalized line profile of the two-photon excitation, $g(\Delta\bar{\nu}_i)$ is generally imprecise [20]. In this study, it is considered unity because of the considerably broad bandwidth of the fs laser pulses used, although the linewidths of the two resonances are quite different. In some studies, the fluorescence signal was spectrally integrated by scanning the laser wavelength over the resonance of each species to account for the $g(\Delta\bar{\nu}_i)$ ratio. Table 5.2 lists the spectroscopic parameters like line shape-independent two-photon absorption cross-section ($\sigma_i^{\langle 2 \rangle}$), spontaneous emission rate of the excited level ($A_{3,i}$) and spontaneous emission rate along the detection transition ($A_{32,i}$) adopted for the H and Kr during the present work. The Boltzmann function f_B of each species in a singlet state S is independent of the temperature and is equal to 1. The fluorescence signal ratio $\left(\frac{S_H}{S_{Kr}}\right)$is obtained during the experiment. The laser energy and the excitation wavelength are kept constant during the experiment and hence I_{ν_i} and ν_i are unity.

Table 5.2 Spectroscopic constants required for calibration procedure.

Parameters	Species	
	H	**Kr**
$\frac{\sigma_{Kr}^{\langle 2 \rangle}}{\sigma_{H}^{\langle 2 \rangle}}$	0.62 ± 50% [67]	
A_{32} $(10^6\ s^{-1})$	57.8 [131]	34.16 [132]
A_3 $(10^6\ s^{-1})$	57.8 [131]	35.0 [132]

The flame studied for this study and Ref [20] is same, so the spatially resolved quenching rate profile of the Kr atom was taken from supplementary material of the literature [20]. Similarly, the quenching rate of the H atom is calculated using

$$Q_H = N_t \sum_i \chi_i \, k_i \qquad 5.2$$

Where N_t is the total number density, χ_i is the collider mole fraction and $k_i$is the quenching rate coefficients. The quenching coefficients of the main colliders of interest in the flames are provided in the literature [124]. We calculated Q_H in the current Bunsen flame using the rate coefficients for CH_4, O_2, N_2, H_2O, CO_2, and C_2H_2 at room temperature and assuming that the coefficients are temperature independent [124]. The spatial distribution of the temperature profile was taken from the current experiment and the spatial distribution of the mole fractions of these collider species were obtained from simulation data.

5.3.5.2 ANSYS Fluent modeling

The simulations were carried out in a commercial computational fluid dynamics (CFD) solver: ANSYS Fluent. The solver used was a 2D axisymmetric solver allowing the simulations to be conducted only in half of the domain to limit computational expense. The domain extended to 80 mm on the horizontal axis and to 500 mm on the vertical axis. The turbulence model used was a k-epsilon standard model which is the most common model. The partially premixed combustion model was selected, and GRI-Mech 2.11 mechanism with 49 species and 279 reactions was imported to generate a premixed flamelet which is necessary to create a distinct conical feature in jet flame combustion. The inlet mass flow rate (used in the experiments) and outlet pressure boundary conditions were provided to the domain. In solution methods, a Semi-Implicit Method for Pressure-Linked Equations (SIMPLE) scheme was used as a pressure-velocity coupling scheme. Such a scheme is often preferred for steady-state problems as it results in faster convergence. A second-order upwind spatial discretization was chosen for all solvers (momentum, turbulence kinetic energy, progress variable, and energy) to increase the accuracy of the solution. A convergence criterion of 1×10^{-4} was set for each residual except for the continuity equation (1×10^{-7}) and energy equation (1×10^{-8}) for better convergence. The solution was initialized using a hybrid initialization and 2×10^{4} iterations were set for the residual to converge.

5.3.5.3 Quantitative Concentration of H-atom profiles

The 1D temperature distribution profiles and H fluorescence profiles are obtained along a line at once. The spatially resolved 1D temperature distribution profile is of great interest for in-situ quenching corrections of the H fluorescence signals. The simultaneous measurements of Kr fluorescence, temperature and H fluorescence are especially helpful to conduct a detailed

calibration scheme as done by Nathalie et al [20] for quantitative H atom measurements avoiding the need of additional calibration experiments. In addition to these measurements, a thorough understanding of the experimental quenching rates and concentrations of major colliders is essential to obtain quantitative H number densities. While such an extensive experimental investigation warrants a separate dedicated study, this manuscript presents a sample case for quenching corrections based on model prediction of collider species spatial distribution.

Figure 5.8a depicts the corresponding LIF signals obtained via vertical integration of the H line images in Figure 5.6a. Figure 5.8b shows a sample case for experimental H atom profile (black dots) compared with H atom concentration (green dots) at HAB = 5.0 mm. The general trend for H atom no. density profile is similar to the H TPLIF profile with approx. $\pm$15% residual signal. The peak H-atom signal varies within $\pm$10% obtained from the repeated experiment. Only 0.0 < r (mm) < 8.0 portion is shown here where experimental temperature profile is valid. The peak H no. density found during the experiment is on the order of $10^{17}(\#/\mathrm{cm}^3)$.

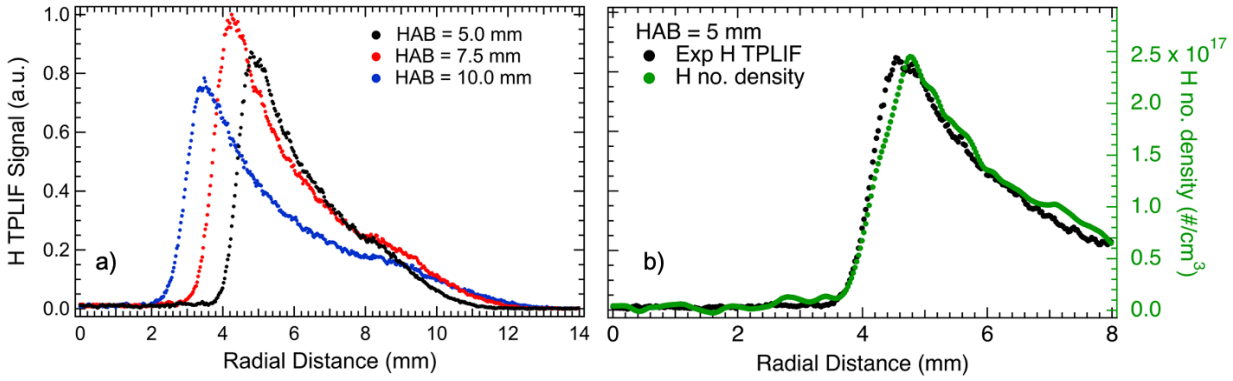

Figure 5.8 a) Fs H TPLIF raw signals along the radial axis obtained at HAB = 5, 7.5, and 10-mm. b) a sample case for quenching applied H atom profile at HAB = 5.0 mm.

5.3.6 Signal Enhancement Strategies

It is worthwhile to mention that only 3.5 μJ/pulse of 204.5 nm laser radiation generated from OPA is introduced into the probe region. In the future, a modified harmonic generation system with increased pump beam spot size is needed to utilize the maximum available pump energy of ~6 mJ/pulse. A simple power scaling suggests approximately ~20× the laser energy used for the current experiment is achievable. Such improvements can result in a substantial increase in the signal counts approx. ~400× (owing to two-photon excitation) for both the species, thereby enabling kHz-rate and simultaneous single-shot H & Kr imaging in future applications. Such simultaneous measurements and its application for H atom concentration measurements especially in the elevated pressure condition will be the part of our future investigation.

5.4 Summary and Recommendations

In this study, the Kr TPLIF technique was applied to measure the in-situ temperature profile in a $CH_4/O_2/N_2$ Bunsen flame and quantify H-atom fluorescence signal. The two species – H and Kr were excited simultaneously at an intermediate wavelength near 204.5-nm taking an advantage of broadband, fs pulses having linewidths in excess of 400 cm^{-1}. The simultaneous excitation was performed using two-photon absorption at 3.5 μJ/pulse laser energy where both the species show quadratic laser energy dependence. Individual H and Kr TPLIF signals were collected at three different height locations in the $CH_4/O_2/N_2$/Kr Bunsen flame. Recently demonstrated Kr thermometry technique was used to extract 1D temperature profiles from the Kr TPLIF images by simply squaring the inverse of the signal counts and providing adiabatic temperature estimation. Hence, the temperature distribution, H and Kr atom fluorescence profiles are acquired along a line simultaneously using a single laser pulse. Thus, obtained in-situ 1D temperature profile was used

to calculate the quenching rates which along with the Kr fluorescence signal were applied for the calibration of H atom and the peak H no. density was found to be on the order of $10^{17}(\#/\mathrm{cm}^3)$. Overall, the TPLIF technique using broadband fs pulse, combined with efficient harmonic generation system has huge prospects for kHz-rate, simultaneous single-shot H and Kr imaging, and subsequent quantitative H atom measurements in future applications.

6. FEMTOSECOND CH PLANAR LASER-INDUCED FLUORESCENCE DIAGNOSTICS

6.1 Experimental Details and Procedure

6.1.1 Burner Configuration and Flame Conditions

The fs CH PLIF measurements were performed in premixed laminar and non-premixed turbulent flame at different conditions stabilized on the Bunsen burner with an inner diameter of ~4 mm as shown in Figure 6.1. The red dotted squares (~14 mm × 14 mm) represent the region from where the CH PLIF signal was captured. For the stable laminar flame, CH_4, O_2, and N_2 were set to produce a conical flame with cone height ~16 mm at Φ=1.30 and the flow rates used were 0.50 slpm, 0.769 slpm, and 2.30 slpm respectively. In the case of non-premixed flame at low flow velocity, diffusion flame appears laminar near the jet exit and becomes turbulent further downstream [133]. As the flow velocity is increased, the flame becomes turbulent throughout and is detached from the burner surface. It is important to add H_2 with the inlet mixture (C_2H_4 and N_2 in this study) to prevent such lift-off. H_2 burns with a high burning velocity as compared to hydrocarbon flame, so an appropriate amount of H_2 has a strong influence on the overall burning velocity of the inlet mixture preventing it from lifting off. The flow rates used were 5 slpm, 21 slpm, and 8 slpm respectively for C_2H_4, N_2, and H_2. All the experiments were conducted under atmospheric pressure conditions.

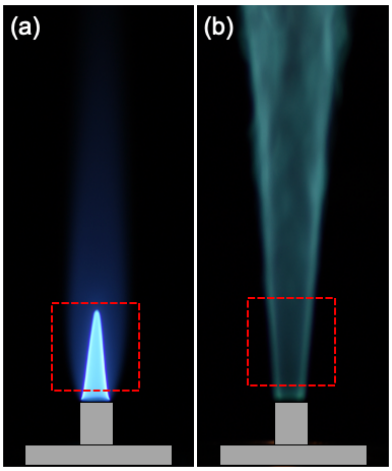

Figure 6.1 Photographs of the investigated flames (a) $CH_4/O_2/N_2$ premixed laminar flame with no co-flow, and (b) $C_2H_4/H_2/N_2$ non-premixed turbulent flame with air co-flow.

6.1.2 Fs Laser System for CH PLIF Measurements

The experimental apparatus consists of a fs laser system, burner configuration, and detection system as shown schematically in Figure 6.2. A regeneratively amplified Ti: Sapphire laser system (Spectra-Physics, Model: Solstice Ace) generates fundamental output between 770–830 nm range with 6 mJ/pulse laser energy and approximately 80-fs-duration laser pulses at a 1-kHz-repetition rate. As shown in Figure 6.2, the 780 nm laser beam with energy turned down to ~2 mJ/pulse pumps a high-conversion efficient SHG system to generate radiation near 390 nm for CH B–X excitation. The 10 mm diameter fundamental beam was down collimated to ~7 mm using a telescopic combination of +200 mm and -90 mm lens. This reduced diameter beam was guided through several 780 nm mirrors and then into the SHG BBO crystal to produce a 390 nm beam. The frequency-doubled beam was then focused onto the flame using a combination of plano-convex lens and cylindrical lens to create a beam sheet of the height approximately ~14 mm.

6.1.3 Imaging Apparatus for CH PLIF Measurements

The CH PLIF emission signal from the flame was collected orthogonal to the direction of the propagation of the laser beam sheet using two camera configurations: (i) a shot-averaged signal in the laminar flame using an ICCD camera and (ii) a single-laser-shot CH PLIF imaging in the laminar and turbulent flame using a high-speed CMOS camera (Photron, SA-Z) coupled with a high-speed intensified relay optics (HS-IRO) unit (LaVision, HS-IRO). Each detection system was fitted with a 50 mm focal length visible camera lens (Nikon, $f/1.2$) with a narrow bandpass filter centered at 434 nm (Semrock, FF01-434/17-50) to block unwanted interferences and laser scattering.

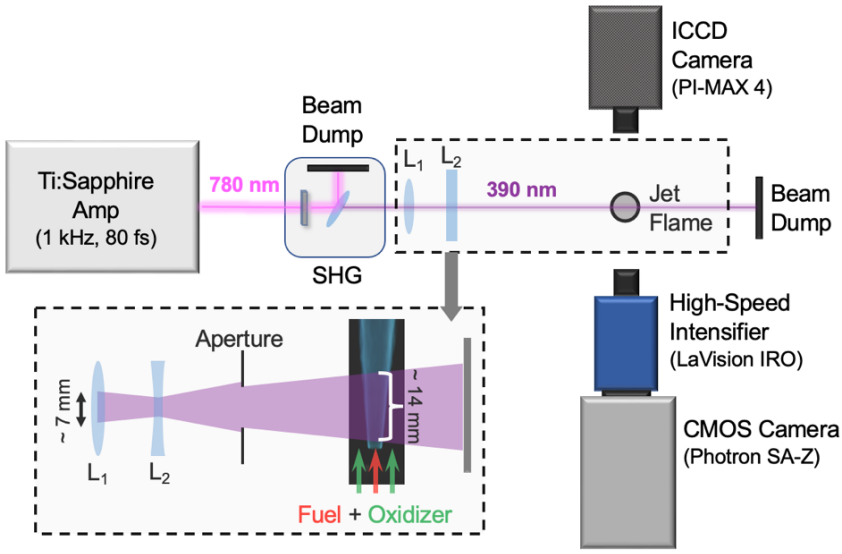

Figure 6.2 Schematic of the experimental apparatus showing laser and detection system along with the flame setup in the inset; SHG = second harmonic generation; ICCD = intensified charge-coupled device; L_1 = plano-convex lens; L_2 = cylindrical lens.

6.2 Results and Discussions

6.2.1 Excitation Scan

Figure 6.3 shows a simulated high-resolution excitation spectrum of CH B–X transition with Lorentzian lineshape, obtained using LIFBASE software (version 2.1.1) for a temperature of 2000 K. A broad Gaussian profile of the laser spectrum (black curve) with full-width-at-half-maximum (FWHM) ~2.5 nm is also included for comparison. The maximum intensity of the rotational excitation line under the laser curve is observed near 390 nm and considering the lines with intensity above 10% of the maximum, altogether 39 different rotational lines are excited at once by the broad fs laser pulse with approximately 160 cm^{-1} bandwidths. Such simultaneous excitation of the large no. of the transitions is important to generate CH PLIF with high SNR.

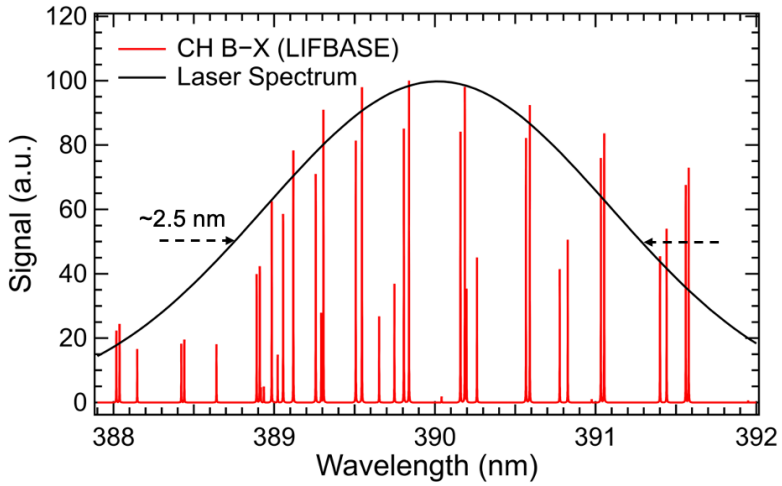

Figure 6.3 High resolution scan of several rotational lines (red lines) of the B–X transition excited by broad laser spectrum (black line) with FWHM ~2.5 nm.

The wavelength scan was conducted in $CH_4/O_2/N_2$ Bunsen flame at $\Phi = 1.30$ within 13 nm range at low laser energy (~8 μJ/pulse) to avoid any possible saturation and dissociation of other

CH precursors such as CH_3, CH_4 etc. A detailed investigation of the saturation effect due to higher laser energy was also performed and is presented in *Section 3.3*. Note that this scan was conducted using a laser line with a beam waist of ~180 µm, obtained from FWHM of line images. The experimental data points are the CH emission lines collected from the B–X (0,1), A–X (0,0), and (1,1) bands near 431 nm and are represented by black dots in Figure 6.4. The experiment was repeated multiple times near the peak wavelength region to confirm the repeatability of the excitation trend obtained. Also included is the simulated low-resolution excitation spectrum of CH B–X transition with Lorentzian lineshape, obtained using LIFBASE software. A good agreement is observed between the experiment and simulation with a peak excitation wavelength of 390 nm which was fixed for the rest of the experiment. Such a broad excitation spectrum of CH is particularly advantageous to avoid a weak absorption band of formaldehyde (HCHO), discussed further in *Section 6.2.5*.

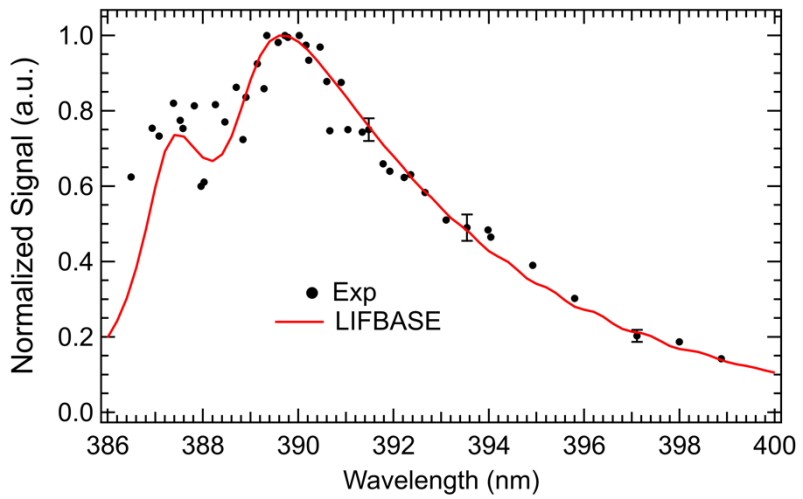

Figure 6.4 CH LIF signal response to the laser wavelength in $CH_4/O_2/N_2$ Bunsen flame at Φ = 1.30 fitted with a low resolution LIFBASE simulation.

6.2.2 Emission Spectrum

The CH LIF emission spectrum was captured in $CH_4/O_2/N_2$ Bunsen flame at $\Phi = 1.30$ to check the possible interference from laser scattering and other species. The 390 nm laser beam was focused into the probe region and the emission spectra were collected using a spectrometer (Princeton Instruments, Model: Isoplane 160) fitted with an ICCD camera. The spectrometer-camera system was calibrated for wavelength using a dual Hg/Ne-Ar calibration lamp (Princeton Instruments, Model: IntelliCal). The spectrometer was positioned such that the horizontal entrance slit, and the laser line lie in the same horizontal plane. The entrance slit was open to ~100 μm. An additional +60-mm focal length plano-convex lens was added in between the burner and the detection system to optimize the signal collection solid angle and focus the flame emission into the entrance slit.

Initially, the entire spectral range of interest was covered using 300 lines/mm grating and 300 nm Blaze wavelength with central wavelength kept constant at 400 nm. An average of 2500 laser shots was recorded for the spectrum and the elastic scattering from the excitation laser beam was observed at 390 nm, as shown in Figure 6.5. It is likely that the laser line could be blended with CH B–X (0,0) emission towards the right wings causing it to be little asymmetric. A weak CH emission at 430 nm due to B–X (0,1), A–X (0,0), and (1,1) bands were also observed. A high-resolution grating (1200 lines/mm) with 300 nm Blaze wavelength was used to record CH fluorescence in the narrow 50 nm range near 430 nm. The experimental spectra recorded are shown in the inset of Figure 6.5 and are denoted by black dots. It is clearly indicated that the location of the CH fluorescence spectra matched well with the simulation (red curve) using the LIFBASE package, although the intensity of the individual rotational lines varies likely due to temperature

change under those conditions. Additionally, the transmission curve of the filter (Semrock, Part No. FF01 434/17-50) with a peak transmission efficiency of ~95% used for CH imaging experiments is indicated by the blue curve. No fluorescence interferences from other combustion species in the spectral range of interest are observed in the flame investigated during the fs CH LIF scheme. Hence, by utilizing CH B–X excitation transition along with an appropriate filter, the elastically scattered laser light is sufficiently blocked which is the main advantage of this scheme as compared to CH A–X.

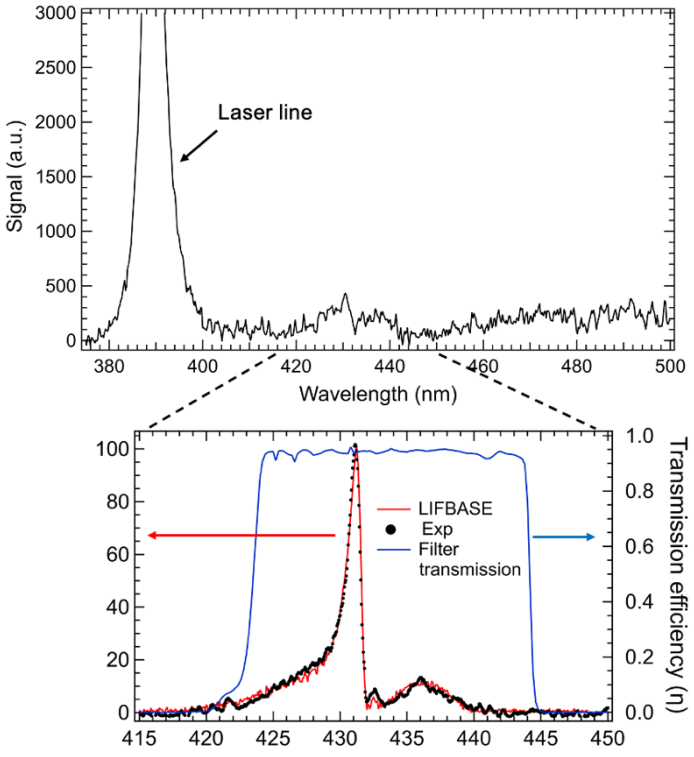

Figure 6.5 Emission spectra showing laser scattering along with CH fluorescence emission (black dots) fitted with LIFBASE simulation (red curve) in zoomed view. The blue curve represents the transmission curve of the filter used.

6.2.3 Laser Energy Dependence

The dependence of the CH fluorescence signal on the laser pulse energy was investigated by varying the pulse energy using a circular, continuously variable, reflective neutral density filter (Thorlabs, NDC-100C-4M) placed on the laser beam path. The laser was operated at the optimum excitation wavelength of 390 nm to maximize the fluorescence signal obtained. The laser beam was focused into a rich $CH_4/O_2/N_2$ flame at $\Phi = 1.30$ stabilized on the Bunsen burner, 5 mm above the burner exit. The laser pulse energy was measured with a laser power meter placed right after a 500 mm MgF_2 plano-convex lens (Thorlabs, Part No.# LA6009). The fluorescence signal was collected with an ICCD camera (PI-MAX4) coupled with a 50 mm visible lens (Nikon, $f/1.2$).

The laser energy dependence curve was obtained by plotting the averaged CH LIF signals versus the corresponding pulse energies as shown in Figure 6.6. Each data point (black dots) accumulates the fluorescence signal of 100 laser shots with 50 exposures per frame. The error bars represent one standard deviation calculated from 50 individual frames recorded for each data points. A function (black solid line) is fitted into these data points to obtain a simplified saturation equation [37, 76] given by:

$$I_{CH} = A \cdot \left(\frac{I_L}{I_L + I_{L,sat}}\right) \tag{6.1}$$

Where, I_{CH} is the CH LIF signal, A is a scaling factor, I_L is the laser pulse energy and $I_{L,sat}$ is the pulse energy required to achieve saturation of the CH signal. It was deduced from the fit that approximately 36 μJ/pulse is required to saturate the CH signal. Hence, high laser pulse energy can be utilized easily for the simultaneous excitation of several rotational lines to bring these transitions close to mild saturation resulting in high SNR for CH PLIF diagnosis.

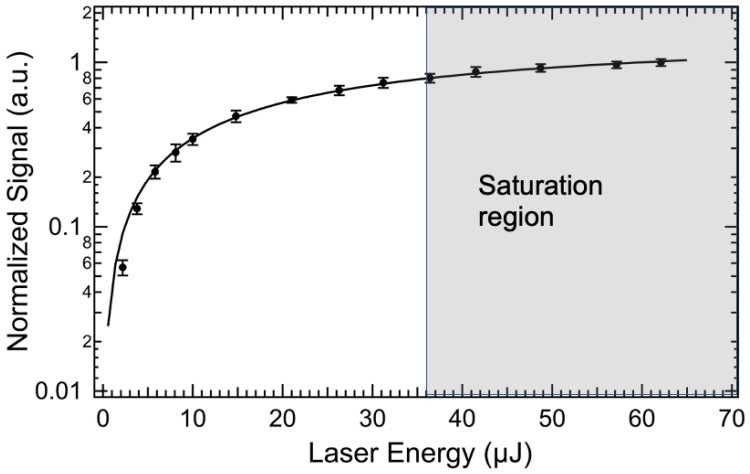

Figure 6.6 CH LIF signal as a function of laser pulse energy for $CH_4/O_2/N_2$ Bunsen flame at Φ = 1.30. A fit (solid black line) given by the saturation equation in the text is fitted to the experimental data (black dots).

6.2.4 Laminar Flame Investigation

The hydrodynamic flame surface instability acting on the flame front due to the density transition across the flame front is characterized by the flame thickness [134]. A decrease in the flame front thickness indicates the increase of such kind of instability. Figure 6.7 presents the experimental CH profile thickness (black dots) at different Φs' as compared with the literature [135, 136]. The experimental CH layer thickness is estimated as the full width of the layer where the CH intensity is half of its maximum value. The error bar shows one standard deviation of the flame thickness measured from 3 different experiments and the absolute values represent the mean values. An excellent agreement is observed when compared with the flame thickness obtained from Dimotakis et al. [135] CH PLIF measurements (red dots). However, both the measurements appeared to be limited by the imaging resolution used and deviated from the absolute values obtained from the kinetic predictions by Turner et al. [136] (red curve). The flame thickness in

experiments is further assumed to be artificially broadened due to the number of the averages used which combines the lateral flame fluctuations during the data acquisition. Overall, the trends revealed by current and previous work are generally the same, depicting a range of lower flame thickness near stoichiometry, indicating the higher instability in the flame. It is suggested to increase the detection resolution and conduct single-laser-shot imaging to obtain true CH layer thickness. This concern is further discussed in *Section 6.2.6*. Such true flame thickness can serve as an input for the computational fluid dynamics (CFD) model and as benchmark data for kinetics model validation.

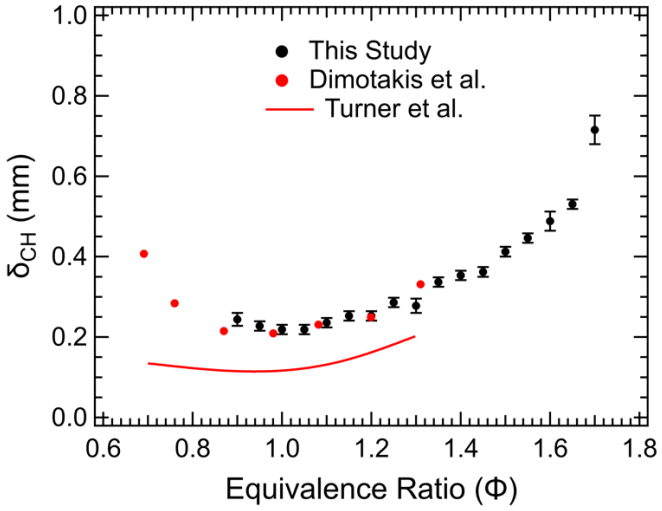

Figure 6.7 Experimental CH layer thickness as a function of Φ compared with the literature value.

The $CH_4/O_2/N_2$ conical flame with low jet velocities stabilized in the 4 mm jet burner was studied at a wide range of Φ = 1.0–1.7 keeping the cone height constant at ~16 mm. Figure 6.8 depicts the dependence of average SNR recorded as a function of Φ for two different sets of experiments. The SNR was calculated by taking a ratio of the average CH signal intensity of the

background-subtracted image and the standard deviation of the background noise fluctuation. The SNR slowly increases for slightly rich flames as compared to the stoichiometric case and peaks at $\Phi = 1.3$ due to peak CH number density; however, a steep decrease in SNR can be observed after that. Alden et al. [76] considered the peak CH signal intensity for SNR calculation and reported similar observations for saturation measurements of 2D CH PLIF investigations. Please note that the laser pulse energy, for this measurement, was maintained at 8 μJ/pulse which is well below the saturation pulse energy. Further SNR investigation on the saturated measurement was also performed by increasing the laser energy up to 62 μJ/pulse which lies above the saturation limit of 36 μJ/pulse. Figure 6.9 presents the plot showing the variation of average SNR as a function of the laser energy in $CH_4/O_2/N_2$ jet flame at $\Phi = 1.3$. It shows a non-linear rise in average SNR values with the increase in laser energy. An average SNR as high as ~70 and ~150 are obtained without and with saturation respectively. Approximately twice the SNR of each of these measurements (i.e. peak SNR obtained is close to 300) are obtained if SNR is to be calculated using peak CH signal intensity like in a previous study [76].

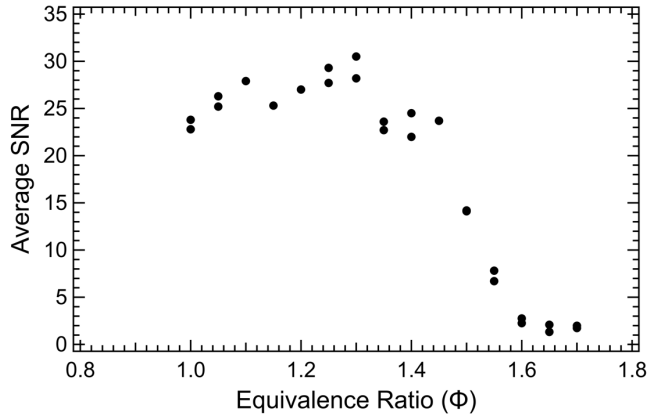

Figure 6.8 Average SNR from averaged CH images recorded with 8 µJ/pulse laser energy for $CH_4/O_2/N_2$ Bunsen flame as a function of Φ.

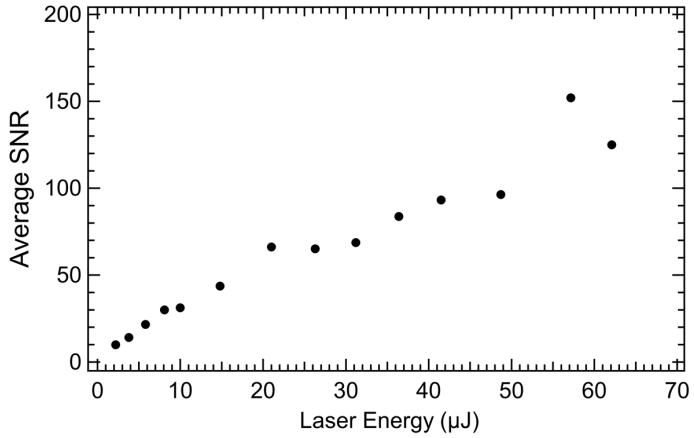

Figure 6.9 Average SNR from averaged CH images recorded for $CH_4/O_2/N_2$ Bunsen flame at Φ = 1.30 as a function of laser energy used.

Two different laminar flames involving CH_4 and C_2H_4 were investigated & shot-averaged CH PLIF images were captured for same Φ of 1.30 using a low-speed ICCD camera. These images were captured using a laser beam sheet of the height of 14 mm at approximately 3 mm above the burner exit. The beam sheet was cut-off from the top and bottom using a circular aperture and a

nearly equal intensity sheet was used to excite the CH radical. The images were recorded with the accumulation of 20 laser shots and an average of 50 camera frames. The intensifier gain was kept constant at 100%. Both images show a well-defined CH layer as shown in Figure 6.10, observed in the front region with different intensity levels. Due to the comparatively high number density present in C_2H_4 flame, the CH signal intensity observed is also higher (approximately 2×) as compared to CH_4 flame and hence further investigation was focused in C_2H_4 flame. The CH layer thickness (δ_{CH}), defined as the FWHM of the layer normal to the flame front planar surface, is measured to be similar (~ 0.28 μm) for both flames.

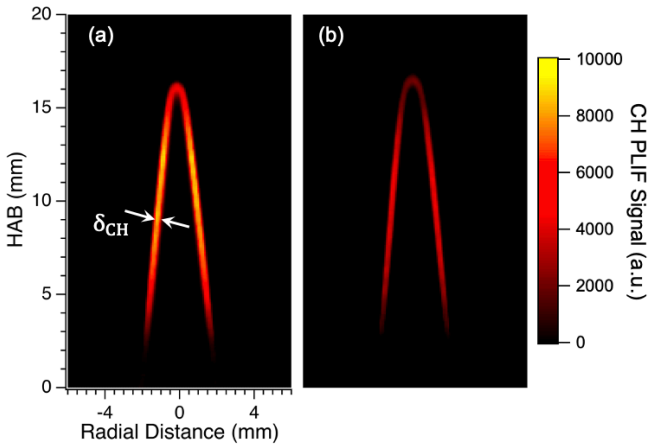

Figure 6.10 Averaged CH PLIF images for two different flames (a) $C_2H_4/O_2/N_2$, and (b) $CH_4/O_2/N_2$ at Φ = 1.30.

The potential of the fs diagnostic technique was extended to high-speed CH PLIF single-laser-shot imaging to visualize the flame ignition and the stabilization of $C_2H_4/O_2/N_2$ conical flame stabilized in the jet burner. The reactant mixture was fed through a central tube of 4 mm with an equivalence ratio of Φ = 1.30. A spark was created approximately 1 mm above the burner surface towards one side without disturbing the conical surface. The CH PLIF images were captured by

using a high-speed CMOS camera coupled with a HS-IRO unit. The intensifier gate and gain were set at 40 ns and 75% respectively. Approximately 2000 single-laser-shot CH PLIF flames were captured starting from t = 0 ms. Figure 6.11 shows the consecutive sequence of the first 7 ms highlighting the incipient propagating flame created due to a point spark. It is observed that the premixed combustion proceeds in transient processes in the form of combustion waves with thin fronts propagating into the unburnt combustibles. Such self-acceleratory phenomena along with combustion waves are the features of premixed combustion. This incipient flame shows a bulging structure in the CH profile with relatively colder fluid existing inside these CH zones. It takes approximately 4-5 ms (based on 5 repeated experiments) for the flame to be stabilized to form a conical shape. The basic structure of the flame with a rather smooth and thin flame surface is clearly captured by the instantaneous CH PLIF images. Similar characteristics and trends were observed in $CH_4/O_2/N_2$ conical flame (not shown here) as well.

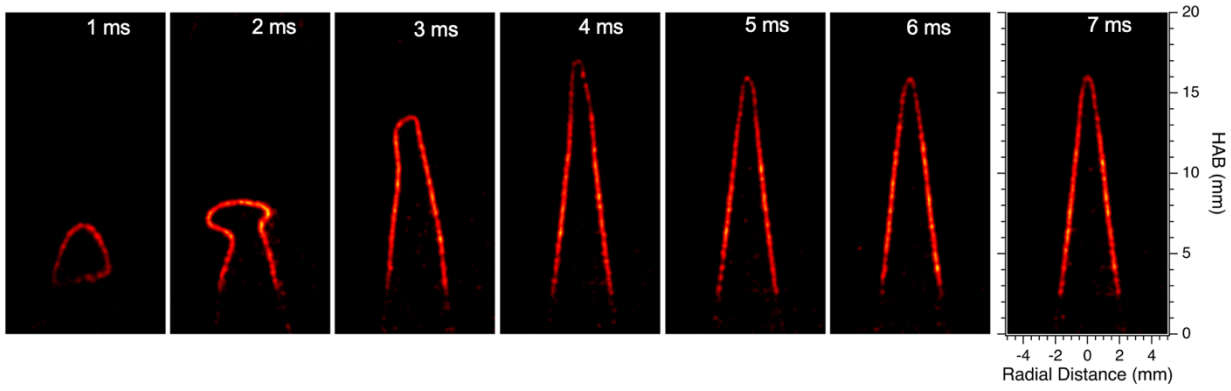

Figure 6.11 Sequence of consecutive single-shot CH PLIF images in $C_2H_4/O_2/N_2$ conical flame at Φ = 1.30 showing the flame ignition, propagation, and stabilization process.

6.2.5 Turbulent Flame Investigation

The non-premixed turbulent flame of $C_2H_4/H_2/N_2$ mixtures with air co-flow was further studied to demonstrate the potential of broadband fs excitation. Alden et al. [137] observed spectral interferences from HCHO while conducting CH PLIF measurements with broadband excitation pulse. Suppression of interferences is feasible by employing one of the following three approaches – (i) Use of appropriate spectral filters [137], (ii) Use of appropriate excitation wavelength [137], and (iii) High dilution of reactant mixture with N_2 (followed in this study). Both (i) and (ii) approaches aren't feasible for this study as the HCHO emission range lies within the filter transmission range and the fs laser used is broadband with FWHM ~2.5 nm. Initially, approximately 50% C_2H_4 and 25% N_2 were fed through the central tube to create a turbulent non-premixed flame. Similar spectral interferences with spatially separated HCHO were observed just inside the CH flame front (not shown here). These interferences can falsify the qualitative and quantitative interpretation of CH signals. The N_2 dilution was increased to 62% (i.e., 14.5% C_2H_4) to obtain HCHO interference-free CH images in turbulent flame. Such a high dilution of N_2 is also needed to obtain a clear bluish region, especially near the burner exit which is free from polycyclic aromatic hydrocarbons (PAHs) and soot [25].

In one set of experiments, we focused on the ignition of non-premixed turbulent combustion. The high velocities jet mixture was ignited by a spark generator near the burner exit, like the conical flame ignition. Figure 6.12 is the combination of 3 single-laser-shot frames showing how ignited flame propagates into the unburnt mixture region. The HAB is plotted against the time after ignition in milliseconds (ms) and only the right edge of the propagating flame is presented here. A smooth thin flame surface is observed near the burner exit. It is seen that the CH layer moves on the order of ~5.8 mm in 2 ms, corresponding to a convective velocity of

approximately ~ 3 m/s. More accurate velocity can be obtained by using a larger beam sheet and conducting CH imaging with high-repetition-rate (>1 kHz).

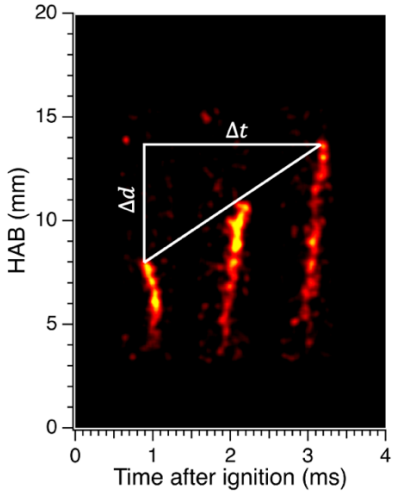

Figure 6.12 Consecutive single-laser-shot CH PLIF images recorded in $C_2H_4/O_2/N_2$ turbulent flame at 1 kHz repetition rate during the flame ignition process.

Figure 6.13 shows a consecutive 7-frame single-laser-shot CH PLIF image sequence with 1 ms spacing between successive images, corresponding to a 1-kHz acquisition rate. These images were captured using a laser beam sheet of a height of 14 mm at approximately 4 mm above the burner exit. The field-of-view for each raw image captured is ~40 mm × 40 mm, with a camera spatial resolution of ~40 μm/pixel. Such high-speed CH PLIF images are useful for examining local flame extinction, and the re-ignition process. Several interesting features like flame wrinkling, flame curvatures, and response to unsteady fluid mechanics are highlighted by these CH images. The visible region as shown in the first frame represents the region where the variation in laser beam intensity was nearly constant (within 10%) in vertical direction. The third frame with "(t_o + 2) ms" time-stamped shows that narrow streams of inner cold fluid connect the inner fuel jet

to the surrounding air through openings in the CH zone. The tips of the CH zones extending radially outward provide evidence that the fluid originating from the inside of the flame is responsible for the local extinction. The investigation of such locally extinguished combustion process along with flow/flame interaction stabilizing the flame front is important in understanding the flame stability in gas turbines, industrial oil furnaces, and burners. Further, the δ_{CH} observed in these non-premixed turbulent flames does not vary significantly from the premixed laminar jet flames.

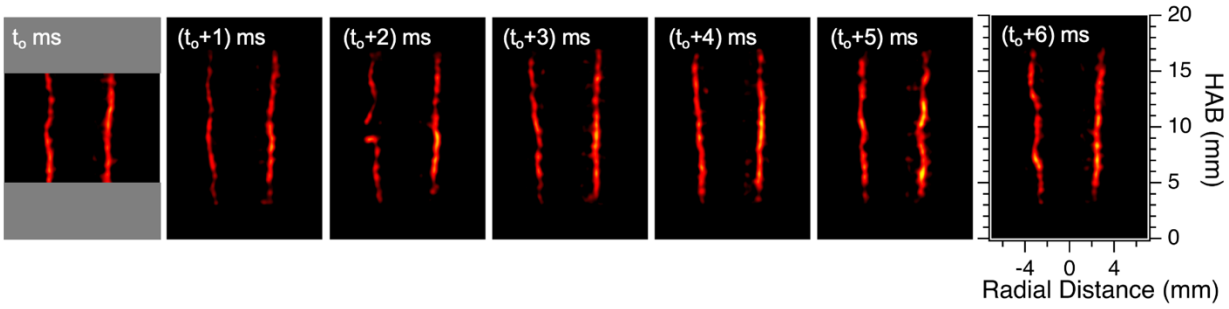

Figure 6.13 Sequence of consecutive single-shot CH PLIF images in $C_2H_4/O_2/N_2$ turbulent flame showing flame dynamics and transient phenomena like flame extinction.

6.2.6 Statistical Data Analysis

Further, a specific statistical trend in two flames $CH_4/O_2/N_2$ and $C_2H_4/O_2/N_2$, both at Φ = 1.30, are accessed from the consecutive 2000 single-laser-shot images captured after the 10 ms of ignition. Figure 6.14 presents the probability density function (PDF) of the mean CH PLIF signal using a kernel density estimation method [138, 139]. The histograms demonstrate that the PDF curves show an excellent fit with the underlying data. The shape of the mean CH signal PDF in both cases is approximately Gaussian (normal). The information on the arithmetic mean (μ) and standard deviation (σ) are also provided in the respective PDF plots. The mean CH PLIF signal in

the C_2H_4 is more than 2× higher than that in the CH_4 flame. Similarly, the σ is calculated to be approximately 5.5% and 7.5% for C_2H_4 and CH_4 flames respectively, it is likely that some CH signal in the latter flame may fall below certain threshold values of camera sensitivity causing the discrepancy.

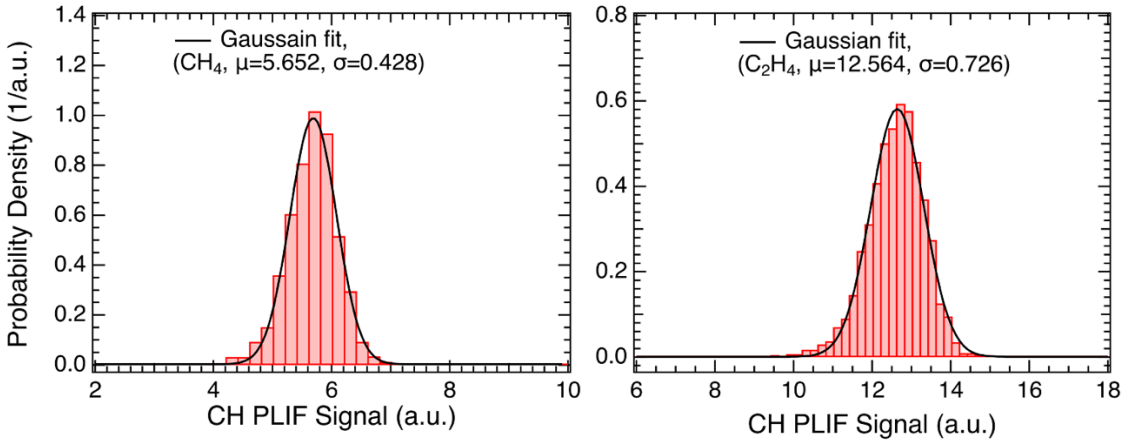

Figure 6.14 Probability density function for $CH_4/O_2/N_2$ (left side) and $C_2H_4/O_2/N_2$ flames (right side) at Φ = 1.30.

The statistical flame thickness trend was performed in $C_2H_4/O_2/N_2$ at Φ = 1.30 using 1000 consecutive single-laser-shot frames after the flame is fully stabilized. Figure 6.15 shows the approximately Gaussian PDF for flame thickness measurement. The CH PLIF thickness was measured normal to the flame front planar surface, as indicated in Figure 6.10, and was found to be ~0.214 mm, a little less than the one observed in averaged CH images (~0.28 mm). It was expected because averaged CH thickness tends to be artificially broadened due to slight lateral flame fluctuation. All the stabilized SS frames were averaged to confirm the repeatability of the flame thickness that was obtained with the ICCD camera.

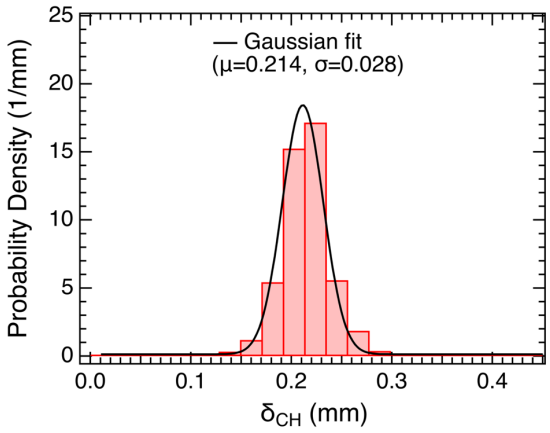

Figure 6.15 Probability density function for flame front thickness captured for $C_2H_4/O_2/N_2$ laminar flame at Φ = 1.30.

6.3 Summary and Recommendations

Overall, the fs imaging diagnostics coupled with high-efficient home-built SHG system is a simple and promising technique for CH PLIF imaging with high SNR. The current SHG setup was operated with only 2 mJ/pulse of pump energy, adding a buffer on the BBO crystal damage threshold. In future, the pump beam spot size can be increased on SHG optics such that full output capacity of the fs laser system (i.e., 6 mJ/pulse) may be utilized. While an increase in laser energy may result in additional complications such as ionization, dielectric breakdown, and further saturation effect, mitigating strategies such as laser pulse stretching and increasing in laser beam dimensionality can be explored. Such an improved CH PLIF imaging dimensionality can be a significant step for real-time tracking of the primary reaction zones in highly turbulent combustion measurement applications.

7. MULTI-PHOTON EXCITATION OF NITROGEN SECOND POSITIVE SYSTEM

7.1 Experimental Procedure

The experimental apparatus consists of an fs laser system, fuel tube, and detection system. The laser system consisting of a high conversion efficient direct frequency tripled system, along with optics and nonlinear crystals to generate UV radiation, has been described in detail elsewhere [109]. Briefly, a regeneratively amplified Ti: Sapphire laser system (Spectra-Physics, Model: Solstice Ace) generates fundamental output between 750–850 nm range at a 1-kHz-repetition rate with 6 mJ/pulse laser energy. In the present study, the pump beam tuned to 850 nm wavelength at ~2 mJ/pulse pumps a THG system to generate radiation near 283 nm. The 10 mm diameter fundamental beam was down collimated to ~5 mm by passing through a telescopic combination of +200 mm and -90 mm lens. This reduced-diameter beam was passed sequentially through two BBO crystals. The first one is used to generate the SHG beam, and the output beam mixes with the residual pump beam for the THG process. The near Gaussian 283 nm output beam was guided through several dichroic mirrors and then focused onto the flame using a +500-mm MgF_2 lens. In the case of LIF experiments, the fundamental beam at different wavelengths was directly focused on the probe region without any frequency conversion.

In both cases, the N_2 emission signal was collected orthogonal to the direction of the propagation of the laser beam sheet using two detection systems: (i) a spectroscopic study using a spectrometer (Princeton Instruments, Model: Isoplane 160) fitted with an intensified charge-coupled device (ICCD) camera (Princeton Instruments, PI-MAX4) and (ii) a shot-averaged imaging study using the ICCD camera alone. The spectrometer-camera system was calibrated for wavelength and intensity using a dual set of calibration lamps (Princeton Instruments, Model: IntelliCal) consisting of Hg/Ne-Ar atomic emission and an LED-based light source. The horizontal

entrance slit of the spectrometer was positioned such that it lies in the same horizontal plane as that of the laser line. The entrance slit was open to approximately ~100 μm. An additional +60-mm focal length plano-convex lens was placed in between the probe region and the spectrometer system to focus the flame emission into the entrance slit and optimize the signal collection efficiency.

7.2 Results and Discussions

7.2.1 REMPI using a third harmonic beam

7.2.1.1 Excitation scan

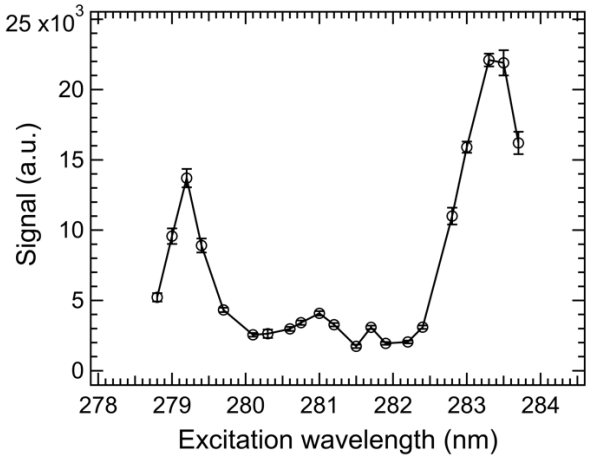

Figure 7.1 N_2 fluorescence signal response to the excitation wavelength. Solid black lines are drawn to guide the eye.

A 1:1 mixture of N_2 and Ar was fed through a tube of 4 mm ID and N_2 emission was collected at a range of excitation wavelengths. The laser line was focused at ~5 mm above the tube surface. Figure 7.1 shows the dependence on different wavelengths and is obtained by plotting the averaged N_2 signal emitted near 337 nm versus the corresponding excitation wavelengths. Each

data point (red dots) accumulates the fluorescence signal of 300 laser shots and an average of 30 camera frames. The intensifier gain and gate were set at 100% and 50 ns respectively. The error bars represent one standard deviation calculated from 30 individual frames recorded for each data point. The black solid line is drawn as a guide to the eyes.

Alden et al. [78] claimed that six complex molecular spectral structures are available within the 279-286 nm range and observed two-photon resonance $a^1\Pi_g(v' = 1) \leftarrow X^1\Sigma_g^+(v'' = 0)$ and three-photon resonance $b^1\Pi_u(v' = 6) \leftarrow X^1\Sigma_g^+(v'' = 0)$ near 283 and 285 nm respectively. The latter excitation wavelength lies outside the third harmonic tuning range, in our case. However, we observed another resonance-enhanced peak at 279 nm likely due to two-photon resonance $B'^3\Sigma_u^+(v' = 4) \leftarrow X^1\Sigma_g^+(v'' = 0)$transition in addition to widely known a – X transition. Tilford et al. [140] claim that the $B' - X$ is somewhat weaker than the $a - X$ transition which is what we observed in this study as well. Quantitatively, $a - X$ is almost 1.8 times stronger than $B' - X$ excitation transition obtained from this study.

7.2.1.2 Laser Energy Dependence

The two-photon transition for these two-excitation wavelengths was verified via the energy dependence of the signal intensity. To conduct the energy scan, a thin variable neutral density beam attenuator was used which allows well-controlled measurements without altering the beam path or its properties. As is observed in Figure 7.2, the energy dependencies for the two-photon excitation in the $a^1\Pi_g$ and $B'^3\Sigma_u^+$ exhibited almost the quadratic power functions. The error bars represent one standard deviation calculated from 30 individual frames recorded for each data point.

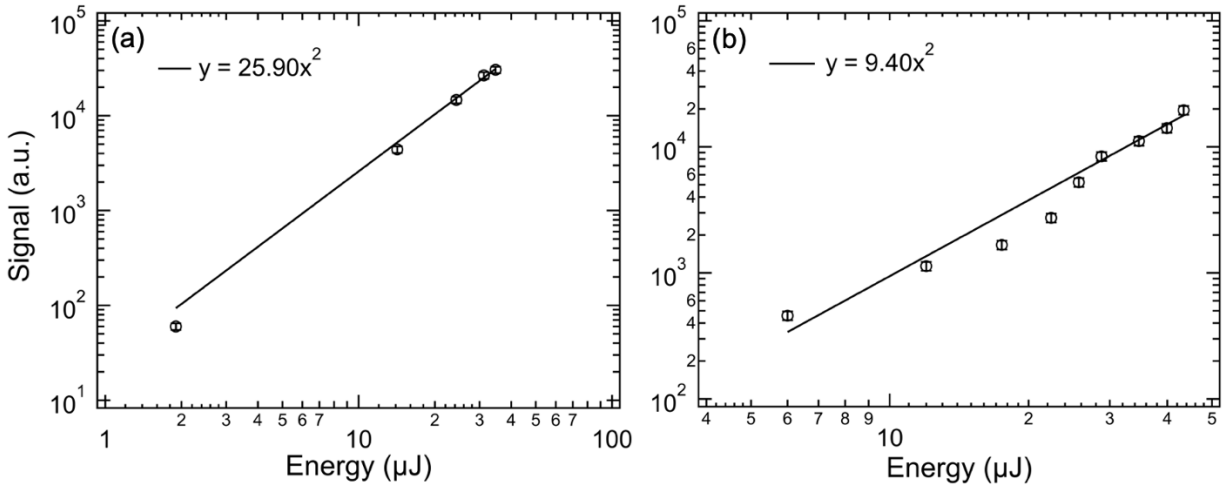

Figure 7.2 N_2 fluorescence signal as a function of laser energy for an excitation wavelength of (a) 279 nm and (b) 283 nm. A fit (solid black curve) is a quadratic fit to the experimental data (black open circles).

7.2.1.3 Emission Spectral Study

Initially, the entire spectral range of interest from 300 – 800 nm was covered using 300 lines/mm grating and 300 nm Blaze wavelength by changing the central wavelength. Shown in Figure 7.3a is the N_2 emission spectrum recorded at atmospheric pressure and room temperature. The excitation wavelength was maintained at 283.3 nm with laser pulse energy of 30 μJ/pulse (approximately 9.50×10^4 μJ/cm^2). The intensifier gain and gate width were kept constant at 100% and 50 ns, respectively. The spectra recorded are an average of 30 frames with each frame containing an on-chip accumulation of 300 laser shots. Table 7.1 summarizes the band heads and origins of the $C^3\Pi_u - B^3\Pi_g$ SPS of N_2 molecule observed in 300 – 400 nm region. Also observed is the second-order SPS. Additionally, the transmission curve of the filter (Thorlabs, Part No. FGS900S) with a peak transmission efficiency of ~80% used for N_2 molecule imaging experiments is indicated by the dotted blue curve. No fluorescence interferences from other combustion species

in the spectral range of interest are observed in the flame investigated during the fs N_2 molecule imaging. The two of the strongest emission of SPS were captured using high-resolution grating with 1200 lines/mm and a reduced spectrometer slit to improve the spectral resolution. Figure 7.3b presents the corresponding second positive (0-0), (1-2), and (0-1) bands of N_2 near 337-, 353- and 357 nm respectively, obtained in a ~300 K 1:1 mixture of N_2/Ar flow.

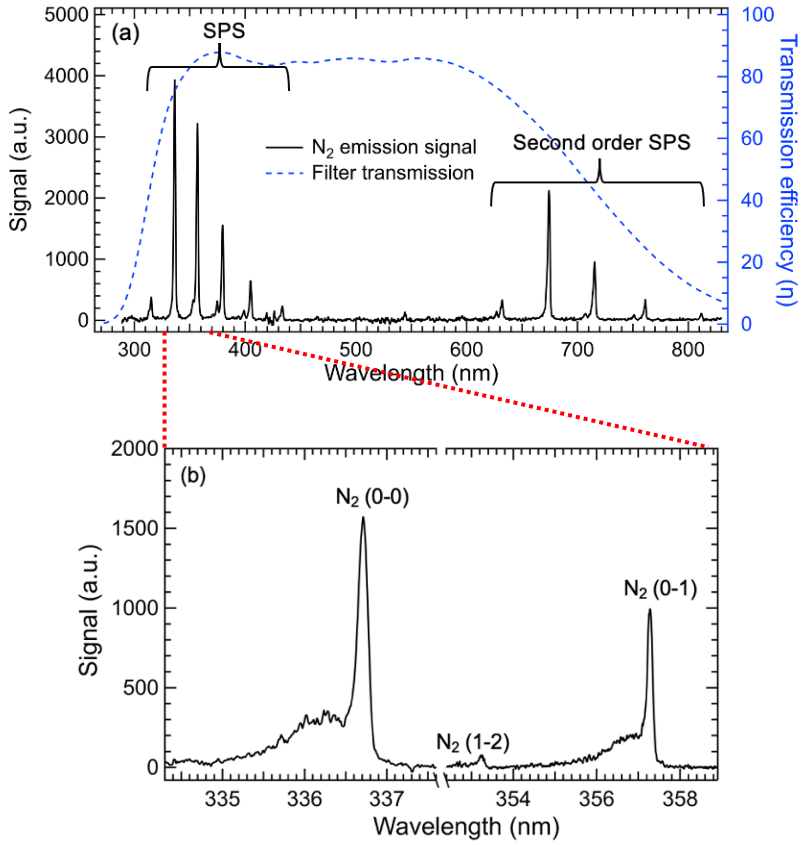

Figure 7.3 (a) N_2 C-B emission spectra showing SPS using 300 lines/mm grating. The emission lines shown between 600 to 820 nm are the second order of N_2 SPS. The dotted blue curve represents the transmission curve of the filter used for the imaging experiments in the subsequent study. (b) High-resolution spectrum of N_2 C-B (0-0), (1-2) and (0,1) bands.

Table 7.1 The band heads and origins of C-B SPS of N_2 molecule

Emission line	Wavelength (nm)	Intensity (a.u.)	Transition $\nu' - \nu''$
i	315.9	400	1 – 0
ii	337.1	4000	0 – 0
iii	353.6	150	1 – 2
iv	357.7	3200	0 – 1
v	375.5	120	1 – 3
vi	380.4	1500	0 – 2
vii	399.8	50	1 – 4
viii	405.9	600	0 – 3
ix	434.3	100	0 – 4

7.2.1.4 Single-Laser-Shot and Shot-Averaged Imaging Investigations

Shot-averaged N_2 fluorescence 1D measurements were performed along the radial axis using an ICCD camera and a sample image is shown in Figure 7.4a. The image was captured with the laser beam focused at 5 mm above the 4 mm ID tube with a 1:1 mixture of N_2/Ar fed at ~300 K. It should be noted that the image accumulates the fluorescence signal of 50 laser shots and an average of 30 such camera frames with intensifier gain set to 100%. The typical width of the line image recorded filled about 8 pixels in the camera plane which corresponds to a beam waist of approx. 0.100 mm. The SNR was calculated by taking a ratio of the peak/ average N_2 signal intensity of the background-subtracted image and the standard deviation of the background noise fluctuation and termed as peak/average SNR. The peak and average SNR for the averaged N_2

molecule image is calculated to be 2530 & 1590 respectively. Similarly, the average SNR for the SS image (not shown here) is calculated to be approx. 38. Figure 7.4b shows the corresponding fluorescence signals obtained by vertically integrating the line image shown in Figure 7.4a.

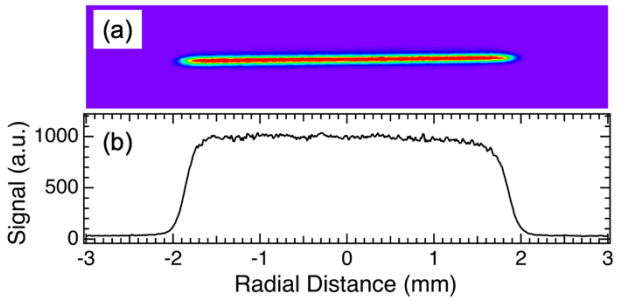

Figure 7.4 Sample (a) single-laser-shot image (b) averaged image of N_2 C-B emission lines capturing all the SPS. The color distribution is based on a rainbow color palette with red and purple being the maximum and minimum signals, respectively. The third harmonic laser beam was focused at 5 mm above the 4 mm ID tube exit.

7.2.2 Laser-Induced Fluorescence using Fundamental Beam

7.2.2.1 Fs Laser Pulse Duration Measurement

The pulse duration measurement is essential for the investigation of fundamental wavelength dependence on N_2 emission signals at near constant pulse width. Figure 7.5 presents the minimum pulse duration recorded for each fundamental wavelength investigated. The uncertainty in measurement is calculated to be ~ 4%, obtained from one standard deviation of three different measurements. The pulse duration remains constant nearly up to 830 nm and starts decreasing beyond it. It should be noted that the Ti: sapphire laser system is optimized for a fundamental wavelength of 800 nm. Although the laser can be tuned between 750–850 nm, the

laser spectrum becomes slightly asymmetric at the right end of the tuning range. It is primarily due to the gain-pulling effect towards the Ti: sapphire gain peak on the blue side of the spectrum. As a result, two lobe-like structures near the wings at the condition of minimum pulse duration reducing the time width of the signal (i. e. ΔS) in Equation (1).

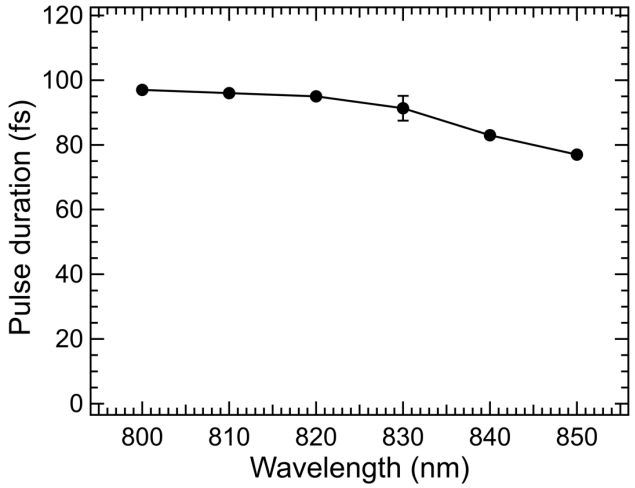

Figure 7.5 Pulse duration as a response to the fundamental laser wavelength.

7.2.2.2 Spectroscopic Investigation

The multiphoton spectroscopy of N_2 molecule was further characterized via the $a''^1\Sigma_g^+ - X^1\Sigma_g^+$ transition using the fundamental wavelength of the Ti: sapphire laser system. A single-photon transition between the $a''^1\Sigma_g^+ - X^1\Sigma_g^+$ states is dipole forbidden. Figure 7.6 displays an eight-photon LIF excitation spectrum recorded using ICCD camera placed perpendicular to the laser beam. The laser beam focused at 5 mm above the 4 mm ID tube with a 1:1 mixture of N_2/Ar fed at ~300 K. The laser beam wavelength was varied from 800–850 nm. To the best of our knowledge, this is the first systematic experimental investigation of the dependence of the N_2 LIF

signal on the fundamental beam wavelength especially at low energies. The black and red curves show the excitation spectrum trends recorded for 0.5 mJ/pulse and 0.3 mJ/pulse laser beam energy. The fluorescence signal for the laser energy of 0.3 mJ/pulse is multiplied by a factor of 20 for clear visualization. It is observed that on-resonance wavelength at 810 nm excites the $a''^1\Sigma_g^+ - X^1\Sigma_g^+$ transition via an eight-photon process. Approximately one-third of the peak N_2 LIF signal is obtained at 800 nm which could be due to the partial overlap of the right wing of the spectral region with the peak excitation wavelength of 808 nm. However, no such signals were observed for wavelength range of 820–850 nm at 0.3 mJ/pulse laser energy as indicated by the flat blue curve. The laser energy was raised to 0.5 mJ/pulse to observe the N_2 LIF signal dependence on the excitation wavelength. Approximately 15% of the peak N_2 signal was observed even for the off-resonance wavelength. The possible reasoning requires the investigation of the fluorescence spectra.

The majority of the fluorescence signal observed due to the $a''^1\Sigma_g^+ - X^1\Sigma_g^+$ excitation transition is the SPS from the $C^3\Pi_u - B^3\Pi_g$ transition (as indicated in Figure 7.7) which is well-known 337 nm band of nitrogen lasers. The $C^3\Pi_u$ excited state is populated via collisional relaxation of the $a''^1\Sigma_g^+$ state [96]. In addition to the emission of SPS, as laser energy is increased additional fluorescence emission was also observed at 391 nm, originating from $B^2\Sigma_u^+ - X^2\Sigma_g^+$ transition in N_2^+. The N_2^+ $B^2\Sigma_u^+$ excited state is likely to be populated via optical excitation of electronically excited neutral states of N_2 produced via collisional quenching of the $a''^1\Sigma_g^+$ state [96]. The N_2^+ ion is produced once the laser energy reached the threshold level which is more evident in Fig. 8 as the energy is raised to 1 mJ/pulse. The third order of $a^1\Pi_g \leftarrow X^1\Sigma_g^+$ REMPI signal was not observed at 850 nm, which could be possibly due to following three reasons - weak

REMPI emission signal [96], lower laser energy used during the experiment and tendency of laser wavelength to get blue-shifted at the right end of the tuning range.

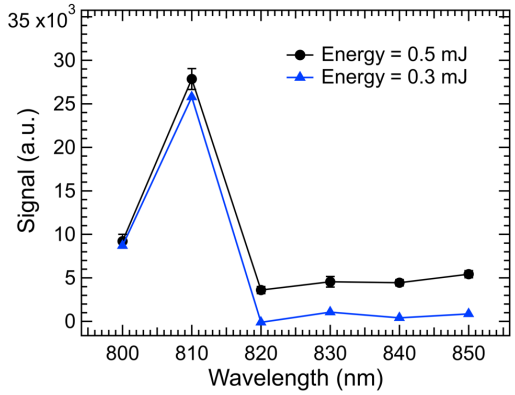

Figure 7.6 Dependence of the N_2 C-B emission signal on the fundamental beam wavelength at two different laser energies. Each emission signal value at 0.3 mJ is multiplied by a factor of 20 for better visualization of the laser energy effect.

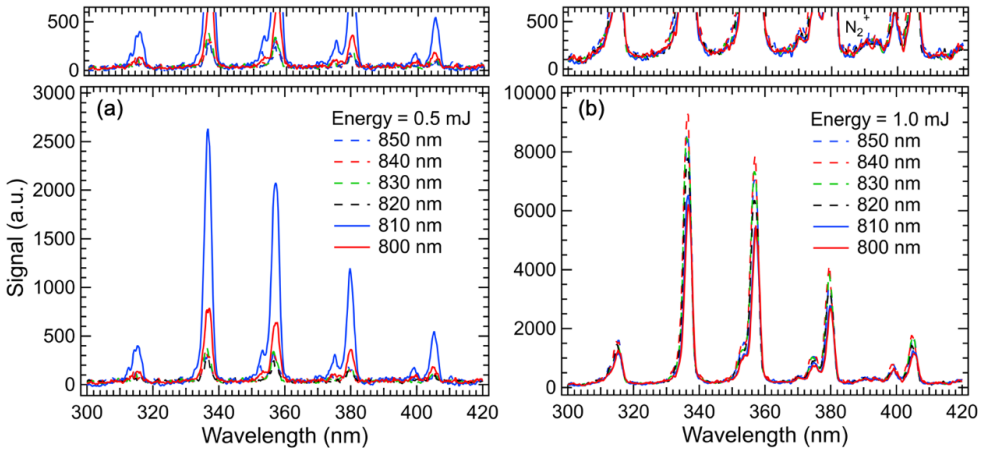

Figure 7.7 N_2 C-B emission signal dependence on excitation fundamental wavelength for a laser beam energy of (a) 0.5 mJ and (b) 1 mJ with a zoomed-in section showing the appearance of N_2^+ on the top.

Further, a laser energy scan was performed for the excitation wavelength of 810 nm using a laser beam attenuator without altering the beam path and its properties. Two strong emission lines - N_2 (0-0) and N_2 (0-1) near 337 nm and 357 nm were integrated respectively, and the signal response to the laser energy used is plotted in Figure 7.8. Both the emission signal shows a similar trend. It is further likely that the N_2 emission reached the saturation level once the energy is above the threshold of 0.5 mJ. The signal strength shows an increase by a factor of approx. 60 when the energy is raised from 0.1 mJ to 0.5 mJ.

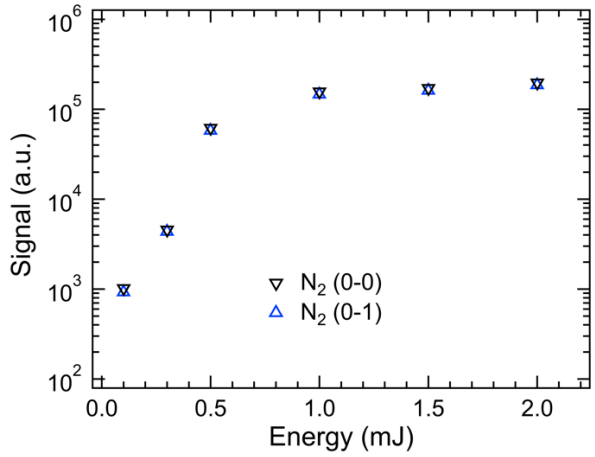

Figure 7.8 N_2 C-B emission signal recorded as a function of laser energy for an excitation wavelength of 810 nm. Blue upright triangles denote the N_2 (0-1) emission band whereas the N_2 (0-0) emission band is represented by black inverted triangles.

Figure 7.9 shows the fluorescence lifetimes observed in a mixture 1:1 of N_2 and Ar as indicated by black closed circle. A narrow time gate of 10 ns synchronized with the excitation pulse is used to sweep the fluorescence profile. The observed emission signals for N_2 ($C^3\Pi_u$) state (Figure 7.9a) and N_2^+ ($B^2\Sigma_u^+$) state (Figure 7.9b) are normalized by the individual peak signal recorded at zero delay. The falling edge of each fluorescence curve is fitted with an exponential

decay function, given by equation $I(t) = I_0 e^{-t/\tau}$ where I_0 is fluorescence intensity immediately after excitation, τ is the fluorescence lifetime and $I(t)$ is the fluorescence intensity at time t. The mean lifetime of approx. 7.3 ns and 800 ps was recorded for SPS and FNS respectively which is in accordance with literatures [141, 142]. The comparative faster decay of 391 nm is further evident by the inset in Fig. 10b where 391 nm decays by almost 100% as compared to 394 nm line (one of the emission lines of SPS) which decays only by ~40% for 1 ns raise in delay time. These reported non-radiative lifetimes are expectedly much shorter than the spontaneous lifetime. It is well known that the spontaneous emission lifetimes of N_2^+ $(B^2\Sigma_u^+)$ and N_2 $(C^3\Pi_u)$ are approximately 60 ns [141, 143] and 40 ns [28, 30, 144-148] respectively.

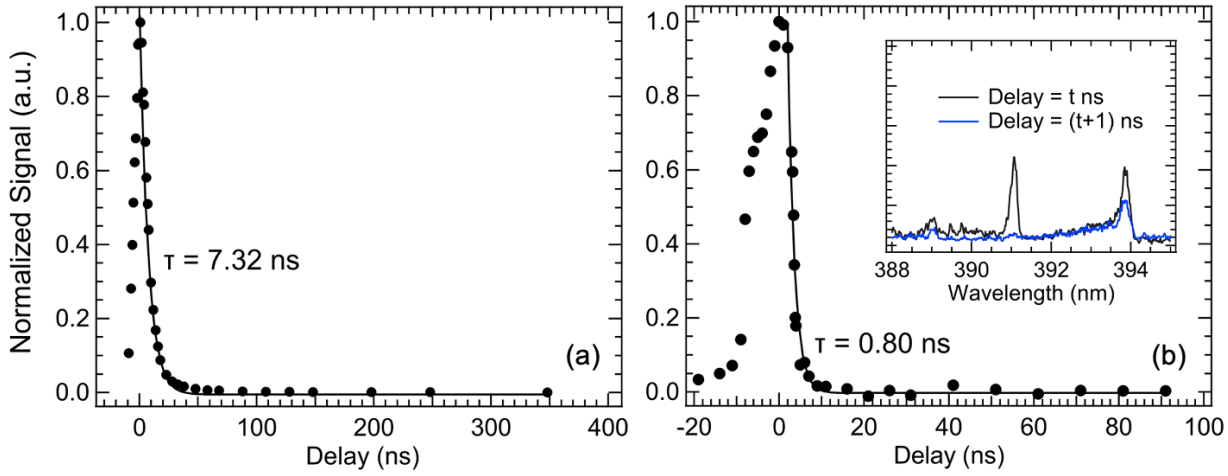

Figure 7.9 Time-resolved fluorescence emission at (a) SPS (b) 391 nm. The inset in (b) indicates the faster decay of the N_2^+ $(B^2\Sigma_u^+)$ state as compared to one of the emission lines of N_2 $(C^3\Pi_u)$ state.

7.2.2.3 Imaging Measurement Study

Figure 7.10a and 7.10b present the shot-averaged eight-photons N_2 LIF emission imaged using an ICCD camera for laser beam energies of 0.3 mJ and 0.5 mJ. These images were captured with the laser beam focused at 5 mm above the 4 mm ID tube with a 1:1 mixture of N_2/Ar fed at ~300 K. It should be noted that the image for 0.5 mJ accumulates the fluorescence signal of only one laser shots and an average of 30 camera frames with intensifier gain set to 30% only. The signal count for 0.3 mJ laser energy is multiplied by a factor of 20 for better visualization. The beam waist is estimated to be ~0.100 mm, obtained from the full-width-at-half-maximum (FWHM) of the recorded line images. The peak and average SNR for the averaged N_2 LIF image at 0.5 mJ laser pulse energy is calculated to be 1750 & 1100 respectively.

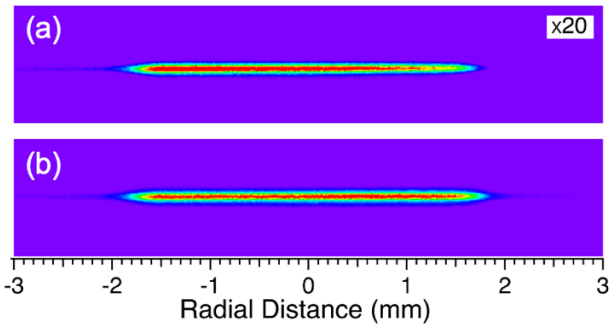

Figure 7.10 Sample averaged image of N_2 C-B emission lines capturing all the SPS for laser energies of (a) 0.3 mJ and (b) 0.5 mJ. The emission signal at 0.3 mJ is multiplied by a factor of 20 for better visualization of the laser energy effect. The color distribution is based on a rainbow color palette with red and purple being maximum and minimum signals, respectively.

Figure 7.11 presents the SS N_2 LIF image recorded for the laser beam energy of 0.5 mJ. The intensifier gain was increased to 100% for better SNR. The peak and average SNR for the SS N_2 molecule image is calculated to be 760 and 380 respectively. Even though this work is focused on the excitation using multiple photons at 810 nm wavelength, the substantially strong SS signals of N_2 fluorescence and high SNR are of great interest for diagnostics purposes, for instance, in combustion studies and nonflammable flow fields.

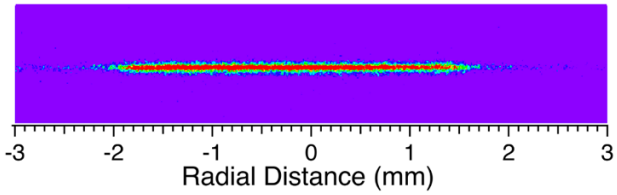

Figure 7.11 Sample SS image of N_2 LIF C-B emission lines capturing all the SPS for laser energies of 0.5 mJ at an excitation wavelength of 810 nm. The color distribution is based on a rainbow color palette with red and purple being maximum and minimum signals, respectively.

7.3 Summary and Recommendations

The shot-averaged and SS images of N_2 SPS with an extremely high SNR were achieved using ultrashort pulse, fs multi-photon excitation scheme. The promising results from the present study give us a firm belief that fs multiphoton scheme (at 283 nm as well as 810 nm) has a great potential for applications in harsh environments such as high temperature and pressure burners and gas turbines. We plan to utilize the potential of such N_2 fluorescence signal levels for efficient flow velocity measurements [82, 149, 150] and kHz-rate SS thermometry investigations in the near future.

8. CONCLUSION AND RECOMMENDATIONS FOR FUTURE WORK

This chapter summarizes the results from Chapter 3 through Chapter 7. The main purpose of this thesis work is to develop novel approaches and improve existing laser diagnostics techniques based on ultrafast laser pulse excitation laser pulses. The limitations of the current diagnostics developed in this work are also discussed along with the recommendations for further work to resolve some of these deficiencies.

8.1 Atmospheric and High-pressure Chemical Species Imaging

In this work, we have successfully implemented the ultrashort fs laser pulses for chemical species imaging in atmospheric as well as elevated-pressure conditions. Ultrashort fs-pulse excitation schemes are more attractive because of the efficient multi-photon excitation and photolytic-interference-free kHz-rate imaging capability. The fundamental fs beam pumping a home-built, high-conversion efficiency harmonic-generation scheme is utilized for atomic and molecular species imaging in gas cells, atmospheric-pressure flames, and elevated-pressure flames.

For the fs-TPLIF measurement studies of the H atom in high-pressure flames up to 10 bar, a home-built, high-conversion efficient FHG scheme was used to overcome the transmission losses via thick optical windows. The laser energy dependence of the H-TPLIF signal showed quadratic behavior in higher pressures as well. ASE-interference-free H profiles were reported, possibly due to the stretching of fs pulses by the burner window. The pressure-dependence study showed a nonlinear decay of the fs H-TPLIF signal as opposed to the expected linear increase in the H number density. The measured H fluorescence signal as a function of ϕ is well predicted by Cantera and UNICORN code calculations. At lower-pressure flames (1 bar & 2 bar) reasonable agreements were obtained between the measured signals and code calculations, however, significant

discrepancies were observed on the lean side at higher pressures. Several line images were recorded at different flame heights and the generated 2D H maps are well predicted by UNICORN calculations.

Further, for CH-PLIF high-speed imaging measurements using the broadband pulses, an ultrashort-pulse fs excitation scheme was developed for the first time. The complexity of the laser and optics setup was minimized by simply employing a high-conversion efficiency direct frequency-doubled SHG system to generate high-energy laser pulses near 390 nm. A detailed study on the excitation/ emission, flame thickness, and saturation issues due to high-energy laser pulses was conducted. A systematic study on the SNR dependence on ϕ and laser energy was conducted, and the result showed an average SNR as high as ~70 and a peak SNR as high as ~150 is achievable without saturation of the excitation transition. Kilohertz-rate imaging sequence of the first few CH PLIF images in laminar flame showcased the flame ignition, propagation, and stabilization process. Overall, the fs imaging diagnostics coupled with the SHG system is a simple and promising technique for CH PLIF imaging with reasonably high SNR.

Subsequently, the fs fundamental beam and the third harmonic laser beam were utilized to perform the fluorescence studies and investigate the possible multi-photon excitation scheme for N_2 molecules. The home-built, high-efficient third-harmonic fs beam near 283 nm exploited the N_2 REMPI technique via (2+3) photon excitation. Similarly, fs beam near 810-nm laser pulses exploited $a''^1\Sigma_g^+ - X^1\Sigma_g^+$ transition via an eight-photon process to populate the $C^3\Pi_u$ excited state of N_2 molecules via collisional relaxation of $a''^1\Sigma_g^+$ state. Also, shot-averaged and SS images of N_2 SPS with a high SNR were achieved using the ultrashort pulse, fs multi-photon excitation scheme.

8.2 Multi-Species Imaging and Temperature Measurement

One-dimensional imaging of the temperature profile wwas been demonstrated in $CH_4/O_2/N_2$/Kr Bunsen flame via fs Kr TPLIF measurements. The Kr TPLIF line images were recorded at several HAB locations and converted to radial temperature profiles. The fs TPLIF provided an easy way to extract the flame temperature simply by taking the inverse square of the fluorescence signal and approximating the quenching rate as $T^{-0.5}$. These temperature profiles agreed well with 1D flame model predictions. This fs-TPLIF is a promising approach and can be extended for thermometry purposes for higher-pressure flames during future studies.

Further, the simultaneous Kr-based thermometry and H-atom imaging using a single fs laser pulse have been demonstrated in a $CH_4/O_2/N_2$/Kr Bunsen flame. The two species were excited at an intermediate wavelength near 204.5 nm taking advantage of broadband fs pulses having linewidths in excess of 400 cm^{-1}. The Kr fluorescence profiles and the resulting 1D temperature profiles along with H atom fluorescence profiles were acquired along a line simultaneously. Such 1D temperature profiles were applied for in-situ quenching corrections to obtain quantitative H atom concentration. The technique has prospects for kHz-rate simultaneous SS imaging in future applications through signal enhancement by optimizing the current apparatus.

8.3 Limitations and Future Recommendations

The fs laser diagnostics coupled with the harmonic generation system has taken a large step forward in obtaining fluorescence measurements over a wider pressure range with increased efficiency and accuracy. However, there are still some limitations within the system that can be resolved during future work. Although the in-situ temperature is calculated from the experiment, the branching ratio is obtained from the experiment only at the low-pressure condition and are

extrapolated to the atmospheric and high-pressure condition. At high-pressure conditions, the fluorescence decay becomes significantly faster which is difficult to measure experimentally. However, in the future, such issues can be addressed by utilizing state-of-art streak cameras which have a nominal response time of ~5 ps. Alternatively, the fs-TPLIF diagnostics developed here can be coupled with a fast-response-time PMT to measure in-situ quenching rates even at high pressures.

In addition, future work could be extended in the kHz-rate SS as well as planar measurements. The maximum available pump energy is 6 mJ/pulse at kHz repetition rates. However, only one-third of pump energy was utilized to operate the current harmonic generation setup considering potential BBO crystal damage threshold. In the future, the pump beam diameter can be increased to utilize the full laser energy, and the signal can be enhanced by approximately nine times, especially for species with two-photon processes such as H and Kr. Such optimization can improve image dimensionality which can be a significant step forward in kHz-rate imaging in fundamental flame studies as well as practical combustion diagnostics.

8.4 Overall Summary

As a combustion diagnostics community, we have always sought photolytic interference-free imaging capabilities, efficient multi-photon excitation, and accurate measurements with the inception of laser and optical-based diagnostics. The advancement of the ultrashort, broadband fs laser pulses are the key enabler for non-linear diagnostics with significantly higher laser pulse intensities compared to conventional pulses. They have shown encouraging outcomes in a number of laser diagnostics for combustion applications along with multi-species imaging capabilities. The present fs-TPLIF investigation provides the full 2D atomic and molecular species concentration

maps much more effectively and efficiently compared to the conventional LIF techniques. The demonstrated fs laser pumped harmonic generation technique further keeps the door ajar for a fundamental study of atomic and molecular species as well as their applications in turbulent flame dynamics and high-pressure combustion processes.

REFERENCES

[1] A. Konnov, Fundamental combustion, Division of Combustion Physics, Department of Physics, Lund University Sweden, 2021.

[2] F.N. Egolfopoulos, C.K. Law, Chain mechanisms in the overall reaction orders in laminar flame propagation, Combustion and Flame 80 (1990) 7-16.

[3] T. Paschal, P. Parajuli, M.A. Turner, E.L. Petersen, W.D. Kulatilaka, High-Speed OH* and CH* Chemiluminescence Imaging and OH Planar Laser-Induced Fluorescence (PLIF) in Spherically Expanding Flames, AIAA Scitech 2019 Forum.

[4] M. Allen, R. Hanson, Planar Laser-Induced-Fluorescence Monitoring Of OH In A Spray Flame, Optical Engineering 25 (1986) 251309.

[5] G. Singla, P. Scouflaire, C. Rolon, S. Candel, Planar laser-induced fluorescence of OH in high-pressure cryogenic LOx/GH2 jet flames, Combustion and Flame 144 (2006) 151-169.

[6] M. Tanahashi, S. Murakami, G.-M. Choi, Y. Fukuchi, T. Miyauchi, Simultaneous CH–OH PLIF and stereoscopic PIV measurements of turbulent premixed flames, Proceedings of the Combustion Institute 30 (2005) 1665-1672.

[7] J.M. Donbar, J.F. Driscoll, C.D. Carter, Reaction zone structure in turbulent nonpremixed jet flames—from CH-OH PLIF images, Combustion and Flame 122 (2000) 1-19.

[8] D.L. Baulch, C.J. Cobos, R.A. Cox, C. Esser, P. Frank, T. Just, J.A. Kerr, M.J. Pilling, J. Troe, R.W. Walker, J. Warnatz, Evaluated Kinetic Data for Combustion Modelling, Journal of Physical and Chemical Reference Data 21 (1992) 411-734.

[9] J.E. Rehm, P.H. Paul, Reaction rate imaging, Proceedings of the Combustion Institute 28 (2000) 1775-1782.

[10] J.A. Miller, R.J. Kee, C.K. Westbrook, Chemical Kinetics and Combustion Modeling, Annual Review of Physical Chemistry 41 (1990) 345-387.

[11] P. Glarborg, Hidden interactions—Trace species governing combustion and emissions, Proceedings of the Combustion Institute 31 (2007) 77-98.

[12] R. Barlow, G. Fiechtner, J. Chen, Oxygen atom concentrations and no production rates in a turbulent H2/N2 jet flame, 1996.

[13] S.R. Turns, An Introduction to Combustion: Concepts and Applications, third ed., McGraw-Hill Education2011.

[14] N.J. Parziale, M.S. Smith, E.C. Marineau, Krypton tagging velocimetry of an underexpanded jet, Appl. Opt. 54 (2015) 5094-5101.

[15] M.A. Mustafa, N.J. Parziale, Simplified read schemes for krypton tagging velocimetry in N2 and air, Opt. Lett. 43 (2018) 2909-2912.

[16] D. Zelenak, V. Narayanaswamy, Demonstration of a two-line Kr PLIF thermometry technique for gaseous combustion applications, Opt. Lett. 44 (2019) 367-370.

[17] A.G. Hsu, V. Narayanaswamy, N.T. Clemens, J.H. Frank, Mixture fraction imaging in turbulent non-premixed flames with two-photon LIF of krypton, Proceedings of the Combustion Institute 33 (2011) 759-766.

[18] V. Narayanaswamy, R. Burns, N.T. Clemens, Kr-PLIF for scalar imaging in supersonic flows, Opt. Lett. 36 (2011) 4185-4187.

[19] O. Park, R.A. Burns, O.R.H. Buxton, N.T. Clemens, Mixture fraction, soot volume fraction, and velocity imaging in the soot-inception region of a turbulent non-premixed jet flame, Proceedings of the Combustion Institute 36 (2017) 899-907.

[20] N. Lamoureux, K.K. Foo, P. Desgroux, Quantitative measurement of atomic hydrogen in low-pressure methane flames using two-photon LIF calibrated by krypton, Combustion and Flame 224 (2021) 248-259.

[21] P.H. Paul, H.N. Najm, Planar laser-induced fluorescence imaging of flame heat release rate, Symposium (International) on Combustion 27 (1998) 43-50.

[22] J.M. Donbar, J.F. Driscoll, C.D. Carter, Strain rates measured along the wrinkled flame contour within turbulent non-premixed jet flames, Combustion and Flame 125 (2001) 1239-1257.

[23] C.M. Vagelopoulos, J.H. Frank, An experimental and numerical study on the adequacy of CH as a flame marker in premixed methane flames, Proceedings of the Combustion Institute 30 (2005) 241-249.

[24] N. Jiang, R.A. Patton, W.R. Lempert, J.A. Sutton, Development of high-repetition rate CH PLIF imaging in turbulent nonpremixed flames, Proceedings of the Combustion Institute 33 (2011) 767-774.

[25] D. Han, M.G. Mungal, Simultaneous measurement of velocity and CH layer distribution in turbulent non-premixed flames, Proceedings of the Combustion Institute 28 (2000) 261-267.

[26] K.T. Walsh, M.B. Long, M.A. Tanoff, M.D. Smooke, Experimental and computational study of CH, CH*, and OH* in an axisymmetric laminar diffusion flame, Symposium (International) on Combustion 27 (1998) 615-623.

[27] R.S. da Silva, L.R. Ventura, C.E. Fellows, M.Y. Ballester, A novel investigation of the N2(C3Πu−B3Πg)and N2(C″5Πu−A′5Σg+)band systems using accurate functional forms, Journal of Quantitative Spectroscopy and Radiative Transfer 253 (2020) 107130.

[28] A. Lofthus, P.H. Krupenie, The spectrum of molecular nitrogen, Journal of Physical and Chemical Reference Data 6 (1977) 113-307.

[29] S.S. Prasad, E.C. Zipf, Photochemical production of odd nitrogen directly from O2, N2 principals: Atmospheric implications and related open issues, Journal of Geophysical Research: Atmospheres 109 (2004).

[30] H.J. Werner, J. Kalcher, E.A. Reinsch, Accurate ab initio calculations of radiative transition probabilities between the A 3Σ+u, B 3Πg, W 3Δu, B′ 3Σ−u, and C 3Πu states of N2, The Journal of Chemical Physics 81 (1984) 2420-2431.

[31] J. Bishop, M.H. Stevens, P.D. Feldman, Molecular nitrogen Carroll-Yoshino v′ = 0 emission in the thermospheric dayglow as seen by the Far Ultraviolet Spectroscopic Explorer, Journal of Geophysical Research: Space Physics 112 (2007).

[32] C. Ni, X. Cheng, Ab initio study of the second positive system of N2 at high temperature, Computational and Theoretical Chemistry 1197 (2021) 113158.

[33] D.R. Crosley, Laser Probes for Combustion Chemistry, American Chemical Society Washington, D.C., 1980.

[34] D. Crosley, Collisional Effects On Laser-Induced Fluorescence Flame Measurements, Optical Engineering 20 (1981) 204511.

[35] D. Crosley, G. Smith, Laser-Induced Fluorescence Spectroscopy For Combustion Diagnostics, Optical Engineering 22 (1983) 225545.

[36] K. Kohse-Höinghaus, Laser techniques for the quantitative detection of reactive intermediates in combustion systems, Progress in Energy and Combustion Science 20 (1994) 203-279.

[37] A.C. Eckbreth, Laser Diagnostics for Combustion Temperature and Species, Second ed., CRC Press, Taylor and Francis Group, New York, NY, 1996.

[38] Y. Wang, A. Jain, W. Kulatilaka, Simultaneous measurement of CO and OH in flames using a single broadband, femtosecond laser pulse, Combustion and Flame 214 (2020) 358-360.

[39] A. Jain, Y. Wang, W.D. Kulatilaka, Simultaneous imaging of H and OH in flames using a single broadband femtosecond laser source, Proceedings of the Combustion Institute 38 (2021) 1813-1821.

[40] M. Hay, P. Parajuli, W.D. Kulatilaka, Simultaneous detection of three chemical species (NO, O, O2) using a single broadband femtosecond laser, Proceedings of the Combustion Institute, doi:https://doi.org/10.1016/j.proci.2022.08.090(2022).

[41] W.K. Bischel, B.E. Perry, D.R. Crosley, Detection of fluorescence from O and N atoms induced by two-photon absorption, Appl. Opt. 21 (1982) 1419-1429.

[42] T.J. McIlrath, R. Hudson, A. Aikin, T.D. Wilkerson, Two-photon lidar technique for remote sensing of atomic oxygen, Appl. Opt. 18 (1979) 316-319.

[43] R.P. Lucht, J.T. Salmon, G.B. King, D.W. Sweeney, N.M. Laurendeau, Two-photon-excited fluorescence measurement of hydrogen atoms in flames, Opt. Lett. 8 (1983) 365-367.

[44] J. Bittner, K. Kohse-Höinghaus, U. Meier, S. Kelm, T. Just, Determination of absolute H atom concentrations in low-pressure flames by two-photon laser-excited fluorescence, Combustion and Flame 71 (1988) 41-50.

[45] W.D. Kulatilaka, B.D. Patterson, J.H. Frank, T.B. Settersten, Comparison of nanosecond and picosecond excitation for interference-free two-photon laser-induced fluorescence detection of atomic hydrogen in flames, Appl. Opt. 47 (2008) 4672-4683.

[46] B. Li, D. Zhang, X. Li, Q. Gao, M. Yao, Z. Li, Strategy of interference-free atomic hydrogen detection in flames using femtosecond multi-photon laser-induced fluorescence, International Journal of Hydrogen Energy 42 (2017) 3876-3880.

[47] W.D. Kulatilaka, J.H. Frank, B.D. Patterson, T.B. Settersten, Analysis of 205-nm photolytic production of atomic hydrogen in methane flames, Applied Physics B 97 (2009) 227-242.

[48] A. Brockhinke, A. Bülter, J.C. Rolon, K. Kohse-Höinghaus, ps-LIF measurements of minor species concentration in a counterflow diffusion flame interacting with a vortex, Applied Physics B 72 (2001) 491-496.

[49] W.D. Kulatilaka, J.H. Frank, T.B. Settersten, Interference-free two-photon LIF imaging of atomic hydrogen in flames using picosecond excitation, Proceedings of the Combustion Institute 32 (2009) 955-962.

[50] W.D. Kulatilaka, J.R. Gord, V.R. Katta, S. Roy, Photolytic-interference-free, femtosecond two-photon fluorescence imaging of atomic hydrogen, Opt. Lett. 37 (2012) 3051-3053.

[51] W.D. Kulatilaka, J.R. Gord, S. Roy, Femtosecond two-photon LIF imaging of atomic species using a frequency-quadrupled Ti:sapphire laser, Applied Physics B 116 (2014) 7-13.

[52] C.A. Hall, W.D. Kulatilaka, J.R. Gord, R.W. Pitz, Quantitative atomic hydrogen measurements in premixed hydrogen tubular flames, Combustion and Flame 161 (2014) 2924-2932.

[53] A. Jain, Y. Wang, W.D. Kulatilaka, Effect of H-atom concentration on soot formation in premixed ethylene/air flames, Proceedings of the Combustion Institute 37 (2019) 1289-1296.

[54] J.B. Schmidt, S. Roy, W.D. Kulatilaka, I. Shkurenkov, I.V. Adamovich, W.R. Lempert, J.R. Gord, Femtosecond, two-photon-absorption, laser-induced-fluorescence (fs-TALIF) imaging of atomic hydrogen and oxygen in non-equilibrium plasmas, Journal of Physics D: Applied Physics 50 (2016) 015204.

[55] P. Ding, M. Ruchkina, Y. Liu, M. Alden, J. Bood, Femtosecond two-photon-excited backward lasing of atomic hydrogen in a flame, Opt. Lett. 43 (2018) 1183-1186.

[56] A. Jain, Y. Wang, W.D. Kulatilaka, Simultaneous imaging of H and OH in flames using a single broadband femtosecond laser source, Proceedings of the Combustion Institute, doi:https://doi.org/10.1016/j.proci.2020.07.137(2020).

[57] J.T. Salmon, N.M. Laurendeau, Absolute concentration measurements of atomic hydrogen in subatmospheric premixed H2/O2/N2 flat flames with photoionization controlled-loss spectroscopy, Appl. Opt. 26 (1987) 2881-2891.

[58] J.T. Salmon, N.M. Laurendeau, Concentration measurements of atomic hydrogen in subatmospheric premixed C2H4/O2/Ar flat flames, Combustion and Flame 74 (1988) 221-231.

[59] J.E.M. Goldsmith, Multiphoton-excited fluorescence measurements of atomic hydrogen in low-pressure flames, Symposium (International) on Combustion 22 (1989) 1403-1411.

[60] M. Aldén, A.L. Schawlow, S. Svanberg, W. Wendt, P.L. Zhang, Three-photon-excited fluorescence detection of atomic hydrogen in an atmospheric-pressure flame, Opt. Lett. 9 (1984) 211-213.

[61] K.E. Bertagnolli, R.P. Lucht, M.N. Bui-Pham, Atomic hydrogen concentration profile measurements in stagnation-flow diamond-forming flames using three-photon excitation laser-induced fluorescence, Journal of Applied Physics 83 (1998) 2315-2326.

[62] A. Jain, Y. Wang, W.D. Kulatilaka, Three-photon-excited laser-induced fluorescence detection of atomic hydrogen in flames, Opt. Lett. 44 (2019) 5945-5948.

[63] K.A. Rahman, K.S. Patel, M.N. Slipchenko, T.R. Meyer, Z. Zhang, Y. Wu, J.R. Gord, S. Roy, Femtosecond, two-photon, laser-induced fluorescence (TP-LIF) measurement of CO in high-pressure flames, Appl. Opt. 57 (2018) 5666-5671.

[64] K.A. Rahman, V. Athmanathan, M.N. Slipchenko, S. Roy, J.R. Gord, Z. Zhang, T.R. Meyer, Quantitative femtosecond, two-photon laser-induced fluorescence of atomic oxygen in high-pressure flames, Appl. Opt. 58 (2019) 1984-1990.

[65] Y. Wang, P. Parajuli, W. Swain, W.D. Kulatilaka, 1-kHz Femtosecond OH-PLIF Imaging in High-Pressure Flames, Under Review, (2021).

[66] D. Zahradka, N.J. Parziale, M.S. Smith, E.C. Marineau, Krypton tagging velocimetry in a turbulent Mach 2.7 boundary layer, Experiments in Fluids 57 (2016) 62.

[67] K. Niemi, V.S.-v.d. Gathen, H.F. Döbele, Absolute calibration of atomic density measurements by laser-induced fluorescence spectroscopy with two-photon excitation, Journal of Physics D: Applied Physics 34 (2001) 2330-2335.

[68] J.C. Miller, Two-photon resonant multiphoton ionization and stimulated emission in krypton and xenon, Physical Review A 40 (1989) 6969-6976.

[69] R.M. Magee, M.E. Galante, N. Gulbrandsen, D.W. McCarren, E.E. Scime, Direct measurements of the ionization profile in krypton helicon plasmas, Physics of Plasmas 19 (2012) 123506.

[70] Y. Wang, C. Capps, W.D. Kulatilaka, Femtosecond two-photon laser-induced fluorescence of krypton for high-speed flow imaging, Opt. Lett. 42 (2017) 711-714.

[71] D. Zelenak, V. Narayanaswamy, Composition-independent mean temperature measurements in laminar diffusion flames using spectral lineshape information, Experiments in Fluids 58 (2017) 147.

[72] P.H. Paul, J.E. Dec, Imaging of reaction zones in hydrocarbon–air flames by use of planar laser-induced fluorescence of CH, Opt. Lett. 19 (1994) 998-1000.

[73] M.G. Allen, R.D. Howe, R.K. Hanson, Digital imaging of reaction zones in hydrocarbon–air flames using planar laser-induced fluorescence of CH and C2, Opt. Lett. 11 (1986) 126-128.

[74] C.D. Carter, J.M. Donbar, J.F. Driscoll, Simultaneous CH planar laser-induced fluorescence and particle imaging velocimetry in turbulent nonpremixed flames, Applied Physics B 66 (1998) 129-132.

[75] N.L. Garland, D.R. Crosley, Energy transfer processes in CH A2Δ and B2Σ− in an atmospheric pressure flame, Appl. Opt. 24 (1985) 4229-4237.

[76] Z.S. Li, J. Kiefer, J. Zetterberg, M. Linvin, A. Leipertz, X.S. Bai, M. Aldén, Development of improved PLIF CH detection using an Alexandrite laser for single-shot investigation of turbulent and lean flames, Proceedings of the Combustion Institute 31 (2007) 727-735.

[77] A.N. Bunner, Cosmic Ray Detection by Atmospheric Fluorescence Graduate School of Cornell University, February 1967.

[78] M. Aldén, W. Wendt, Detection of nitrogen molecules through multi-photon laser excitation and N+2 fluorescence, Optics Communications 69 (1988) 31-36.

[79] F.J. Comes, F. Speier, Luminescence of Diatomic Molecular Ions: I. Franck-Condon-Factors and Collisional Deactivation, Zeitschrift für Naturforschung A 26 (1971) 1998-2007.

[80] P. Natalis, J. Delwiche, J.E. Collin, Enhancement of vibrational level population of N2+ and CO+ by photoelectron spectrometry, Chemical Physics Letters 13 (1972) 491-495.

[81] C.F. Kaminski, T. Dreier, Investigation of two-photon-induced polarization spectroscopy of the a–X (1,0) transition in molecular nitrogen at elevated pressures, Appl. Opt. 39 (2000) 1042-1048.

[82] N. Jiang, B.R. Halls, H.U. Stauffer, P.M. Danehy, J.R. Gord, S. Roy, Selective two-photon absorptive resonance femtosecond-laser electronic-excitation tagging velocimetry, Opt. Lett. 41 (2016) 2225-2228.

[83] P. Huber-Wälchli, D.M. Guthals, J.W. Nibler, Cars spectra of supersonic molecular beams, Chemical Physics Letters 67 (1979) 233-236.

[84] H.G. Heard, Ultra-violet Gas Laser at Room Temperature, Nature 200 (1963) 667-667.

[85] V. Kaslin, G. Petrash, Rotational structure of ultraviolet generation of molecular nitrogen, ZhETF Pisma Redaktsiiu 3 (1966) 88.

[86] C.A. Massone, M. Garavaglia, M. Gallardo, J.A.E. Calatroni, A.A. Tagliaferri, Investigation of a Pulsed Molecular Nitrogen Laser at Low Temperature, Appl. Opt. 11 (1972) 1317-1328.

[87] T. Fukuchi, R.F. Wuerker, A.Y. Wong, Lifetime and transition probability measurements of the second positive system of nitrogen by laser-induced fluorescence, The Journal of Chemical Physics 97 (1992) 9490-9491.

[88] Q.Y. Zhang, D.Q. Shi, W. Xu, C.Y. Miao, C.Y. Ma, C.S. Ren, C. Zhang, Z. Yi, Determination of vibrational and rotational temperatures in highly constricted nitrogen plasmas by fitting the second positive system of N2 molecules, AIP Advances 5 (2015) 057158.

[89] M. Yuan, J. Cheng, X. Cheng, Theoretical study of the ro-vibrational band of ground state for BaCl+ cation, Computational and Theoretical Chemistry 1172 (2020) 112670.

[90] B. Bai, H.H. Sawin, B.A. Cruden, Neutral gas temperature measurements of high-power-density fluorocarbon plasmas by fitting swan bands of C2 molecules, Journal of Applied Physics 99 (2006) 013308.

[91] M. Tuszewski, Ion and gas temperatures of 0.46MHz inductive plasma discharges, Journal of Applied Physics 100 (2006) 053301.

[92] E.J. Tonnis, D.B. Graves, Neutral gas temperatures measured within a high-density, inductively coupled plasma abatement device, Journal of Vacuum Science & Technology A 20 (2002) 1787-1795.

[93] V.M. Donnelly, M.V. Malyshev, Diagnostics of inductively coupled chlorine plasmas: Measurements of the neutral gas temperature, Applied Physics Letters 77 (2000) 2467-2469.

[94] N.v. Veen, P. Brewer, P. Das, R. Bersohn, Detection of the a 1Πg (v′=0, 1)←X 1Σ+g (v″=0) transition in N2 by laser-induced fluorescence, The Journal of Chemical Physics 77 (1982) 4326-4329.

[95] H. Helvajian, B.M. Dekoven, A.P. Baronavski, Laser-induced fluorescence of N2(X 1Σg+) and electron-impact excited N2+ (X 2Σg+) in a pulsed supersonic beam: Rotational distributions, Chemical Physics 90 (1984) 175-183.

[96] K.R. Lykke, B.D. Kay, Two-photon spectroscopy of N2: Multiphoton ionization, laser-induced fluorescence, and direct absorption via the a‘ 1Σ+g state, The Journal of Chemical Physics 95 (1991) 2252-2258.

[97] C. Rulliere, Femtosecond Laser Pulses: Principles and Experiments, Second ed., Springer2004.

[98] A.M. Weiner, Ultrafast Optics, John Wiley & Sons, Inc. , Hoboken, New Jersey, 2009.

[99] J. Diels, W. Rudolph, Ultrashort Laser Pulse Phenomena - Fundamentals, Techniques, and Applications on a Femtosecond Time Scale, Academic Press, Burlington, MA, 2006.

[100] Y.R. Shen, The Principles of Nonlinear Optics, John Wiley & Sons, NY, 1984.

[101] M. Schubert, B. Wilhelmi, Nonlinear Optics and Quantum Electronics, John Wiley & Sons, NY, 1978.

[102] R. Boyd, Nonlinear Optics, Academic Press, Boston, MA, 1977.

[103] R. Paschotta, Mode Locking. https://www.rp-photonics.com/mode_locking.html (accessed Oct 25 2021).

[104] M. Khelladi, Femtosecond Laser Pulses: Generation, Measurement and Propagation, Recent Advances in Numerical Simulations, IntechOpen2021.

[105] L. Piovani, Mid-InfraRed Tunable, Carrier-Envelope-Phase Stable, Pulsed Source, 2014.

[106] P.A. Franken, A.E. Hill, C.W. Peters, G. Weinreich, Generation of Optical Harmonics, Physical Review Letters 7 (1961) 118-119.

[107] A. Yariv, Optical Electronics in Modern Communications Oxford University Press, New York, 1997.

[108] User's Manual, Traveling-Wave Optical Parametric Amplifier of White-Light Continuum, 2014.

[109] A. Jain, P. Parajuli, Y. Wang, W.D. Kulatilaka, Hydroxyl radical planar laser-induced fluorescence imaging in flames using frequency-tripled femtosecond laser pulses, Opt. Lett. 45 (2020) 4690-4693.

[110] W.D. Kulatilaka, R.P. Lucht, S.F. Hanna, V.R. Katta, Two-color, two-photon laser-induced polarization spectroscopy (LIPS) measurements of atomic hydrogen in near-adiabatic, atmospheric pressure hydrogen/air flames, Combustion and Flame 137 (2004) 523-537.

[111] W.D. Kulatilaka, N. Chai, S.V. Naik, N.M. Laurendeau, R.P. Lucht, J.P. Kuehner, S. Roy, J.R. Gord, Measurement of nitric oxide concentrations in flames by using electronic-resonance-enhanced coherent anti-Stokes Raman scattering, Opt. Lett. 31 (2006) 3357-3359.

[112] N. Chai, W. Kulatilaka, S. Naik, N. Laurendeau, R. Lucht, J. Kuehner, S. Roy, V. Katta, J. Gord, Nitric oxide concentration measurements in atmospheric pressure flames using electronic-resonance-enhanced coherent anti-Stokes Raman scattering, Applied Physics B 88 (2007) 141-150.

[113] M.S. Wooldridge, P.V. Torek, M.T. Donovan, D.L. Hall, T.A. Miller, T.R. Palmer, C.R. Schrock, An experimental investigation of gas-phase combustion synthesis of SiO2 nanoparticles using a multi-element diffusion flame burner, Combustion and Flame 131 (2002) 98-109.

[114] N. Kastelis, E. Zervas. Analysis of flat burners used to study gaseous pollutants emitted from combustion of hydrocarbons. In: editor^editors. 2008. p.

[115] D.W. Senser, J.S. Morse, V.A. Cundy, Construction and novel application of a flat flame burner facility to study hazardous waste combustion, Review of Scientific Instruments 56 (1985) 1279-1284.

[116] F. Migliorini, S. De Iuliis, F. Cignoli, G. Zizak, How “flat” is the rich premixed flame produced by your McKenna burner?, Combustion and Flame 153 (2008) 384-393.

[117] W. Clauss, V.I. Fabelinsky, D.N. Kozlov, V.V. Smirnov, O.M. Stelmakh, K.A. Vereschagin, Dual-broadband CARS temperature measurements in hydrogen-oxygen atmospheric pressure flames, Applied Physics B 70 (2000) 127-131.

[118] S. Cheskis, Quantitative measurements of absolute concentrations of intermediate species in flames, Progress in Energy and Combustion Science 25 (1999) 233-252.

[119] Y.L. Chen, J.W.L. Lewis, C. Parigger, Spatial and temporal profiles of pulsed laser-induced air plasma emissions, Journal of Quantitative Spectroscopy and Radiative Transfer 67 (2000) 91-103.

[120] R.S. Barlow, C.D. Carter, Raman/Rayleigh/LIF measurements of nitric oxide formation in turbulent hydrogen jet flames, Combustion and Flame 97 (1994) 261-280.

[121] W. Meier, A.O. Vyrodov, V. Bergmann, W. Stricker, Simultaneous Raman/LIF measurements of major species and NO in turbulent H2/air diffusion flames, Applied Physics B 63 (1996) 79-90.

[122] W. Swain, Y. Wang, P. Parajuli, M. Hay, A. Saylam, T. Dreier, C. Schulz, W.D. Kulatilaka, Characterization of a High-Pressure Flame Facility Using High-Speed Chemiluminescence and OH PLIF, Experiments in Fluids, (2022, Under Review).

[123] P. Parajuli, Y. Wang, M. Hay, V.R. Katta, W.D. Kulatilaka, Femtosecond two-photon LIF imaging of atomic hydrogen in high-pressure methane-air flames, Proceedings of the Combustion Institute, doi:https://doi.org/10.1016/j.proci.2022.09.040(2022).

[124] J. Bittner, K. Kohse-höinghaus, U. Meier, T. Just, Quenching of two-photon-excited H(3s, 3d) and O(3p 3P2,1,0) atoms by rare gases and small molecules, Chemical Physics Letters 143 (1988) 571-576.

[125] V.R. Katta, W.M. Roquemore, On the structure of a stretched/compressed laminar flamelet—Influence of preferential diffusion, Combustion and Flame 100 (1995) 61-70.

[126] D. Goodwin, H. Moffat, R. Speth, Cantera: An Object-oriented Software Toolkit for Chemical Kinetics, Thermodynamics, and Transport Processes. Version 2.2.0, 2015.

[127] X. Xia, P. Zhang, A vortex-dynamical scaling theory for flickering buoyant diffusion flames, Journal of Fluid Mechanics 855 (2018) 1156-1169.

[128] N. Lamoureux, P. Parajuli, W. Kulatilaka, P. Desgroux, Evaluation of LIF thermometry technique using Krypton as a tracer: Impact of laser lineshape and collisional bandwidth, Proceedings of the Combustion Institute, doi:https://doi.org/10.1016/j.proci.2022.07.123(2022).

[129] M.G.H. Boogaarts, S. Mazouffre, G.J. Brinkman, H.W.P.v.d. Heijden, P. Vankan, J.A.M.v.d. Mullen, D.C. Schram, H.F. Döbele, Quantitative two-photon laser-induced fluorescence measurements of atomic hydrogen densities, temperatures, and velocities in an expanding thermal plasma, Review of Scientific Instruments 73 (2002) 73-86.

[130] A. Goehlich, T. Kawetzki, H.F. Döbele, On absolute calibration with xenon of laser diagnostic methods based on two-photon absorption, The Journal of Chemical Physics 108 (1998) 9362-9370.

[131] W.L. Wiese, J.R. Fuhr, Accurate Atomic Transition Probabilities for Hydrogen, Helium, and Lithium, Journal of Physical and Chemical Reference Data 38 (2009) 565-720.

[132] K. Dzierżęga, U. Volz, G. Nave, U. Griesmann, Accurate transition rates for the $5p\ensuremath{-}5s$ transitions in Kr I, Physical Review A 62 (2000) 022505.

[133] K.A. Watson, K.M. Lyons, J.M. Donbar, C.D. Carter, Visualization of multiple scalar and velocity fields in a lifted jet flame, Journal of Visualization 3 (2000) 275-285.

[134] X. Ma, C. Jiang, H. Xu, H. Ding, S. Shuai, Laminar burning characteristics of 2-methylfuran and isooctane blend fuels, Fuel 116 (2014) 281-291.

[135] J.M. Bergthorson, D.G. Goodwin, P.E. Dimotakis, Particle streak velocimetry and CH laser-induced fluorescence diagnostics in strained, premixed, methane–air flames, Proceedings of the Combustion Institute 30 (2005) 1637-1644.

[136] M.A. Turner, T.T. Paschal, P. Parajuli, W.D. Kulatilaka, E.L. Petersen, Resolving flame thickness using high-speed chemiluminescence imaging of OH* and CH* in spherically expanding methane–air flames, Proceedings of the Combustion Institute 38 (2021) 2101-2108.

[137] J. Kiefer, F. Ossler, Z.S. Li, M. Aldén, Spectral interferences from formaldehyde in CH PLIF flame front imaging with broadband B-X excitation, Combustion and Flame 158 (2011) 583-585.

[138] Z.I. Botev, J.F. Grotowski, D.P. Kroese, Kernel density estimation via diffusion, The Annals of Statistics 38 (2010) 2916-2957, 2942.

[139] I.A. Mulla, B. Renou, Simultaneous imaging of soot volume fraction, PAH, and OH in a turbulent n-heptane spray flame, Combustion and Flame 209 (2019) 452-466.

[140] S.G. Tilford, J.T. Vanderslice, P.G. Wilkinson, The High Resolution Absorption Spectrum of Nitrogen from 1060 TO 1520 Å. III. The B'^{3}Σ_{u} <- X^{1}Σ_{g}^{+} System, The Astrophysical Journal 141 (1965) 1226.

[141] M. Lei, C. Wu, Q. Liang, A. Zhang, Y. Li, Q. Cheng, S. Wang, H. Yang, Q. Gong, H. Jiang, The fast decay of ionized nitrogen molecules in laser filamentation investigated by a picosecond streak camera, Journal of Physics B: Atomic, Molecular and Optical Physics 50 (2017) 145101.

[142] P. Ran, G. Li, T. Liu, H. Hou, S.-n. Luo, Collision-mediated ultrafast decay of N2 fluorescence during fs-laser-induced filamentation, Optics express 27 (2019) 19177-19187.

[143] Y.-C. Wang, C.-Y. Wu, Y.-X. Liu, S.-H. Xu, Q.-H. Gong, Fluorescence emission from excited molecular ions in intense femtosecond laser fields, Frontiers of Physics 8 (2013) 34-38.

[144] R.E. Imhof, F.H. Read, Measured lifetimes of the C³Π_ustate of N₂and the a³Σ_g⁺state of H₂, Journal of Physics B: Atomic and Molecular Physics 4 (1971) 1063-1069.

[145] P. Millet, Y. Salamero, H. Brunet, J. Galy, D. Blanc, J.L. Teyssier, De-excitation of N2 (C 3Πu ; ν′ = 0 and 1) levels in mixtures of oxygen and nitrogen, The Journal of Chemical Physics 58 (1973) 5839-5841.

[146] M. Larsson, T. Radozycki, Time Resolved Studies of Perturbations in thev'= 1 Level and Radiative Properties of theC³Π_ustate in N₂, Physica Scripta 25 (1982) 627-630.

[147] A. Morozov, T. Heindl, J. Wieser, R. Krücken, A. Ulrich, Influence of pressure on the relative population of the two lowest vibrational levels of the C 3 Πu state of nitrogen for electron beam excitation, The European Physical Journal D 46 (2008) 51-57.

[148] Z. Qin, J. Zhao, L. Liu, Radiative transition probabilities between low-lying electronic states of N2, Molecular Physics 117 (2019) 2418-2433.

[149] J.C. McDaniel, B. Hiller, R.K. Hanson, Simultaneous multiple-point velocity measurements using laser-induced iodine fluorescence, Opt. Lett. 8 (1983) 51-53.

[150] U. Westblom, S. Svanberg, Imaging Measurements of Flow Velocities using Laser-Induced Fluorescence, Physica Scripta 31 (1985) 402-405.

[151] K. Niemi, V.S.-v.d. Gathen, H.F. Döbele, Absolute atomic oxygen density measurements by two-photon absorption laser-induced fluorescence spectroscopy in an RF-excited atmospheric pressure plasma jet, Plasma Sources Science and Technology 14 (2005) 375-386.

[152] N. Lamoureux, P. Desgroux, Direct quantification of O-atom in low-pressure methane flames by using two-photon LIF, Proceedings of the Combustion Institute 38 (2021) 1753-1760.

[153] J.B. Schmidt, B. Sands, J. Scofield, J.R. Gord, S. Roy, Comparison of femtosecond- and nanosecond-two-photon-absorption laser-induced fluorescence (TALIF) of atomic oxygen in atmospheric-pressure plasmas, Plasma Sources Science and Technology 26 (2017) 055004.

[154] S.J. Pendleton, S. Bowman, C. Carter, M.A. Gundersen, W. Lempert, The production and evolution of atomic oxygen in the afterglow of streamer discharge in atmospheric pressure fuel/air mixtures, Journal of Physics D: Applied Physics 46 (2013) 305202.

[155] A.F.H. van Gessel, S.C. van Grootel, P.J. Bruggeman, Atomic oxygen TALIF measurements in an atmospheric-pressure microwave plasma jet within situxenon calibration, Plasma Sources Science and Technology 22 (2013) 055010.

APPENDIX

Appendix A Detection Instruments

Figure I, Figure II and Figure III shows the ICCD camera, high-speed camera and spectrometer used for the experiment in this study, respectively.

Figure I An ICCD camera (Princeton instruments, PIMAX 4).

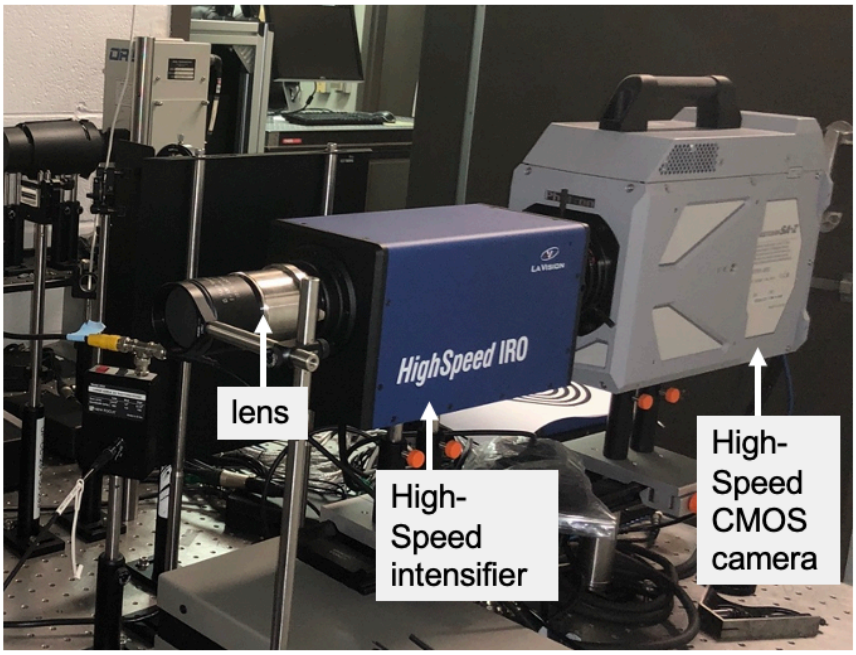

Figure II A high-speed CMOS camera (Photron, SA-Z) coupled with a HS-IRO intensifier (LaVision, HS-IRO).

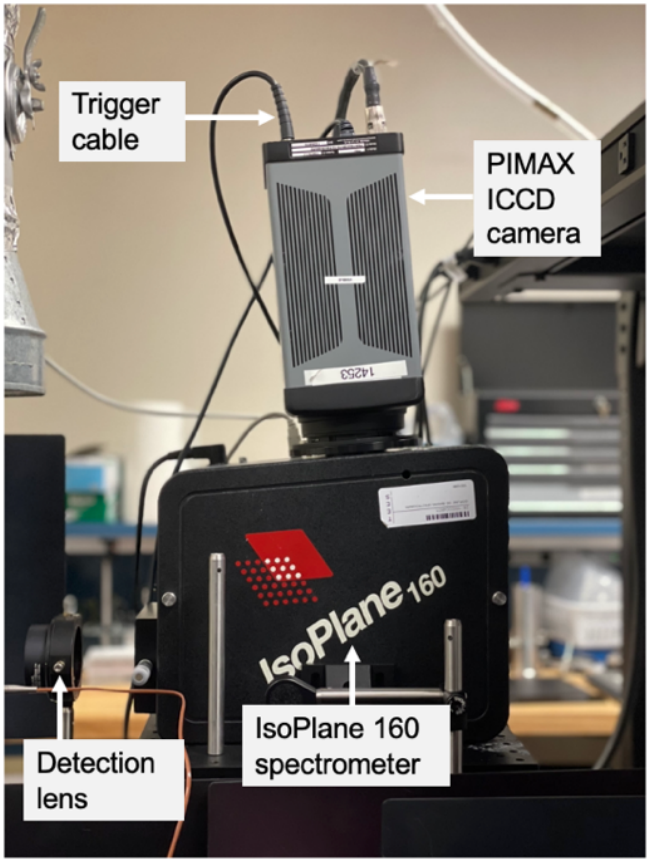

Figure III A spectrometer (Princeton Instruments, IsoPlane 160) fitted with an ICCD camera (Princeton Instruments, PIMAX 4).

Appendix B Laser Sheet Correction Profile

This section presents the approach/methodology to correct the species fluorescence signal for laser non-uniformity. This approach was applied to O-atom fluorescence images in nanosecond pin-to-pin plasma discharges. The correction is necessary as the spatial non-uniformity in laser sheet profile significantly influences the fluorescence distribution. Figure indicates the original location of the laser sheet and electrodes.

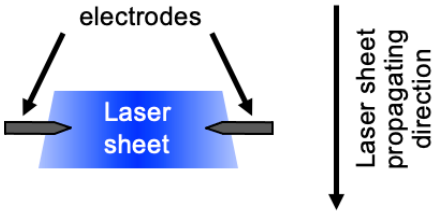

Figure IV Original position of laser sheet and electrodes.

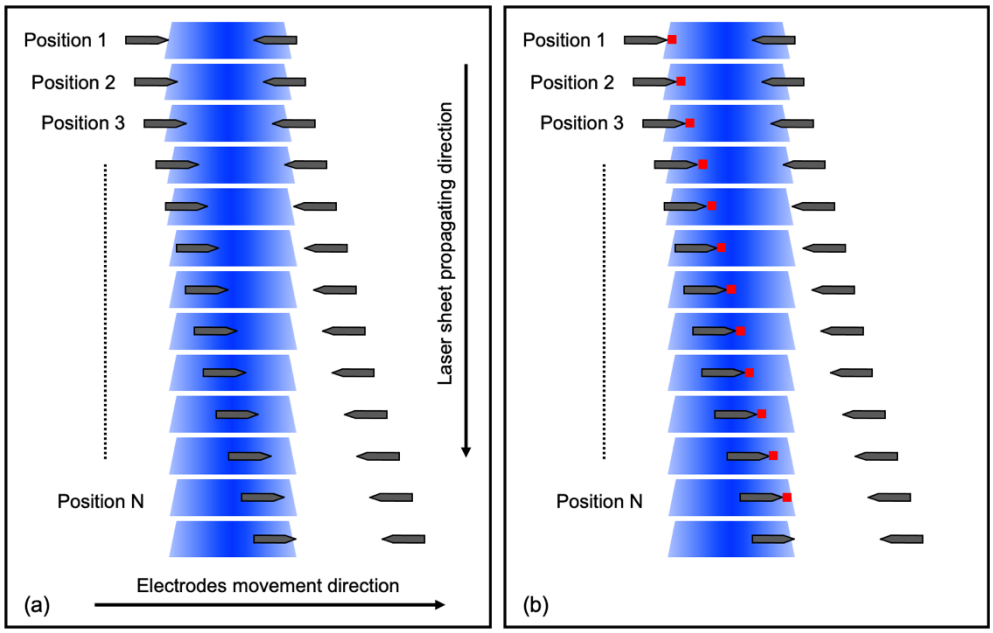

Figure V Procedure to obtain laser sheet profile.

For laser sheet profile correction map, the position of the laser sheet profile and the detection system was kept fixed. The electrodes were translated in horizontal direction through the entire width of the laser sheet in small steps (~0.215 mm in our case). At each position (Position 1, Position 2, …..., Position N), a signal and background images were recorded. During data processing, a small rectangular section (indicted by red rectangles near the tip of the electrodes in Figure b) with length 0.215 mm was selected for each position after background subtraction. The length of the rectangular section should be same as the translation distance of the electrodes. If the section considered is sufficiently small, the variation in O-atom signal in X-direction is negligible and can be assumed uniform field. So, the only variable in each section is laser intensity. The background-subtracted signal profile in each of these rectangular sections at different positions are added together in X-direction to obtain spatial profile of laser intensity as indicated by red curve in Figure a. Once the laser profile is obtained, each of the raw and background-subtracted fluorescence profile/ image (a sample profile is shown by blue curve in Figure a is divided by the laser profile to obtain final fluorescence profile. A sample laser beam profile corrected; final fluorescence profile is shown by black curve in Figure b.

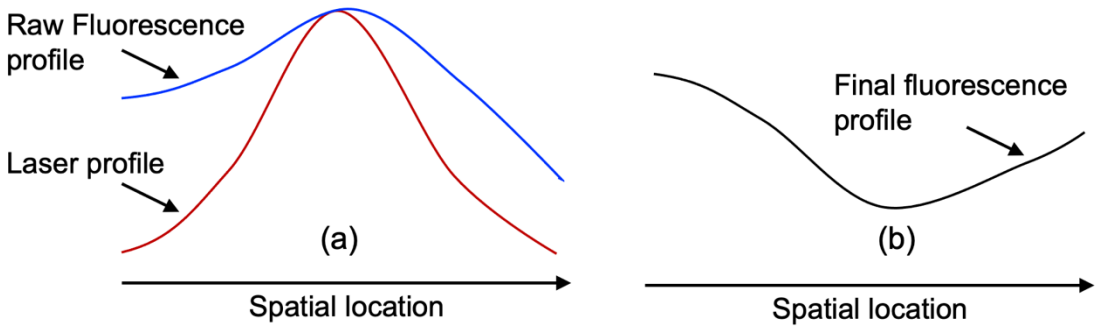

Figure VI Procedure to obtain laser profile corrected fluorescence profile.

Appendix C Quantitative O-atom Concentration Measurement Approaches

This section presents the approach/methodology to quantify the species fluorescence signal. This approach was applied to O-atom fluorescence images in nanosecond pin-to-pin plasma discharges. The O atom mole fraction is calculated using

$$\chi_O = \chi_{Xe} \frac{C_{Xe}}{C_O} \frac{\sigma_{Xe}^{\langle 2 \rangle}}{\sigma_O^{\langle 2 \rangle}} \frac{g(\Delta\bar{\nu}_{Xe})}{g(\Delta\bar{\nu}_O)} \frac{A_{23,Xe}}{A_{23,O}} \frac{A_O+Q_O}{A_{Xe}+Q_{Xe}} \frac{1}{f_B(O_{J"=2},T)} \frac{S_O}{S_{Xe}} \frac{I_{\bar{\nu}Xe}^2}{I_{\bar{\nu}O}^2} \left(\frac{\nu_O}{\nu_{Xe}}\right)^2 \quad \text{I}$$

Where,

χ_{Xe}= mole fraction of Xenon

$\frac{C_{Xe}}{C_O}$ = Quantum efficiencies of detectors (e.g., lens, filter, camera)

$\frac{\sigma_{Xe}^{\langle 2 \rangle}}{\sigma_O^{\langle 2 \rangle}}$ = Ratio of the absorption cross-sections between Xe and O

$\frac{g(\Delta\bar{\nu}_{Xe})}{g(\Delta\bar{\nu}_O)}$ = Ratio of the normalized line profile of the two-photon excitation

$A_{23,i}$ = spontaneous emission rate along the detection transition (from level 2 to 3)

A_i= radiative lifetime of the excited level

Q_i= total quenching rate

f_B= temperature dependent Boltzmann function of the probed sub-level of the ground state

$\frac{S_O}{S_{Xe}}$ = fluorescence signal ratio

I_{ν_i}= laser intensity

ν_i= laser frequency

Using $a_i = \frac{A_{23,i}}{A_i+Q_i}$ = branching ratio of individual species (i), Eq. I can be reduced to

$$\chi_O = \chi_{Xe} \frac{C_{Xe}}{C_O} \frac{\sigma_{Xe}^{\langle 2 \rangle}}{\sigma_O^{\langle 2 \rangle}} \frac{g(\Delta\bar{\nu}_{Xe})}{g(\Delta\bar{\nu}_O)} \frac{a_{Xe}}{a_O} \frac{1}{f_B(O_{J"=2},T)} \frac{S_O}{S_{Xe}} \frac{I_{\nu Xe}^2}{I_{\nu O}^2} \left(\frac{\nu_O}{\nu_{Xe}}\right)^2 \quad \text{II}$$

The values of the parameters used are:

Table I Values for the parameters used

$\chi_{Xe} = 0.01$;
$\frac{C_{Xe}}{C_O} = 1$;
$\frac{\sigma_{Xe}^{\langle 2 \rangle}}{\sigma_O^{\langle 2 \rangle}} = 1.9 \pm 20\%$ [151, 152];
$\frac{g(\Delta\bar{\nu}_{Xe})}{g(\Delta\bar{\nu}_O)} = 1$; Because of the broad bandwidth of the femtosecond laser used as compared to the laser linewidth.
$\frac{1}{f_B(O_{J"=2},T)} = \frac{1}{0.6} = 1.6667$; The atomic oxygen in the ground state ^{3}P is distributed into 3 sub-levels (J" = 0,1,2). The Boltzmann function of the probed sub-level (J" = 2) is close to 0.6 at temperatures higher than 1300 K [151, 152]. Xenon in the ground state lies in a singlet state 1S, and f_B is equal to 1, independent of the temperature.
$\frac{I_{\nu Xe}^2}{I_{\nu O}^2} = 1$; Laser energy was kept constant
$\left(\frac{\nu_O}{\nu_{Xe}}\right)^2 = 0.991$
$\frac{1}{A_{23,Xe}} = 40\ ns$; $\frac{1}{A_{23,O}} = 35.4\ ns$; [151-153]
$\frac{A_{23,Xe}}{A_{Xe}} = 0.733$; $\frac{A_{23,O}}{A_O} = 1$; [151, 152]
Q_O *and* Q_{Xe} need to be determined for branching ratio a_O and a_{Xe}.

There are two approaches for branching ratio calculation:

1. Approach one for branching ratio calculation

The branching ratio is $a_i = \frac{A_{23,i}}{A_i+Q_i}$. $A_{23,i}$ and A_i are provided above.

The collisional quenching rate Q is given by:

$$Q_i = \sum_i n_i \, k_i; \qquad \text{III}$$

Where, n_i is the density of colliding species, k_i is the quenching rate coefficients.

The values for k_i can be obtained in literatures. The temperature was estimated to be 1400 K.

Table II Mole fractions and quenching rate coefficients used

		k_i (10^{-10} cm^3/s)	
	Mole fraction	Xe	O
Xe	0.01	3.60 [151]	-
O_2	0.2079	20.6 [67]	9.3 [67, 151, 154]
N_2	0.7821	14.6 [67]	5.9 [67, 154]

For Q_O, O_2 and N_2 are considered as quenching colliders and mole fraction is 0.2079 (for O_2) and 0.7821 (for N_2). Similarly, for Q_{Xe}, the available rate coefficient for excited state Xe ($6p'[3/2]_2$) is only that of Xe itself. So, values of the rate coefficient for quenching colliders O_2 and N_2 were taken as that of the excited state Xe ($7p[3/2]_2$).

Once, Q_O and Q_{Xe} are calculated, all the values of Table I are inserted in Eq I to obtain O-atom mole fraction and convert it to num density. A sample image in shown in Figure VII.

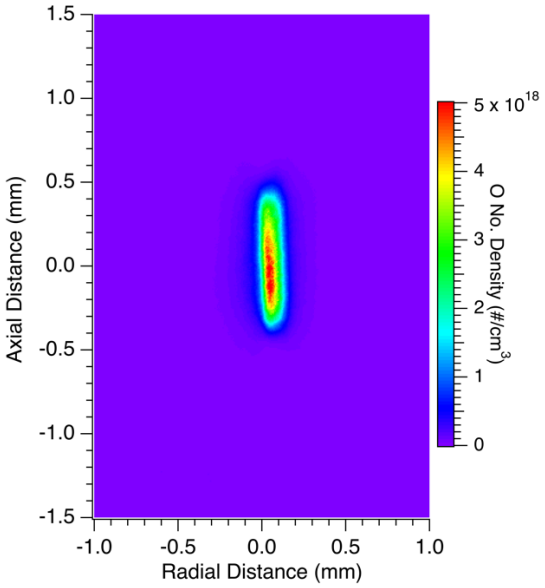

Figure VII O-TPLIF sample image at delay = 5000 ns using approach 1.

2. Approach two for branching ratio calculation

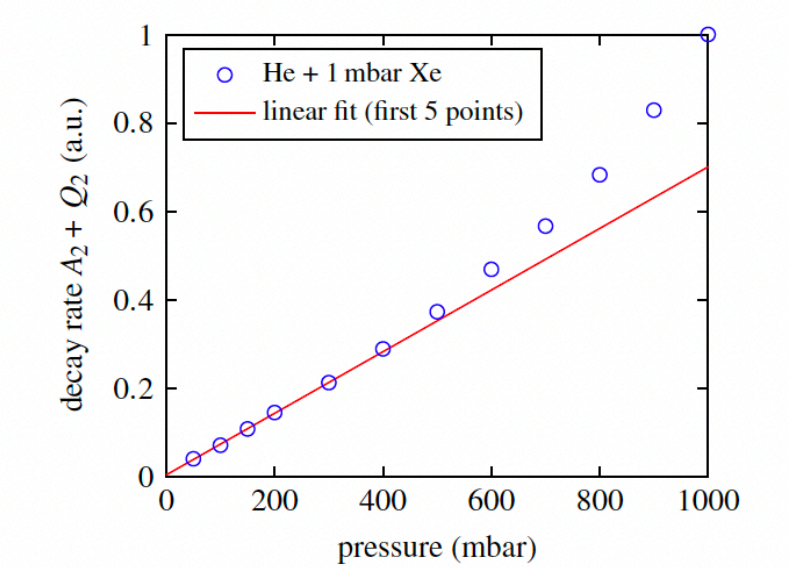

Figure VIII Stern-Volmer plot showing a non-linear dependence of the collisional quenching of Xe reprinted from [155].

As shown in Figure VIII, van Gessel et al. [155] claims that the decay rate above 0.4 bar is not linear with the pressure, which means that Eq. III is not valid for Xe at high pressures. The additional quenching is most likely due to three-body collisions. Since at atmospheric pressure, Q_{Xe} cannot be calculated using Eq. III, the quenching coefficients of the Xe states only give a qualitative indication of the quenching rate at atmospheric pressure and cannot be used to calculate branching ratio (a). The absolute value of a has to be determined experimentally. So, Xe TALIF measurements are performed in a vacuum vessel at low pressure. The branching ratio of Xe at low pressure (a_{low}) is calculated and converted to the branching ratio at atmospheric pressure (a_{atm}) using the following equation.

$$a_{atm} = a_{low} \frac{C_{low}}{C_{atm}} \frac{n_{low}}{n_{atm}} \frac{\langle E_{low}^2 \rangle}{\langle E_{atm}^2 \rangle} \frac{S_{atm}}{S_{low}} \qquad 10.4$$

Where, C_i is the quantum efficiencies, n_i is the number densities of species, E_i is the laser energy used, S_i is the fluorescence signal.

For a_i, A_{23} are taken from the Table I. $(A_i + Q_i)$ are the inverse of fluorescence decay (τ). τ was measured from exponential fitting between 100% and 30% of the fluorescence signal (as done in Ref [152]).

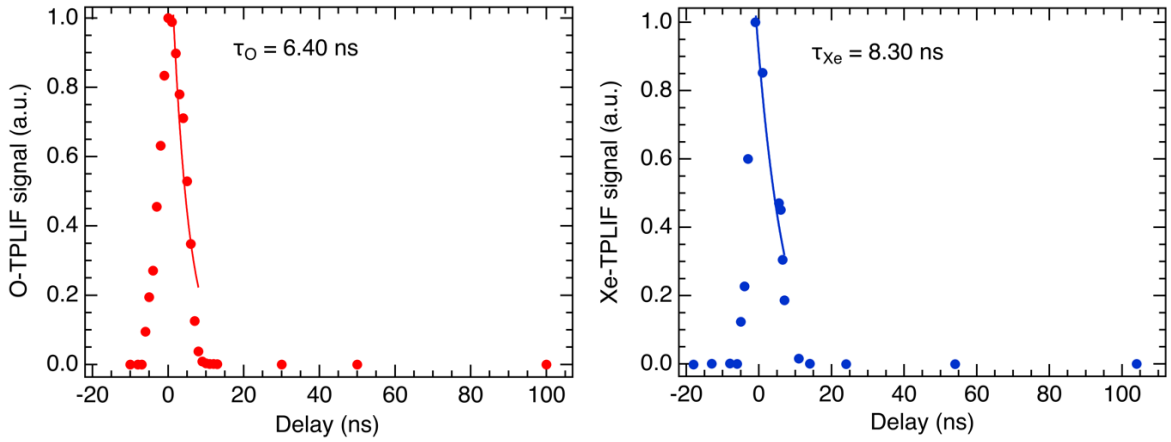

Figure IX Fluorescence lifetime for O-TPLIF at 1 bar (left) and Xe-TPLIF at 0.2 bar (right).

In our case, since the fluorescence lifetime for Xe is not measurable at 1 bar hence it was measured at 0.2 bar. From Fig. 2, $\tau_O @\ 1\ bar = 6.40\ ns$ and $\tau_{Xe} @\ 0.2\ bar = 8.30\ ns$. This allows us to calculate a_{atm} for Oxygen and a_{low} for Xe and a_{atm} for Xe can be calculated using Eq. IV.

The values of different parameters are:

Table III Values of parameters used for $a_{\_atm,Xe}$ calculation

$\frac{C_{low}}{C_{atm}} = 1;$
$\frac{n_{low}}{n_{atm}} = \frac{1}{5};$
$\frac{\langle E_{low}^2 \rangle}{\langle E_{atm}^2 \rangle} = 0.82^2 = 0.6724$
$\frac{S_{atm}}{S_{low}}$ obtained from the experiment

Once, $a_{atm,O}$ and $a_{atm,Xe}$ are calculated, all the values of Table I are inserted in Eq. II to obtain O-atom mole fraction and convert it to num density. A sample image is shown in Figure X.

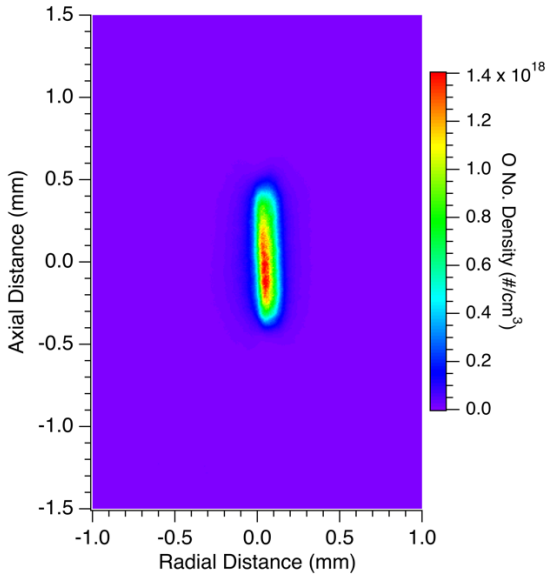

Figure X O-TPLIF sample image at delay = 5000 ns using approach 2.